Fatigue Response of Mo-Si-B Alloys

(N00014-00-1-0373)

Final Report

Submitted by:

K.S. Kumar
Division of Engineering
Brown university
Providence, RI 02912

Submitted to:

Materials Division
Office of Naval Research
800 N. Quincy Street
Arlington, VA 22217

DISTRIBUTION STATEMENT A
Approved for Public Release
Distribution Unlimited

20050930 025

REPORT DOCUMENTATION PAGE	*Form Approved* *OMB No. 0704-0188*

The public reporting burden for this collection of information is estimated to average 1 hour per response, including the time for reviewing instructions, searching existing data sources, gathering and maintaining the data needed, and completing and reviewing the collection of information. Send comments regarding this burden estimate or any other aspect of this collection of information, including suggestions for reducing the burden, to Department of Defense, Washington Headquarters Services, Directorate for Information Operations and Reports (0704-0188), 1215 Jefferson Davis Highway, Suite 1204, Arlington, VA 22202-4302. Respondents should be aware that notwithstanding any other provision of law, no person shall be subject to any penalty for failing to comply with a collection of information if it does not display a currently valid OMB control number.

PLEASE DO NOT RETURN YOUR FORM TO THE ABOVE ADDRESS.

1. REPORT DATE *(DD-MM-YYYY)* 9/27/05	**2. REPORT TYPE** Final Technical Report	**3. DATES COVERED** *(From - To)* 06/01/2000-05/30/2004

4. TITLE AND SUBTITLE
Fatigue Response of Mo-Si-B Alloys

5a. CONTRACT NUMBER
N/A

5b. GRANT NUMBER
N00014-00-1-0373

5c. PROGRAM ELEMENT NUMBER
N/A

6. AUTHOR(S)
K. S. Kumar

5d. PROJECT NUMBER
N/A

5e. TASK NUMBER
N/A

5f. WORK UNIT NUMBER
N/A

7. PERFORMING ORGANIZATION NAME(S) AND ADDRESS(ES)
Brown University
Division of Engineering, Box D
182 Hope Street
Providence, RI 02912

8. PERFORMING ORGANIZATION REPORT NUMBER
N/A

9. SPONSORING/MONITORING AGENCY NAME(S) AND ADDRESS(ES)
Dr. Steven G. Fishman
Office of Naval Research
800 North Quincy Street
Arlington, VA 22217-5660

10. SPONSOR/MONITOR'S ACRONYM(S)
ONR

11. SPONSOR/MONITOR'S REPORT NUMBER(S)
N/A

12. DISTRIBUTION/AVAILABILITY STATEMENT
Approved for Public Release; Distribution is Unlimited

13. SUPPLEMENTARY NOTES

14. ABSTRACT

The high-temperature compression response as well as the monotonic and cyclic crack growth behavior of a two-phase Mo-Si-B alloy compared to a TZM alloy. The compression studies confirmed that deformation in the temperature-strain rate space evaluated is matrix-dominated. In all instances evaluated, the Mo-Si-B alloys is superior to TZM. Fracture toughness of the Mo-Si-B alloy increases from ~8MPa•m at room temperature to ~25 MPa•m at 1400°C, the increase being steepest between 1200°C and 1400°C. S-N response at room temperature is shallow whereas at 1200°C, a definitive fatigue response is observed. Fatigue crack growth in vacuum and air in the temperature interval 20°C-600°C is similar for the Mo-Si-B alloy whereas significant deterioration is noted for TZM when it is tested in air. The Paris slopes for the two alloys is high at room temperature (~20-30) and decreases with increasing temperature to ~3 at 1400°C. Activation energy measurements illustrate grain-boundary diffusion dominance in the 900° C-1200°C regime and volume diffusion dominance in the 1200°C-1400°C regime.

15. SUBJECT TERMS
Molybdenum alloys, Mechanical Properties, Fatigue, Creep, Microstructure, multiphase alloys

16. SECURITY CLASSIFICATION OF:			**17. LIMITATION OF ABSTRACT**	**18. NUMBER OF PAGES**	**19a. NAME OF RESPONSIBLE PERSON**
a. REPORT	**b. ABSTRACT**	**c. THIS PAGE**			K. Sharvan Kumar
unclassified				76	**19b. TELEPHONE NUMBER** *(Include area code)* 401-863-2862

Standard Form 298 (Rev. 8/98)
Prescribed by ANSI Std. Z39.18

Executive Summary

Mo-Si-B alloys are being considered as possible candidates for high-temperature applications beyond the capabilities of Ni-based Superalloys. In this Report, the high-temperature compression response as well as the monotonic and cyclic crack growth behavior (as a function of temperature) of a two-phase Mo-Si-B alloy is discussed and compared to an off-the-shelf TZM alloy.

The compression response was examined as a function of strain rate in the 1000°C-1400°C range. A limited number of tests were also conducted on a three-phase alloy comprising Mo solid solution + T2 + Mo_3Si. These compression studies confirmed that deformation in the temperature-strain rate space evaluated is matrix-dominated, yielding an activation energy of ~415-445 kJ/mol. As a consequence, the response of the three-phase material overlaps that of the two-phase material. In all instances evaluated, the Mo-Si-B alloys exhibit superior flow stress relative to their TZM counterpart. Examination of the deformed microstructure illustrates that recovery and in some instances, recrystallization occurs in the Mo solid solution matrix whereas the T2 phase either cracks or deforms plastically depending on the temperature and strain rate used. Finite element analysis assuming an elastic-plastic matrix and an elastic second phase illustrates strain localization in the matrix, the extent being more severe when the work-hardening rate in the matrix decreases (i.e. increasing temperature and decreasing strain rate) while the stress supported by the T2 particles is substantial. However, if plastic deformation is permitted in the T2 particles strain distribution is homogenized substantially. The interplay between matrix and T2 properties and their dependence on temperature and strain rate are used to explain the observed deformed microstructure.

Fracture toughness of the Mo-Si-B alloy varies from ~8MPa√m at room temperature to ~25 MPa√m at 1400°C, the increase in toughness with temperature being steepest between 1200°C and 1400°C. S-N response at room temperature is shallow whereas at 1200°C, a definitive fatigue response is observed. Fatigue crack growth in vacuum and air in the temperature interval 20°C-600°C is similar for the Mo-Si-B alloy whereas significant deterioration is noted for TZM when it is tested in air. The difference in response is attributed to differences in the oxide scales formed in the two alloys. The Paris slopes for the two alloys is high at room temperature (~20-30) and decreases with increasing temperature to ~3 at 1400°C. For the Mo-Si-B alloy, da/dN for a fixed value of ΔK in the Paris regime in the 900°C-1400°C range, increases with increasing temperature. Apparent activation energies extracted using an Arrhenius-type relationship illustrate grain-boundary diffusion dominance in the 900°C-1200°C regime and volume diffusion dominance in the 1200°C-1400°C regime.

Table of Contents

Executive Summary 2

1.0 Introduction 5

2.0 Background 7

- 2.1 Fatigue Response of Metals and Alloys 7
- 2.2 Molybdenum-Based Alloys for High-Temperature Applications 12
- 2.3 Mo-Si-B Alloys: Phase Equilibria 14
- 2.4 Mo-Si-B Alloys: Mechanical Properties 17
  - 2.4.1 Single-phase alloys 17
  - 2.4.2 Two-phase alloys 18
  - 2.4.3 Three-phase alloys 19
- 2.5 Summary and Unresolved Issues 20

30. Experimental Procedure 22

- 3.1 Material Preparation 22
- 3.2 Compression Studies 22
- 3.3 Isothermal Oxidation Studies 24
- 3.4 Monotonic Crack Growth Studies 24
- 3.5 Stress-Number of Cycles to Failure (S-N) Studies 24
- 3.6 Cyclic Crack Growth Studies 24

4.0 High Temperature Compression Response 27

- 4.1 Initial Microstructure 27
- 4.2 Compression Response 29
- 4.3 Post-Deformation Microstructure 36
- 4.4 Discussion of Microstructure and Strengthening Mechanisms 39
- 4.5 Analysis of the Deformation Behavior of the Two-Phase Aggregate 43

5.0 Fracture Toughness and Fatigue Response 49

- 5.1 Isothermal Oxidation Response 49
- 5.2 Fracture Toughness and Monotonic Crack Growth Response 50
- 5.3 Cyclic Loading Response--Stress-Cycles (S-N) to Failure 52
- 5.4 Cyclic Loading Response -- Crack Growth Studies 54
- 5.5 Discussion of Results 62

6.0 Conclusions 71

- 6.1 High Temperature Compression Response 71
- 6.2 Fracture Toughness and Fatigue Response 71

7.0 References 74

1.0 INTRODUCTION

The ever-increasing demand for materials suitable for elevated temperature applications in the aircraft and aerospace industry beyond the realm of Ni-base superalloys has generated significant research interest in refractory metals and their alloys, intermetallics and ceramics. The lack of damage tolerance (impact as well as crack growth resistance in monotonic and cyclic loading) in many intermetallics and most ceramics has guided research in the direction of multiphase refractory alloys that contain a matrix phase that in principle is capable of providing damage tolerance, and a significant volume fraction of second phase(s) that enhances the creep resistance of the alloy. Thus multiphase Nb-based alloys and Mo-based alloys have been the focus of research attention over the past few years; an overview on each of these alloy systems that provides a brief history of their development, summarizes the current understanding and identifies the numerous challenges that lie ahead, was recently published [1,2]. Additional important requirements for such applications are isothermal and cyclic oxidation resistance and considerable attention has been devoted to improving this property in these refractory alloy systems using approaches that including alloying as well as application of coatings [3-6].

For a variety of reasons, the United States Air Force and Navy recently opted to focus on the Mo-Si-B system for further studies, and considerable efforts are underway at Pratt and Whitney, East Hartford Connecticut to identify reliable vendors and to streamline production capabilities of alloys in this system; furthermore, basic research including understanding of microstructural evolution during processing and testing, evaluating the full suite of mechanical and physical properties, further enhancing environmental resistance through alloying and determining the interplay between processing, structure and properties are all underway at various academic institutions, Corporate, National (DOE) and Defense laboratories across the country.

An important consideration in rotating aircraft engine components is the fatigue response, and fatigue-creep interactions. There is paucity in fatigue data in Mo alloys in general, and those data that are available appear to pose reproducibility problems. Thus there is a significant gap in the literature in this area and a near-future technological need for the information (high cycle fatigue, low cycle fatigue, fatigue crack growth behavior). Driven by this need, the Office of Naval Research (ONR) sponsored a three-year effort at Brown University to characterize and understand the fatigue response of a two-phase Mo-Si-B alloy (Mo solid solution + T2 phase of a fixed volume fraction) over a broad temperature range. Intrinsic to this research was the determination of the creep response of the alloy, and the resulting fatigue-creep interaction. The effort also included a comparison of the fatigue response with an off-the-shelf Mo alloy (TZM) that provided the baseline. This report (Final Report) summarizes the findings of the study.

In terms of organization of this report, in the next chapter, basic ideas relating to fatigue response of metallic materials are first presented (In this context, the reader is advised that a comprehensive treatment of the subject is available in Reference 2) including a short review of the limited literature relating to fatigue behavior of molybdenum and its alloys. This is followed by a summary of the phase equilibria of the Mo-Si-B ternary system and a brief discussion of the microstructure of potential alloys for high temperature service. Next, mechanical properties that have been obtained for Mo-Si-B alloys are summarized. In the last section of this Chapter, the Summary of the literature findings is provided and from it the unresolved issues are extracted. The Chapters following that (Chapters 3, 4 and 5) comprise, experimental procedure, results of high temperature compression tests and associated computational studies, and results of fatigue tests respectively. In the chapter on fatigue testing that includes S-N tests and fatigue crack growth studies, we also include results of monotonic crack growth studies. In each of the chapters, we present microstructural observations as appropriate. In Chapter 6, we summarize out findings.

2.0 BACKGROUND

2.1 Fatigue Response of Metals and Alloys

Almost all types of engineered structures are prone to fatigue failure and in some, such as those common to aircraft, design against fatigue failure is as important as is design against yielding or conventional failure. Rotating parts such as automotive drive axles and aircraft engine turbine blades experience fatigue in service and therefore designing against fatigue is of primary concern. The random nature of many time-varying stress applications makes laboratory simulation of fatigue difficult.

Fatigue fracture involves crack nucleation, growth and coalescence. Crack nucleation is related to inhomogeneous plastic flow occurring at a microscopic level and this can occur even when a structure is only elastically stressed at the macroscopic level. Such cracks once nucleated will then grow as a consequence of the cyclic stress over a period of time. During the slow-growth process, the crack advance rate is related to the frequency of the stress or strain cycle. Slow crack growth is interrupted by final fast fracture either due to overload failure, or due to the fact that the fatigue crack has grown sufficiently that the fracture toughness of the material is exceeded. Thus, in fatigue, a structure will withstand a certain number of stress or strain cycles prior to failure.

Fatigue fracture initiation is the least well-understood of the various aspects of fatigue. In metallic materials, fracture originates at internal or external surfaces, the latter being more common. In all materials, there are regions of local inhomogeneity that result in local softening, or surface flaws that cause local stress concentrations. Either or both of these factors can result in localized plastic flow, which under the action of cyclical stress (or strain) can produce surface features that resemble a crack or a flaw (surface intrusions or extrusions). Continued cyclical stressing enhances these surface features and at some point, a surface crack is considered nucleated. This nucleation stage (stage I) is crystallographic in nature, being dictated by flow (slip) rather than by tensile fracture considerations. Thus, initial fatigue-crack plane is not normal to the principal tensile axis. When the stage I crack has grown to a certain critical size (determined by material properties and applied stress level and state), slow-crack growth (stage II) commences. In this stage, crack propagates in a direction normal to the principal axis. Crack propagation rate is defined by the range of alternating stress. Final fatigue fracture (Stage III) was discussed above.

Systematic analysis of a material's fatigue resistance requires the application of a well-characterized stress/strain cycle even though such a test may not simulate service very well. A cyclical tensile test where a specified stress amplitude is cyclically imposed on a finite mean stress is often used. For metals and alloys (unlike polymeric materials), the frequency of the applied stress doe not have an effect on fatigue resistance except if the frequency is very high (for example, > 200Hz). Although stress-controlled tests are traditional, because of the important role of plasticity in fatigue, it is fundamentally more revealing to assess a material's fatigue response under conditions of a specified cyclically applied strain, rather than stress. The results from stress-controlled tests are plotted as an S-N curve where S is the stress amplitude and N is the number of cycles to failure. In ferrous alloys, there exists a stress amplitude below which fracture will not take place regardless of the number of stress cycles. This is called the fatigue limit or endurance limit. In non-ferrous alloys, a fatigue limit is not readily manifested and as a consequence, the stress amplitude required to cause failure at a very large number of cycles (e.g. $N = 10^8$) is used as a design parameter. The fatigue limit (and the critical stress amplitude) are altered by the magnitude of the mean stress. As the mean stress increases, the fatigue limit decreases. Several empirical engineering estimates have been developed that relate the fatigue limit to the mean stress, one such being due to Goodman. The Goodman equation is written as

$$\sigma_a = \sigma f_{at}(1-\sigma_{mean}/\text{tensile strength})$$

where σ_{fat} is the fatigue limit appropriate to $\sigma_{mean} = 0$.

The notion that plastic strains are responsible for cyclic damage was established by Coffin [3] and Manson [4] independently in 1954. They proposed an empirical relationship between the number of load reversals to fatigue failure and the plastic strain amplitude. This so called Coffin-Manson relationship has remained the most widely used approach for the strain-based characterization of fatigue. Cyclical stress and cyclical strain tests are related. During high-cycle fatigue (regime where number of cycles to failure is large, typically much greater than 10^3), the macroscopic stress level is such that the structure as a whole undergoes only elastic deformation and in this regime, stress and strain ranges are related through the elastic modulus (note: at the microscopic level, the fatigue process still involves plastic deformation for example, due to initiation at stress concentrators). In the low-cycle fatigue range ($N_f < 10^3$), the material is typically subjected to macroscopic as well as microscopic plastic strain. For relatively low values of N_f, the plastic strain range is much greater than the elastic range so that total $\Delta\varepsilon \approx \Delta\varepsilon_{pl}$. $\Delta\varepsilon_{pl}$ can be related to $\Delta\sigma$ by knowing the material's cyclic hardening response. Different material properties are desirable for low cycle fatigue (LCF) versus high cycle fatigue (HCF) applications. A high ductility is desirable for low-cycle applications because fatigue cracks are nucleated early on in the material's life. Since slow crack growth is critical to fatigue life, adequate work hardening and good ductility are essential. In contrast, crack nucleation should be delayed for materials intended to perform safely over a large number of stress or strain reversals. This can be accomplished by using high strength materials with minimal stress concentrators.

Slow crack growth occupies a large fraction of a material's LCF life. Because of this, tests have been developed to monitor the Stage II crack-growth rate as it depends on crack size and stress range. In addition to providing data that allows estimation of LCF lifetimes, these tests are also useful for shedding light on the mechanisms responsible for Stage II crack growth. Measurement of Stage II crack growth rate involves subjecting a precracked specimen to a fixed stress (or strain) amplitude at a specified mean stress or stress ration, and then monitoring the crack length as a function of number of cycles. Crack length can be measured using an optical microscope or indirectly using electrical resistance measurement across the crack. In such a test, the rate of crack advance (typically denoted as *da*/*d*N where *a* is the crack length and N is the number of cycles) increases with increasing crack size. Further, for a fixed stress range, crack advance is promoted by higher values of the stress ratio (often denoted by R) implying that the mean stress, and more importantly, the maximum tensile stress has a pronounced effect on crack growth. Results from several studies on a variety of materials have shown that for a given material and stress ratio, Stage II crack-growth rates are a unique function of $\Delta K(\sim\Delta\sigma(a)^{0.5})$ and over an appreciable range of this variable, *da*/*d*N is related to it by *da*/*d*N $\sim A(\Delta K)^m$, where A is a constant that depends on the material and stress ratio, asnd 'm' is an empirical constant lying between 2 and 7, and deduced from crack-growth rate measurements. It however must be emphasized that this power-law relationship holds only over a portion of the *da*/*d*N - ΔK curve.

A schematic *da*/*d*N-ΔK plot is shown below in Figure 1. The effect of changing the stress ratio, R ($R = \sigma_{min}/\sigma_{max}$) on the response is shown through the two schematic curves for two different R values ($R_1 > R_2$). At very low ΔK, *da*/*d*N becomes very small so much so that in fact, below a certain critical stress intensity factor denoted as ΔK threshold (ΔK_{th}), Stage II cracks will not propagate. As R increases, ΔK_{th} decreases. In Region II, the crack growth rate - ΔK relationship is described by the power-law equation given above and this yields a straight line on the log-log plot shown in Figure 1. Although *da*/*d*N increases with R in Region II it is much less sensitive than in Region I. Once again in Region III, crack growth rates are sensitive to R where high ΔK values promote rapid Stage II crack-growth rates. Fracture takes place when $K_{max} = K_{Ic}$, and clearly, for a given stress amplitude, K_{Ic} decreases as R increases.

The threshold stress intensity factor, ΔK_{th}, represents inherently safe design against fatigue fracture but the value is usually so low compared to critical stress intensities that use of engineering materials at such low DK values represents a great restriction on their effective utilization. Current engineering design therefore is to accept the presence of fatigue cracks in most structures, to assume that some of them will propagate, but to insure also that they will not grow to catastrophic length during the intended lifetime of the part.

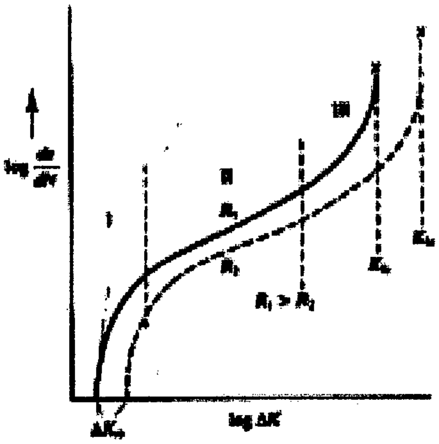

Figure 1: Schematic of crack-growth rate as a function of the cyclical stress intensity factor ΔK for different R-values.

As crack growth rates change, fracture morphology changes too. At high ΔK values, crack advance is often accomplished in a tensile-like mode and the striations typical of fatigue failure are not usually evident. Likewise, at low values of ΔK, fatigue striations are not frequently seen. It is only in Region II that fatigue striations are clearly seen. Measurement of striation spacings provide a confirmation of the *da*/*d*N values obtained by other techniques. Perhaps surprising is the fact that microstructure plays a minor role in determining Stage II fatigue-crack-growth rates in metals and alloys. On the other hand, correlation of crack-growth rates with the elastic modulus , a structure-insensitive property, has been successfully made. However, at high ΔK values, microstructrure does influence crack-growth-rates and factors promoting high fracture toughness also reduce Stage II crack-growth-rates. One reason for the lack of correlation of structure and tensile properties with fatigue crack propagation rates is that materials respond differently to cyclically imposed stresses (and strains) from the way they do to tensile monotnic stresses. The cyclic stress-strain behavior of materials heat treated to quite different tensile yield strengths usually differ much less than their tensile flow curves. Thus, a knowledge of cyclic stress-strain response of a material enhances the understanding of the fatigue process and data obtained from such studies are useful for engineering design against fatigue.

The response of a material to cyclical mechanical environment can be assessed by subjecting it to either a specified cyclical stress or strain amplitude. The latter is more commonly done and the results from this kind of test (a fixed strain amplitude that includes a component of plastic strain) demonstrates that a material may either soften (i.e. stress amplitude decreases with time) or harden (stress amplitude increases with the number of cycles), and the extent is a function of the plastic strain range, $\Delta\varepsilon_{pl}$.

In the case where the material cyclically hardens, the stress amplitude required to maintain the specified strain range increases with the number of cycles and is manifested by an increase in the area of the hysteresis loop. The converse is true for a material that softens. The extent and rate of hardening or softening can be scertained by plotting the stress amplitude against the number of cycles. After a certain number of cycles, typically 100 or so, the stress amplitude attains a constant value. This response clearly illustrates the inadequacy of using tensile properties in fatigue design, particularly when the material exhibits cyclic strain softening. Typically, a material in a "soft" condition (example - well annealed) would tend to cyclically harden whereas the material is in a "hard" condition, it tends to cyclically soften. It should however be noted that some materials in a given condition can harden over certain strain regimes and soften over others. The nature of crystallographic slip in the material influences the extent and rate at which softening or hardening occurs. As a general rule, materials that exhibit wavy slip (as opposed to planar slip) exhibit cyclical stress-strain curves that are independent of the materials starting condition - i.e. history independent. In contrast, materials that exhibit planar slip characteristics (e.g. low stacking fault energy materials) are history dependent. A cyclical stress-strain curve (as opposed to a monotonic stress-strain curve) is the locus of points representing the steady-state stress amplitude as a function of the plastic strain range (usually $\Delta\varepsilon_{pl}/2$), and is obtained by subjecting a number of samples of the alloy to be examined to varying plastic strain ranges until the steady state hysteresis loop is obtained. A curve drawn through the loop tips defines the cyclical stress-strain curve and such a curve is usually very different from a montonic stress-strain curve.

Relevant to this proposal are ideas and theories relating to creep-fatigue interactions. In considering such interactions, the role of environment (i.e. oxidation) also needs attention as it plays a key role in "real-life" failure. Whether this topic should be viewed as creep enhanced by the fatigue environment or vice versa depends on the operational conditions. Thus, when the cyclical stress (or strain) amplitude is small in comparison to the mean stress/strain or the applied frequency is low and/or the temperature is high, it is proper to view the phenomenon as one of creep perturbed by fatigue. In conditions opposite to these (for example, lower temperatures and higher frequencies), we consider failure as due to fatigue and accelerated by diffusional processes. Empirical creep-fatigue correlations have been developed, an example being the linear combination of Robinson's rule for creep fracture with the Palmgren-Miner rule for fatigue [5], which is conservative for cyclically hardening materials but "unsafe" for materials that cyclically soften. Empirical relations have also been developed that take environment into consideration and one such relationship is given below:

$$\Delta\varepsilon_{pl}[(N_f)(\nu)^{k-1}]^{c'} = \text{constant}$$

In this equation, c' and k are empirical constants. $\Delta\varepsilon_{pl}$ is the plastic strain range, N_f is the cycles to failure and ν is the frequency of the fatigue cycle. The constant K is environment sensitive, being taken as unity for vacuum and less than one (~0.8) for air. Fatigue fracture maps have been used to present creep versus fatigue versus tensile fracture and the interaction between these failure modes [6].

Finally, it is pertinent to recognize that BCC refractory metals (Nb,Ta, Mo, and W) exhibit S-N curves that have forms similar to those of iron and the fatigue limit is reached prior to 10^7 cycles [7]. Another interesting feature that has been confirmed is that the ratio of Fatigue limit to the ultimate tensile strength is in the range 0.5-0.8 for the BCC refractory metals as contrasted to FCC and HCP structures where the ratio is 0.3-0.4. This difference has been attributed to the high friction stress and easy cross slip characteristics of BCC metals.

2.2 *Molybdenum-Based Alloys for High-Temperature Applications*

The element molybdenum (Mo) exhibits a high melting point (2610°C), low vapor pressure at high temperatures, high strength and stiffness at high temperatures, and excellent resistance to corrosion in a variety of media. Together with its beneficial nuclear and electrical properties and high thermal conductivity, Mo and its alloys have been successful in finding several industrial applications. Mo and its alloys are typically produced either by the ingot metallurgy (I/M) route or by powder metallurgy (P/M) processing. Pure Mo for example is produced by the vacuum arc casting (VAC) process where high purity Mo powder is pressed into an electrode, sintered at high temperature and then continuously melted to fill a water-cooled copper mold, the entire operation being performed in vacuum. The resulting ingot is usually hot-worked into a useful wrought product. Alternately, elemental Mo can also be produced as a pressed and sintered P/M product that is then warm-worked into a useful product shape [8].

Mo-base alloys offer many advantages over pure Mo including physical and mechanical properties benefits. The compositions of the main Mo-base alloys in the United States are provided in Table I along with the principal producers. Some of these alloys are produced by the I/M arc-casting route as well as the powder route whereas others are produced only via P/M.

Table I: Mo-base Alloys available in the United States [7-9].

Name	Composition	Producer	Production Route	Ref.
TZM Alloy	Mo–0.5Ti–0.08Zr-0.02C	Climax Moly	I/M and P/M	[9]
TZC Alloy	Mo–1.2Ti–0.25Zr-0.15C	Climax Moly	P/M	[9]
MHC Alloy	Mo-2.0Hf-0.2C	Climax Moly	P/M	[9]
MT-104	Mo-0.5Ti-0.08Zr-110 ppm C	Osram Sylvania*	P/M	[10]
HCM	Mo-1.1Hf-735 ppm C	Osram Sylvania	P/M	[10]
HWM-25	Mo-25W-1.0Hf-345 ppm C	Osram Sylvania	P/M	[10]

* previously GTE Corporation

Of these different alloys, the alloy with TZM composition (i.e. MT-104 also which is a P/M version) has been the main-stay Mo-base alloy. This alloy is produced by I/M and P/M techniques, and Briggs and Barr [11] have discussed in detail the physical, chemical and mechanical properties and a variety of applications for arc-cast TZM alloy. The P/M version has a fine equiaxed grain structure in the as-sintered condition and segregation is significantly reduced. A comparison of the stress-rupture properties of the P/M-processed TZC and MHC alloys with those of arc-cast TZC and arc-cast TZM alloys [9] revealed that the P/M alloys were superior to arc-cast TZM but not as good as the Arc-cast TZC alloy. It is important to note however that even TZM alloys have superior high temperature properties compared to Ni-base superalloys. In this context, Jakobeit [12] has reported on efforts at Brown Boveri in Germany to examine P/M-processed TZM turbine blades for use in a high-capacity helium turbine for a direct-cycle high-temperature reactor. He has discussed various high temperature properties of this alloy including creep rupture and bending fatigue and the influence of processing on these properties. In addition to these alloys, there are reports in the Russian literature [13, 14] of evaluation of Mo-base alloys such as TsM-10 whose nominal composition is Mo-0.0024B-0.005Al-0.0027C and a Mo-Ti-Zr-C alloy with a nominal composition of Mo-0.1Ti-0.1Zr-0.004C. The fatigue response of these alloys are presented in the next section.

The effect of microstructure (and hence processing) on the tensile properties as well as creep-rupture characteristics of pure Mo and Mo-base alloys (TZM and TZC) has received adequate attention [9, 15-18]. Thus, the effect of recrystallization on stress-rupture response was evaluated by comparing TZM and TZC alloys in the stress-relieved and recrystallized conditions [15]. The study confirmed that the recrystallized microstructure was weaker than the stress-relieved material at low temperatures (e.g. 1000°C – 1100°C) and short times but was stronger at high temperatures (1300°C) and long times. Calderon et al [16] have compared the mechanical properties of vacuum arc melted TZM with those of P/M processed TZM and showed that while the steady state creep rates were comparable for the two materials, there was a significant scatter in values for the I/M material that was not the case for the P/M material. Fatigue measurements in load control at room temperature confirmed that the endurance limit for the two alloys were similar, lying at approximately 500 MPa; for stress amplitudes higher than the endurance limit, the number of cycles to fracture for the I/M alloy was higher than that for the P/M counterpart. Prior cold work appears to have minimal (if any) effect on fatigue response.

2.3 Mo-Si-B Alloys: Phase Equilibria

A series of papers from the University of Wisconsin, Madison by Perepezko and coworkers [19-23] has systematically documented the phase equilibria and associated microstructures for Mo-Si-B alloys rich in Mo and has further explored alloying strategies to produce enhanced oxidation resistance over a range of temperatures. Some of the findings are highlighted in [24].

A ternary isotherm at 1600°C is shown in Figure 2 below and is reproduced from [21] and a plethal diagram from [19] is reproduced in Figure 3. These diagrams illustrate the following pertinent features:

(i) The addition of B to a binary Mo-Si alloy enables the formation of a ternary silicide-boride, labeled the T2 phase in the diagram that is in equilibrium with the terminal Mo solid solution.

(ii) It is possible to produce a three-phase alloy consisting of Mo solid solution, T2 and Mo_3Si that are thermodynamically stable at high temperatures.

(iii) The solubility of Si and B in Mo is fairly low at room temperature, that for B being considerably lower relative to Si; more importantly, this low solubility is also maintained to very high temperatures (>2000°C); further, limited experimental evidence suggests sluggish diffusion at high temperatures. Together, these features imply a kinetically stable microstructure at high temperatures. While this is beneficial in service, it also implies a reduction in processing flexibility and difficulties in manipulating the microstructure in the solid state.

Systematic studies of a range of compositions in this ternary system (and following further alloying) have however demonstrated the ability to generate a spectrum of microstructures upon controlled cooling and judicious alloy composition selection (for example, see Figures 7-9 in Ref. [23]). The T2 phase has the $D8_1$ structure (body centered tetragonal) with 32 atoms per unit cell and exists over a range of compositions (i.e. off-stoichiometric compositions are possible). The two-phase T2 + Mo solid solution region as well as the three-phase T2 + Mo solid solution + Mo_3Si region adjacent to it on the B-lean side offer the possibility of varying the ratio of matrix phase (Mo solid solution) and intermetallic phase(s) extensively.

Ingot metallurgy (I/M) and powder metallurgy routes are being explored to produce these Mo-Si-B alloys. The high processing temperatures (melting and hot working) and metal reactivity with the container and the environment have posed (and continue to do so) significant challenges in the production of these alloys with reproducible chemistry and homogeneous microstructures. The ingot route has been examined to directly produce billets for hot working, as well as to provide feedstock for powder processes such as the Plasma Rotating Electrode Process (PREP). Difficulties in ingot processing include chemistry control and the production of crack-free ingots. Arc-melt buttons and bars and vacuum arc remelted ingots (from PMTI, Pittsburgh) are all being examined as possible starting material i) for subsequent hot working, ii) to produce alloy powders or iii) to serve as an electrode for PREP or similar processes.

In considering the P/M route, as briefly stated above, PREP was successfully used in the past few years to produce reasonable quality powders . The resulting PREP powder was then canned in Nb containers, HIPed and subsequently isothermally forged into "pancakes" to produce a fully-dense worked structure. *This is the processing route used to generate the two- phase alloy being examined in the current effort* and the resulting microstructures for this material are presented and discussed in the Results Chapters (Chapters 5 and 6).

The hot-working operations (be it isothermal forging or hot extrusion of canned powders) have also posed processing challenges. The relatively high hot-working temperatures and load capacity that are needed, particularly for three-phase alloys containing a high volume fraction of the intermetallic phase(s), have caused issues relating to stalling of presses (insufficient press capacity) and breakage of die and tooling prior to accomplishing the desired level of reduction. These issues have made it necessary to develop multiple hot working steps to achieve the desired levels of hot work and associated microstructures.

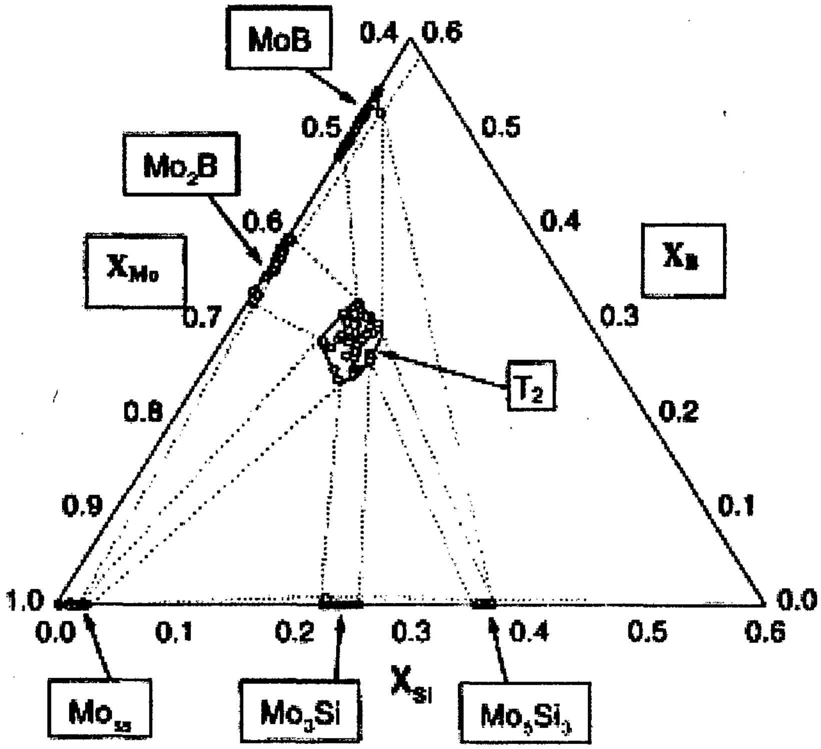

Figure 2. Isothermal section at 1600°C for the Mo-rich portion of Mo-Si-B system

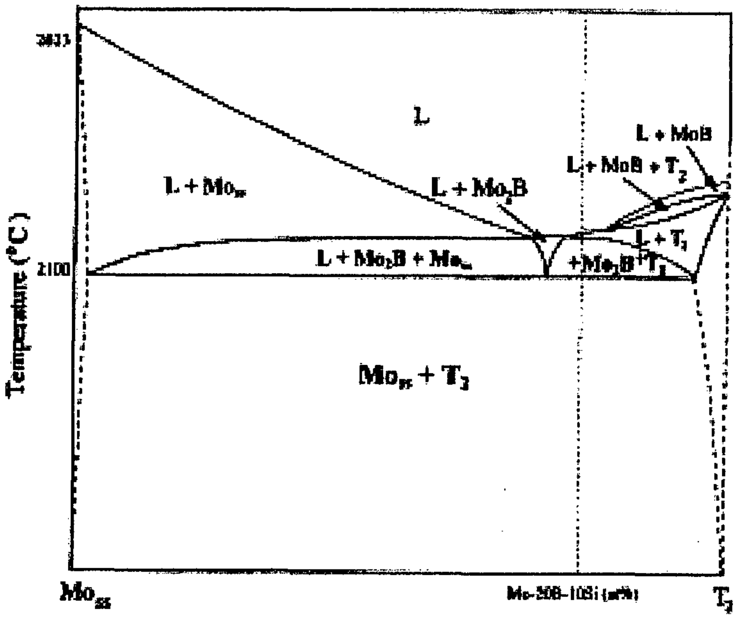

Figure 3: A plethal diagram illustrating the stability of the co-existing phases

One major difficulty in developing desirable microstructures in alloys lying in the two-phase Mo solid solution-T2 phase field is the extensive segregation during solidification by the formation of primary borides. Strategies to eliminate this problem include rapid solidification to suppress their formation, and by selective alloying to alter the solidification pathway [11]. Thus, it has been shown that systematic Nb substitution for Mo is effective in suppressing the formation of primary Mo_2B and producing a two phase (Mo,Nb) solid solution and T2 directly from the melt. In the case of three-phase alloys (Mo solid solution + T2 + Mo_3Si), the substitution of Nb or W for Mo can be effective in eliminating the Mo_3Si phase and instead in producing a three-phase mixture that includes Mo_5Si_3 (T1) phase, and thus a three-phase eutectic microstructure is possible in the quaternary systems. This feature creates the opportunity to produce a variety of eutectic microstructures that are not possible in the ternary Mo-Si-B system [23]. Thus, in the Mo-Si-B system, the alloying strategy is a viable option to alter solidification pathways to produce novel and interesting microstructures.

2.4 Mo-Si-B Alloys: Mechanical Properties

2.4.1 Single-phase alloys:

Ito et al [25] grew *single crystals* of the T2 phase using the floating zone process and characterized its physical and mechanical properties as well as the operating slip systems that enable high temperature plastic deformation. Deformation of the single crystals was carried out at 1500°C in five different orientations ([001], [010], [110], [443] and [021]). Plastic deformation was observed for [021] and [443]. Dislocation analysis on specimens oriented in the [021] orientation confirmed that slip occurred on the [001]{010} system but not on the <100>(001) system as previously reported [26]. The steady state creep rate was reported as being low and of the order of $3 \times 10^{-8}\ s^{-1}$ at 1500°C for a stress level of 432 MPa. The activation energy and stress exponent were reported as ~740 kJ/mol and 6.8 respectively.

The creep behavior of *single crystal* Mo_5Si_3 has been examined in the [314] orientation, (an activation energy of 510 kJ/mol and a stress exponent of 6 was reported [27]), and this compound has been shown to be less creep resistant than T2 [22,25]. Yoshimi et al [28] have examined the yielding and flow characteristics of the single crystals of Mo_5Si_3 in compression in the temperature range of 1200°C – 1450°C using a nominal strain rate of $1.7 \times 10^{-4}\ s^{-1}$. Brittle failure was noted for the near-[101] oriented sample at 1200°C whereas at 1250°C and above, a large yield drop was observed , producing an upper and a lower yield point point. The lower yield stress and flow stress were reported to be strongly strain rate sensitive. Similar behavior was also noted for specimens with [101] orientation but not for the [001] orientation. The variation of upper yield stress for the three orientations with test temperature was determined. A stress exponent of 6 and an activation enthalpy of 4.5 eV was reported for the {101] orientation and these high values were attributed to the high Peierls stress expected of the complex crystal structure.

There are at least two papers that have reported on the physical and mechanical properties of the Mo_3Si phase [29, 30]. In the first of these two papers [29], Rosales and Schneibel arc-melted binary Mo-Si alloys with Si levels ranging from 22 to 28 at.% and drop-cast the molten metal into water-cooled copper molds. Specimens were annealed at 1600°C for 24h and slow cooled to room temperature. Whereas the specimen containing 22 at.% Si contained a-Mo precipitates at grain boundaries of the Mo_3Si matrix, the specimen with 25 at.% Si contained small particles of Mo_5Si_3 within the matrix. The alloy with the composition Mo-24 at.% Si was single phase. Notched three-point bend bar specimens (without a fatigue precrack) yielded a toughness value of ~3 MPa√m. Compression tests at 1400°C over the strain rate regime 10^{-3} s^{-1} to 10^{-5} s^{-1} yielded 0.2% offset stress values ranging from 600 MPa to 100 MPa respectively. Subsequently, single crystal specimens of the Mo_3Si phase were grown using an optical float zone furnace [30] with a growth direction near <102>. Nanoindentation studies yielded elastic constants of $C_{11} = 505\pm35$ GPa, $C_{12}=80\pm60$ GPa and $C_{44} = 130\pm15$ GPa. Non-contact AFM images obtained from the regions around the indents revealed pile-up of material that appeared consistent with {100}(010) slip.

To the best of our knowledge, nothing is known about the mechanical properties of the α-Mo (containing Si and B) solid solution phase.

2.4.2 Two-phase alloys:

Two-phase alloys composed of the Mo solid solution and the T2 phase have been examined for their mechanical properties [31-33]. The specific alloy composition examined in [31] by Ito et al was Mo-9Si-18B (at.%) and contained approximately 28 volume percent of the Mo solid solution phase, the rest being the T2 phase. The alloy is part of a eutectic system and was obtained by directional solidification at a growth rate of less than 5 mm/h. The solid solution phase exhibits two types of microstructures: coarse particles and short rod-type morphology. T2 is the continuous phase. Compression tests conducted on the Mo-9Si-18B (at.%) alloy at a nominal strain rate of 1 x 10^{-4} s^{-1} confirmed brittle failure at stress levels of 1.5 –2.0 GPa between RT and 1000°C. Above 1000°C, the material displayed compressive plasticity with a peak flow stress of ~1 GPa in the 1000°C-1200°C regime followed by flow softening. At 1500°C, the peak stress dropped to about 700 MPa. Even after the 1500°C deformation, the matrix T2 phase was reported to show significant microcracking. Three-point bend tests at room temperature using notched specimens provided K_Q values of ~11 MPa√m, which is significantly higher than the value of 1-2 MPa√m reported for single phase T2 by Ihara et al [32].

Yoshimi et al [33] have published the results of a systematic investigation of the effect of the volume fraction of the Mo solid solution phase in Mo + T2 two-phase alloys on thermal expansion, compressive yield strength and oxidation resistance. The alloys were produced by arc-melting and the resulting buttons were not further hot-worked. The volume fractions of Mo solid solution phase in the four alloy compositions they examined were 0.72, 0.52, 0.34 and 0.2. They found that at a given test temperature, compressive yield strength progressively increased with decreasing volume fraction of the Mo solid solution phase; however, the alloy containing 0.34 (and 0.2) volume fraction of the solid solution phase did not show compressive ductility up to temperatures as high as 1500°C.

2.4.3 Three-phase alloys:

Investigations have also been conducted on the monotonic and cyclic properties of three phase alloys in the Mo-Si-B system with and without further alloying. These studies can be subdivided into two groups: those that pertain to the Mo solid solution + T2 + Mo_3Si phase field and others that correspond to the adjacent three phase field composed of Mo_3Si + T2 + T1 (Mo_5Si_3). In the interest of brevity, we focus our attention only on the first of these two groups – that relating to the alloys lying in the Mo solid solution + T2 + Mo_3Si phase field.

Schneibel and coworkers have published the results of their efforts on assessing the oxidation resistance, fracture toughness and creep resistance of several three-phase alloys with varying levels of the Mo solid solution phase [34-38]. Their alloys were produced using the casting route as well as by powder processing. Their results demonstrate that the fracture toughness at room temperature increases from about 3 MPa√m for a material containing negligible volume fraction of the Mo solid solution phase to about 15 MPa√m for a material containing 38 percent of the Mo solid solution phase when a powder-processing route is adopted. They have also studied the effect of alloying and claim that Nb is a better alloying substitution for Mo than W in terms of improving creep resistance. Ito et al [29] however have demonstrated that directionally solidified three-phase alloys with the eutectic morphology derived from quaternary compositions of the type Mo-30.4Nb-19.5Si-4.5B (at.%) and Mo-38.8Nb-19.5Si-3B (at.%) have lower fracture toughness at room temperature (5-6 MPa√m) than a ternary two-phase alloy like Mo-9Si-18B (11 MPa√m).

The only high temperature evaluation of these alloys using tensile specimens that appears to be reported in the literature is that due to Nieh et al [39]. The composition examined was Mo-9.4Si-13.8B (at.%) and the alloy was produced by powder-processing (mixing of elemental powders and hot pressing). Tensile specimens were electro-discharge machined and tested at strain rates between 10^{-4} s^{-1} and 5 x 10^{-3} s^{-1} in the temperature interval 1350°C – 1550°C. A stress exponent of 2.8 and an activation energy value of 740 kJ/mol were reported. At a strain rate of 10^{-4} s^{-1} and a temperature of 1400°C, a tensile elongation of 150% was realized. The tensile ductility however was reported to decrease rapidly with increasing strain rate and decreasing temperature; thus at 1350°C for the same strain rate, tensile elongation to failure was reported as 25% and it dropped to 20% when the strain rate was increased by an order of magnitude.

To the best of our knowledge, there has been only one group as yet that has reported on the cyclic loading response of three-phase Mo-Si-B alloys. Choe et al [40] examined the crack growth behavior under cyclic loading of a three-phase Mo-12Si-8.5B alloy (38% of the Mo solid solution phase) using disk-shaped compact tension specimens that contained large cracks (>3 mm); they cycled them at $R = 0.1$ using a sinusoidal wave form and conducted such tests at 25°C, 800°C, 1200°C and 1300°C. At room temperature, the ΔK_{th} was ~5 MPa√m and the Paris slope was characteristic of a brittle material (m ~60). At 1200°C, the threshold increased to ~7MPa√m and the Paris slope was still reported to be high at ~55. A variety of mechanisms was invoked to explain the fatigue crack growth process. Subsequently, Choe et al [41] characterized the fracture toughness and fatigue response of four Mo-Si-B three-phase alloys produced by ingot metallurgy and powder metallurgy routes and demonstrated that both properties were superior for the ingot metallurgy materials; they ascribed this difference to the coarser distribution of the Mo solid solution phase in the ingot metallurgy processed material.

2.5 *Summary and Unresolved Issues*

From the above discussion it is evident that there is a demand for structural materials, in the aerospace and aircraft industry that can withstand service temperatures beyond the capability of Ni-based superalloysand that The use of existing commercial refractory metals and alloys (like TZM, or a modified version of it), refractory intermetallics (e.g. $MoSi_2$) and ceramics appears unlikely due to an inadequate combination of high temperature creep resistance, oxidation resistance and ambient and warm-temperature damage tolerance.

Research is ongoing in evaluating novel, multiphase refractory alloys and in-situ composite systems based on a refractory metal matrix such as Nb and Mo. Specifically, systems of current interest include the Mo-Si-B and the Nb-Si-X, families of alloys. In both these systems, several challenges remain in the domains of (i) alloy composition and microstructure optimization (i.e. alloy design),

(ii) processing of these alloys including molten metal containment, and die and tool materials selection and design, (iii) issues related to scale up, and (iv) detailed characterization of the microstructure and mechanical properties of these alloys and understanding their inter-relationships. Thus, Mo-Si-B alloys are being produced by both I/M and P/M routes (although at present, powder processing is the preferred route) and these exhibit excellent high-temperature creep strength and good oxidation resistance at temperatures above 1000°C but "pests" (an oxidation phenomenon) at lower temperatures (around 700°C). Alloying approaches have now been developed to offset this intermediate temperature "pesting" problem.A limited number of studies have been conducted to characterize the high temperature compression and tension response and the low temperature toughness of a few of these Mo-Si-B alloys, but in the various instances reported in the literature, the microstructure of the alloy before and after deformation has not been adequately characterized nor was the processing the same in all instances. For these alloys to be successfully used as a material to make rotating components in turbine engines, an understanding of the cyclic response as a function of temperature and environment is critical. Although there have been some studies on the fatigue behavior of Mo and Mo-base alloys at room and elevated temperature, particularly for TZM, in general there is paucity in fatigue data for Mo alloys and the limited data available pose reproducibility problems.

Limited work has been done on the Mo-Si-B alloy system in terms of evaluating the cyclic response. As discussed earlier, there has been only one effort so far reported in the published literature, by Ritchie and coworkers [40-42]. Those studies however have not systematically characterized the role of microstructure and prior deformation on fatigue response, particularly with respect to crack growth behavior, the role of creep in influencing the cyclic response, and the effect of environment on these properties.

It is the intent of this study to fill some of the gaps in the literature on these Mo-Si-B alloys. Detailed experiments were carried out on Mo-2Si-1B in weight percent (Mo-6Si-8B in atomic percent) to understand the cyclic response of the alloy as a function of temperature both in vacuum (20°C-600°C) and in air (20°C-1400°C). The compression behavior of this alloy was examined in the temperature range of 800°C-1400°C at different strain rates to characterize the creep response of the alloy and to assist in interpreting the experimental observations that result as a consequence of the combined effect of fatigue and creep at elevated temperatures; likewise, monotonic crack growth behavior over the temperature range 20°C-1400°C was examined to understand the differences in crack growth characteristics during monotonic versus cyclic loading. Furthermore, similar studies were conducted on a commercially available Mo alloy, TZM, in order to establish a baseline for the purpose of comparison with the response of the Mo-Si-B alloy.

3.0 EXPERIMENTAL PROCEDURE

3.1 Material Preparation

Powders of a Mo-2wt.% Si-1wt.% B alloy (Mo-6Si-8B in at.%) were produced by the plasma rotating electrode process (PREP) and consolidated by hot isostatic pressing (HIPing) in Nb cans at 1760°C using a pressure of 200 MPa (in the rest of the paper, we refer to this alloy as the Mo-Si-B alloy). The resulting 120 mm tall compact was then subjected to isothermal forging at 1760°C and reduced to a "pancake" with a final thickness of 20 mm. An off-the-shelf, powder-metallurgy processed TZM plate (MT104) was obtained for baseline comparison.

3.2 Compression Studies

Cylindrical samples (5 mm diameter x 10 mm tall) were electro-discharge machined from the forged compact, with the long axis of the sample parallel to the direction of forging. Prior to testing, the ends of the samples were ground and polished flat and parallel to each other. Constant displacement tests in uniaxial compression at ambient temperature were carried out using a servo-hydraulic testing machine that yielded a nominal strain rate of 8.3×10^{-5}/sec. High-temperature compression tests were conducted at a constant displacement rate, in vacuum, in the temperature range of 800-1400°C, and in the strain-rate regime of 10^{-4} to 10^{-7} /sec. Samples were deformed between silicon carbide platens and all tests were carried out in a vacuum better than 10^{-6} Pa. Load-displacement data were monitored and tests were performed till a steady-state load with increasing displacement was attained. Plastic strain in each sample at the end of the test, as measured by change in specimen height, was in the 5 – 7% range.

To understand the contribution to yield strength from the Mo matrix solid solution, we conducted microhardness measurements on the Mo solid solution "islands" in these alloys and compared them to microhardness values for TZM as well as pure Mo (microhardness measurements were made using 500g load and reported values are Vickers Hardness Numbers, VHN).

Microstructure of the samples was characterized before and after the high-temperature tests by optical, scanning (SEM) and transmission electron microscopy (TEM). Samples were etched with Murakami's etch (aqueous solution of potassium ferricyanide and sodium hydroxide) for optical and SEM. Thin foils of compression-tested specimens for TEM observations were made from slices that were taken perpendicular to the loading direction. Final thinning and perforation of the foils was accomplished by twin-jet electropolishing in a solution of methanol and 12.5 volume% sulfuric acid at –30°C using 30 V. The specimens were examined in a Philips 420 transmission electron microscope operating at 120 kV using bright field and selected area diffraction (SAD) techniques.

The compression response of the two-phase Mo-2Si-1B alloy was also investigated via finite element modeling (FEM) with microstructure information being incorporated. Representative optical micrographs of the as-forged Mo-2Si-1B alloy were scanned to capture the size, shape, distribution and spacing characteristics of the T2 particles in the Mo solid solution matrix. Each scanned micrograph was then digitized and meshed into an FEM model. Both phases were assigned constitutive relations obtained from experimental observations at various temperatures and loading rates. As the mechanical properties of the Mo solid solution (containing Si and B) matrix is currently unknown, the properties of pure Mo was approximated in the simulation and these were obtained from the literature [34] for 300K and 1000K at a strain rate of 10^{-3} s^{-1}. The Mo solid solution phase was treated as elastic-plastic; at 300K, the yield strength was taken as 700 MPa with a linear work-hardening rate (expressed as $d\sigma_t/d\varepsilon_t$) of ~700 MPa, whereas at 1000K, the values for yield strength and work-hardening rate were 400 MPa and ~200 MPa respectively. The T2 phase was considered as being both elastic as well as elastic-plastic. Data for the plastic response of T2 were obtained from the work of Ito et al [25] where single crystals of the T2 phase were shown to deform plastically at 1550°C when deformed in compression in the [042] orientation. Thus, three distinctly different cases were evaluated that could be thought of as corresponding to temperature (and/or strain rate) effects: i) matrix strength and work hardening rate are high and particles are elastic, representing a relatively low-temperature situation, ii) matrix strength and work-hardening rate are lower, particle is still elastic – a situation that could correspond to an intermediate-temperature regime, and iii) matrix strength and work-hardening rate are low and particle exhibits plasticity, a siutation representing the high-temperature extreme. Since the matrix properties (for pure Mo) were not available at 1550°C, the data for 1000K were used for the case where T2 was assumed to show plasticity.

Commercially available FEM package (ABAQUS 6.3.1) was used to achieve uniaxial compression of 10% engineering strain with subsequent complete unloading. The friction between the material face and the compression block was assumed to be negligible, and thus sliding of the material block was allowed. At maximum compression, various contour plots of plastic equivalent strain and Mises stress were extracted to show the distribution and interaction between the two phases. In this paper, the FEM model is 2D with the bottom face vertically constrained and the top face uniaxially compressed. Three different mesh sizes were examined (120 x 120, 240 x 240, and 480 x 480) and it was determined that the 240 x 240 mesh adequately captured the situation.

3.3 Isothermal Oxidation studies

To assess the ability to perform monotonic and cyclic crack growth measurements in air as a function of temperature, preliminary isothermal oxidation tests were conducted in the temperature range of 300°C – 1200°C using 10mm x 10mm x 3mm samples. The samples were polished, cleaned and dried before placing them in alumina boats in a box furnace in atmospheric air. The samples were provided 24 hours of exposure at temperature, cooled to room temperature in the furnace and then weighed using a microbalance to measure weight changes.

3.4 Monotonic Crack Growth Studies

Monotonic crack growth studies were undertaken using notched and compression-compression fatigue pre-cracked three-point bend specimens (27 mm length x 6 mm height x 3 mm thick). These tests were conducted in air and in vacuum in the temperature range 20°C-600°C. Tests at higher temperatures up to 1400°C were conducted only in vacuum. Load-displacement data were extracted from these experiments and K_Q was calculated in each instance and reported as K_{IC} after verifying that the result met the required criteria to be valid. Resulting fracture surfaces were characterized using standard SEM techniques, and and appreciation for crack interaction with surface microstructure was obtained using interrupted tests in conjunction with optical metallography.

3.5 Stress-Number of Cycles to Failure (S-N) Studies

Hour-glass-shaped specimens for S-N tests (Figure 4a), whose dimensions were in accordance with ASTM E466-76, were machined using a combination of electrodischarge machining (to machine out the cylinders) and conventional grinding (to incorporate the gage and grip geometry) techniques. These samples had their longitudinal axis in the forging plane for the Mo-Si-B and in the long-transverse direction of the TZM plate. Tests for the Mo-Si-B alloy were conducted at room temperature (in air) and at 1200°C (in vacuum), whereas the TZM was evaluated only at room temperature. Tests were conducted in a tension-tension mode with R = 0.1 ($R = \sigma_{min}/\sigma_{max}$) and resulting fracture surfaces were characterized.

3.6 Cyclic Crack Growth Studies

Compact tension specimens to obtain fatigue crack growth response (Figure 4b) were also machined from both materials; in both cases, the plane of the specimen coincided with the forging/rolling plane. In the case of the TZM, care was taken to orient the notch in the long-transverse orientation of the plate, although a limited number of specimens were tested at room

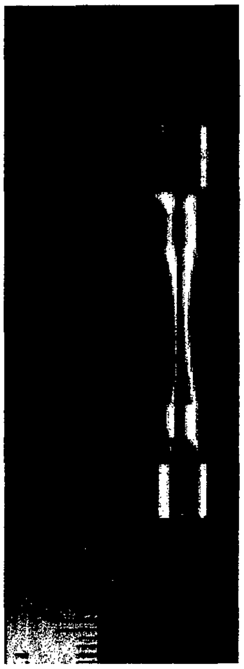

W = 25 mm; B = 3 mm; a = 5.3 mm
a_n = 5.0 mm; notch width = 1.5625 mm
root tip radius = 0.00635 mm

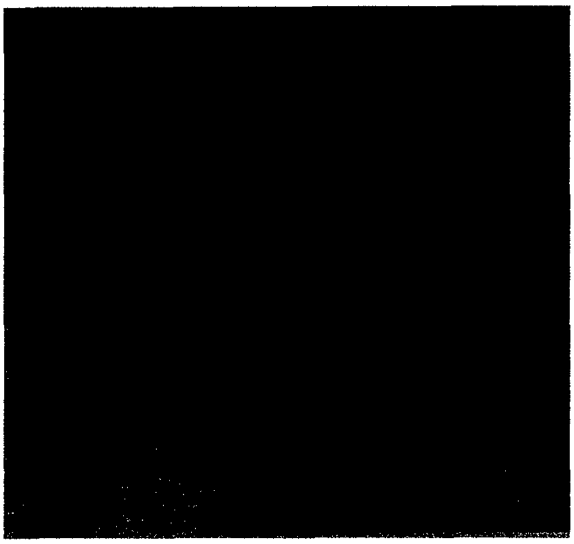

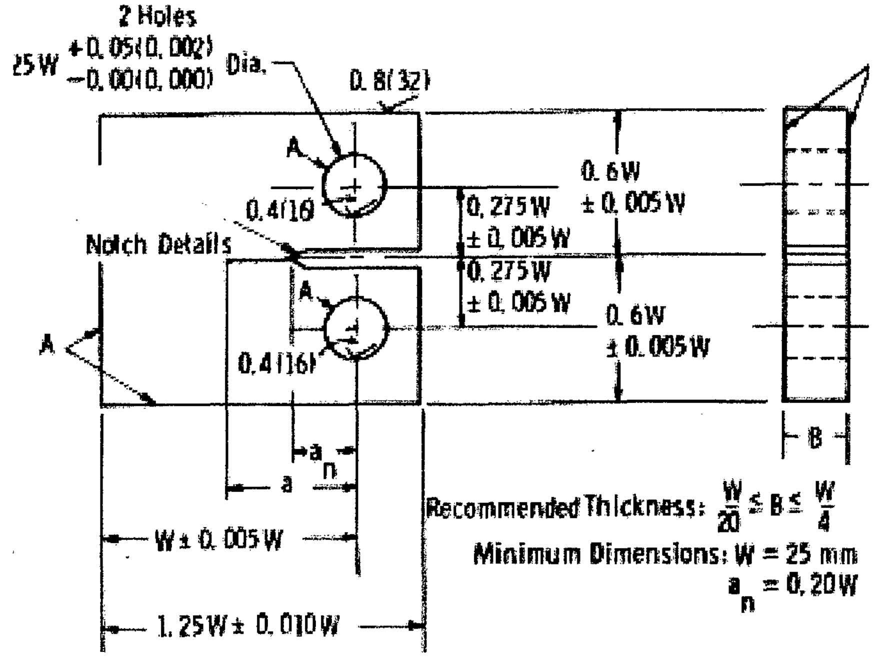
2 Holes
.25W +0.05(0.002) −0.00(0.000) Dia.
0.8(32)
A
0.4(16)
Notch Details
A
0.4(16)
A
0.275W ±0.005W
0.275W ±0.005W
0.6W ±0.005W
0.6W ±0.005W
a
a_n
W ± 0.005W
1.25W ± 0.010W
B
Recommended Thickness: $\frac{W}{20} \leq B \leq \frac{W}{4}$
Minimum Dimensions: W = 25 mm
a_n = 0.20W

(c)

Figure 4(a-c) Fatigue test specimen geometry: a) Hour-glass shaped S-N test specimen, b) Compact tension test specimen for cyclic crack growth studies, and c) ASTM compact tension specimen dimensions and requirements.

temperature with the notch oriented in the rolling direction of the plate. The dimensions of relevance for the compact tension specimen are given in Figure 4b and the allowed dimensional tolerances and permitted inter-relationships between the various dimensions in order to fully comply with ASTM specifications are provided in the drawing in Figure 4c. Fatigue precracks were introduced in these specimens in a compression-compression mode. Tests were initially conducted at room temperature on these materials and orientations using R=0.1 and R=0.2. Based on initial results, subsequent tests were limited at elevated temperatures to R=0.1; further, for the TZM plate, tests were confined to specimens that had the notch oriented in the long-transverse direction of the plate. These crack growth tests were conducted in air at room temperature, 300°C and 600°C. Isothermal oxidation studies revealed that tests at higher temperatures would need to be conducted in vacuum as the rate of material loss was significant and environmental effects at the crack tip would preclude an assessment of the intrinsic fatigue crack growth resistance of the material. Thus a series of crack growth tests were conducted in vacuum for both materials at R=0.1 in the temperature interval 600°C-1400°C. Crack growth increments following a specified number of cycles (either 20,000 or 25,000 cycles) at a fixed value of ΔK were obtained by interrupting the test. For the high temperature vacuum tests, care was taken to control the heating and cooling rates so as to minimize the effect of thermal shock on crack growth. Once again, the interaction of the advancing crack with the microstructure ahead of it was examined by optically imaging the surface microstructure in the region ahead of the main crack before and after increments of loading, and fracture surfaces obtained from these tests were examined in the scanning electron microscope using secondary and back-scattered electron imaging techniques.

4.0 HIGH-TEMPERATURE COMPRESSION RESPONSE

4.1 Initial Microstructure:

The as-received TZM plate (MT104) displayed a partially recrystallized structure (Figure 5a) with an extensive subgrain structure in regions that were unrecrystallized (Figure 5b). Within the sub-grains, a fairly high dislocation density in the form of well-organized networks as well as tangles is noted. Often isolated dislocations appeared to be pinned (Figure 5c) although the source of pinning is not evident (i.e jogs, solid solution or nanometer-scale precipitates). Fine precipitates are however observed in the matrix (Figure 5d) and these are thought to be titanium-zirconium monocarbides. In addition to these fine precipitates observed in Figure 5d, coarser ZrO_2 particles (5-10 μm in size) were frequently observed and likely arise as a consequence of powder processing; similar observations have been previously made [16].

The microstructure of the PREP powder was characterized and a representative SEM image of the cross-section of a particle is shown in Figure 6. A dendritic microstructure is observed in the particle, with dendrites being Mo solid solution and the interdendritic region composed of a eutectic exhibiting the "chinese script" morphology. The eutectic structure is thought to be composed of Mo solid solution and the T2 phase.

Optical and SEM examination combined with X-ray diffraction confirm that the isothermally forged Mo-Si-B alloy consists of a matrix Mo solid solution phase in which is dispersed the T2 phase, as discrete particles for the most part, although local "spherical islands" of highly interconnected T2 phase regions representing a high volume fraction are occasionally observed (Figure 7a). These local regions that are very rich in T2 content are thought to be a consequence of compositional inhomogeneity in the electrode used in the PREP process. These electrodes were prepared by blending elemental powders that were then hot consolidated and the segregation of powders during blending is likely the source of this problem. A measurement of the area fraction of T2 phase in the regions where the phase is present as discrete particles provides a value of 0.38; this is in reasonable agreement with phase diagram predictions for this alloy composition. Secondary electron imaging of the polished cross section in the SEM coupled with EDX analysis confirmed the occasional presence of silica (SiO_2) particles in the microstructure, and in the instances they were observed, they appeared to have occurred at the matrix/T2 interface. Backscattered electron imaging in the SEM however confirmed an alternating T2/silica lamellar morphology in certain regions that is reminiscent of a eutectic/eutectoid decomposition product, an example of which is shown in Figure 7b. The inset in Figure 7b shows an example of one such T2 particle containing the silica phase and it is seen that adjacent to the silica phase, within the T2 phase, fine precipitates are present. The identity of these precipitates remains unknown but it is

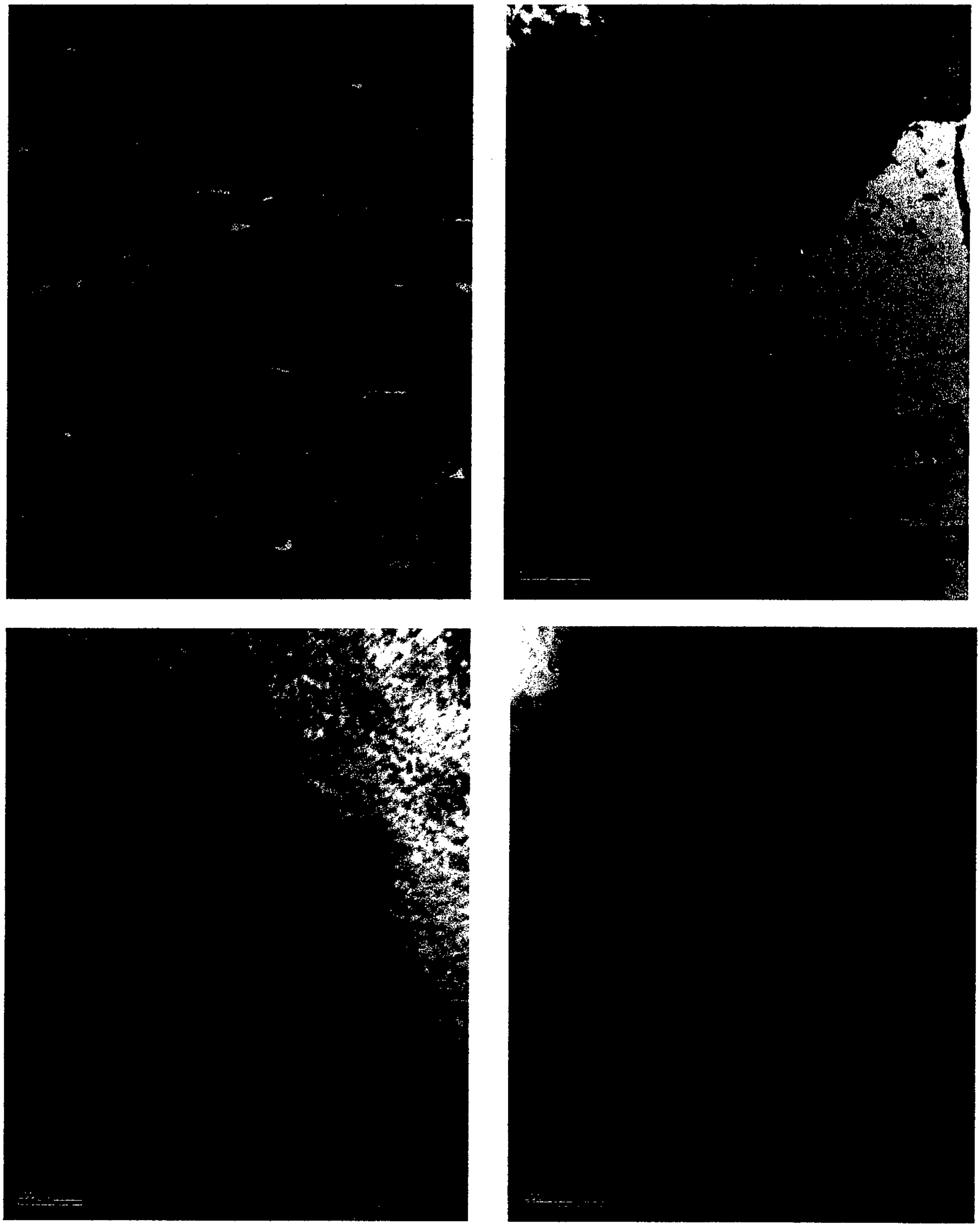

Figure 5 a-d: Microstructure of the as-received TZM plate showing a) partially recrystallized structure containing a dispersion of coarse carbides primarily at grain boundaries, and occasional coarse ZrO_2 particles, the latter being a consequence of the powder processing route, b) a well-developed substructure, c) dislocation pinning by jogs and carbide particles, and d) high-magnification image of the fine carbides within the grains.

argued that they occur as a consequence of the local depletion of silicon from the T2 phase. These fine precipitates are not observed within those T2 particles where the silica phase is not present.

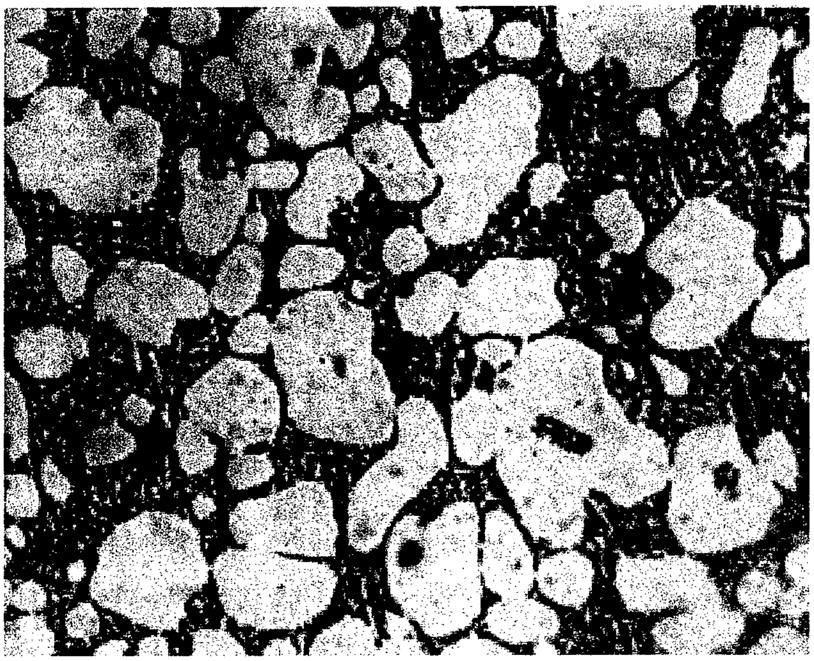

Figure 6: Cross-section of a PREP powder particle of the Mo-6.1Si-7.9B alloy showing dendrites of the Mo solid solution phase with fine two-phase mixture of Mo solid solution and the T2 phase between the primary dendrites.

A bright field image (Figure 7c) illustrating a grain boundary in the Mo solid solution phase and the T2/Mo solid solution interphase interface confirms that both boundaries are devoid of extraneous precipitate phases such as nitrides, borides or carbides (The bright band of uniform width observed in Figure 7c is an artifact of imaging and is a consequence of specimen thickness differences between the T2 phase and the Mo solid solution phase, resulting from the differential electropolishing response of the two phases). Selected area diffraction patterns confirmed the identity of the co-existing phases. Dislocations were not observed at these boundaries or within the T2 phase in the as-forged condition, although within the Mo solid solution phase, dislocation networks (Figure 7d) as well as tangles (Figure 7e) were observed.

4.2 Compression Response

The compressive yield stress of the Mo-Si-B alloy at room temperature was 1280 MPa whereas that for TZM was 620 MPa. In contrast, both materials failed elastically in uniaxial tension at approximately 300 MPa (when a tensile specimen with a rectangular cross-section was used). In both materials fracture occurs by transgranular cleavage. Subsequent to these initial observations,

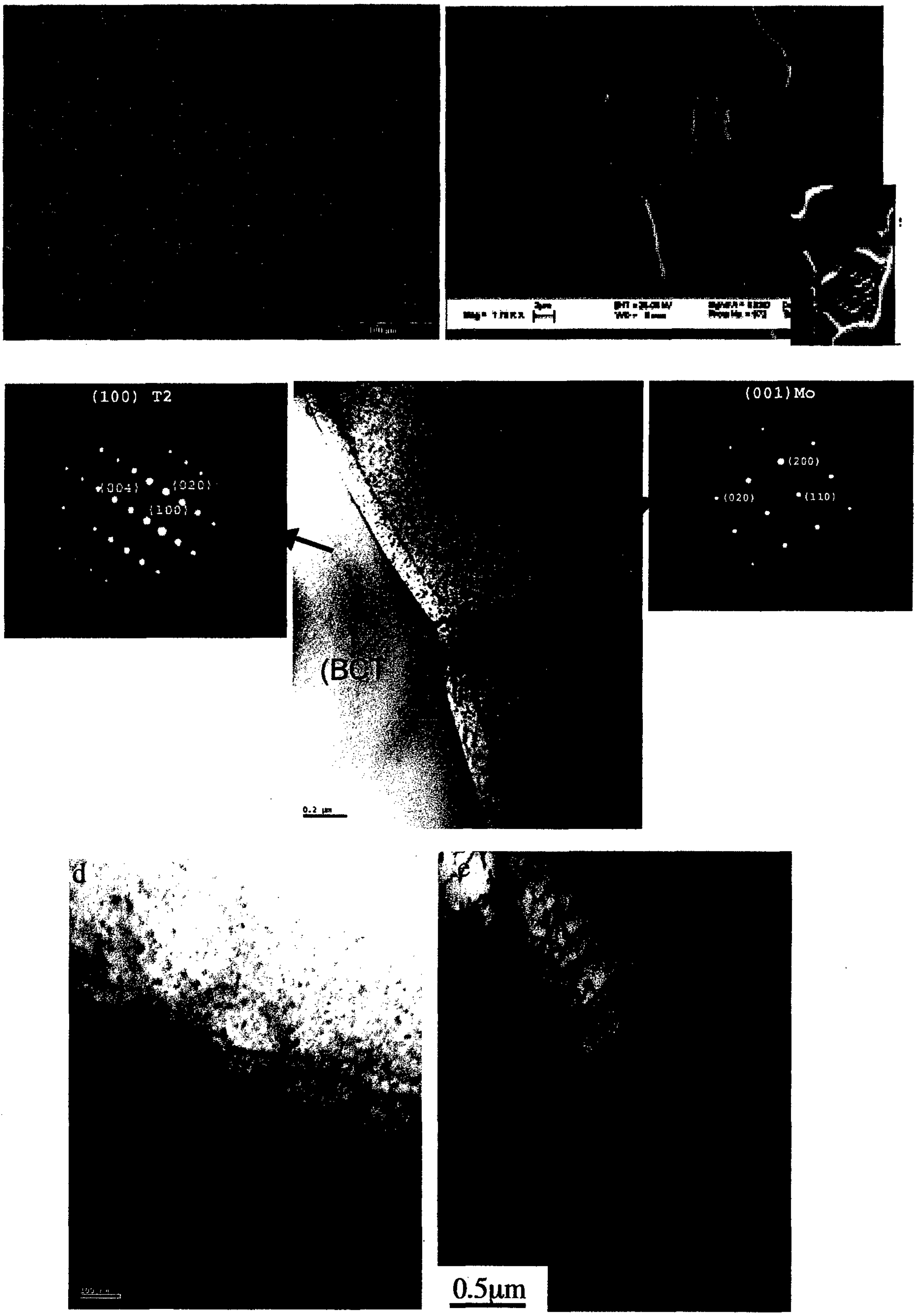
(100) T2
(004)
(020)
(100)
c
(BCT
0.2 µm
(001)Mo
(200)
(020)
(110)
d
e
0.5µm

Figure 7a-e: The HIPed and isothermally forged microstructure of the Mo-6.1Si-7.9B alloy showing a) a fairly uniform distribution of the T2 phase in a continuous Mo solid solution matrix with the occasional presence of clusters of interconnected T2 phase that are approximately spherical in shape and of a size corresponding to the starting powder size, b) the presence of silica in the form of alternating lamellae in some of the T2 particles, or at the T2/Mo solid solution interface (the inset in (b) shows fine precipitation within T2 adjacent to a silica lamella) possibly due to preferential Si depletion in T2) and c) a triple junction from two Mo grains and the T2 phase showing the grain boundaries as well as the interphase interface being clean. The Mo solid solution phase contains a moderately high dislocation density, the structure being made up of d) well developed networks and e) tangles.

emphasis was placed on understanding the compressive response at elevated temperatures and the effect of strain rate on compressive flow behavior. In these high-temperature compression tests that spanned the temperature regime 1000°C to 1400°C and a strain rate regime of 10^{-4} s^{-1} to 10^{-7} s^{-1}, the typical stress-strain response illustrated initial hardening that was followed by a significant decrease in the hardening rate to an almost zero hardening rate or occasionally even softening. As a consequence, flow stress at ~4% plastic strain (which is where a "quasi-steady-state" was reached in most instances) was used as the parameter for comparison of the materials' response to temperature and strain rate. Further, these compression tests were typically carried out to 5-7% strain, so that post-deformation microstructure described in the subsequent sections of this paper reflect this level of deformation.

The high-temperature compression response of the TZM alloy is presented in Figure 8a-d with the stress-strain behavior in compression at 1000°C, 1200°C and 1400°C shown in Figures 8a-c and the variation of the flow stress at 4% strain versus strain rate fitted to a power-law behavior in Figure 8d for the three temperatures. At 1000°C, the stress-strain curves show a perceptible level of work-hardening up to at least 6% strain (Figure 8a), and over a strain rate regime spanning 10^{-3} s^{-1} to 10^{-6} s^{-1}, the flow stress at 4% strain ranges from ~300 MPa to ~250 MPa and is only marginally dependent on strain rate (Figure 8d). In contrast, at 1400°C, at a nominal strain rate of 10^{-4} s^{-1}, a peak stress followed by work softening is observed with the peak stress occurring at ~135 MPa and ~2% strain; further, the flow stress is strongly strain-rate dependent, dropping to about 20 MPa at a strain rate of 10^{-7} s^{-1} (Figure 8c). A power law fit to the data at 1400°C yields a stress exponent of ~3.5 (Figure 8d). The behavior at 1200°C over this strain rate regime is intermediate between the behavior at 1000°C and 1400°C with some dependence of flow stress on strain rate, and the range of flow stress lying between ~230 MPa and ~130 MPa at the highest and lowest strain rates examined (Figures 8b,d).

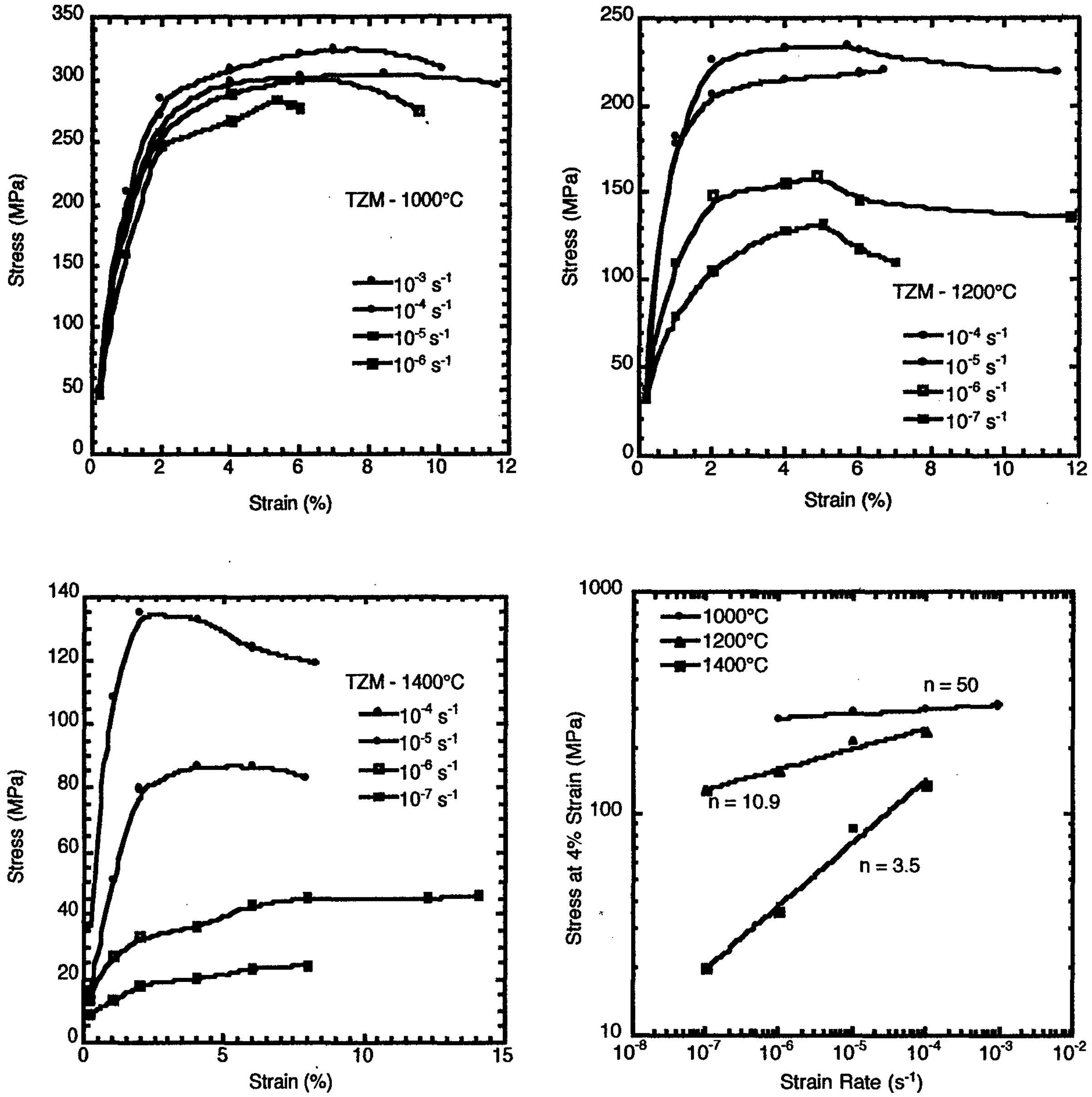

Figure 8: Compression stress-strain curves for TZM in the strain rate regime 10^{-3} s^{-1} to 10^{-7} s^{-1} at temperatures of a) 1000°C, b) 1200°C, and c) 1400°C; d) variation of the compressive flow stress at 4% strain as a function of strain rate at each of the three temperatures.

At 800°C, the compressive flow behavior of the Mo-Si-B alloy was only marginally affected by a change in the nominal strain rate from 10^{-4} s^{-1} to 10^{-7} s^{-1}. The flow stress at 4% strain remains very high (of the order of 1050-1100 MPa) and is comparable to the 0.2% offset yield stress at room temperature (Figure 9a). It is thus reasonable to assume that quasi-static strain rate (10^{-4} s^{-1} to 10^{-7} s^{-1}) has little effect on the material response between 25°C and 800°C. In contrast to the

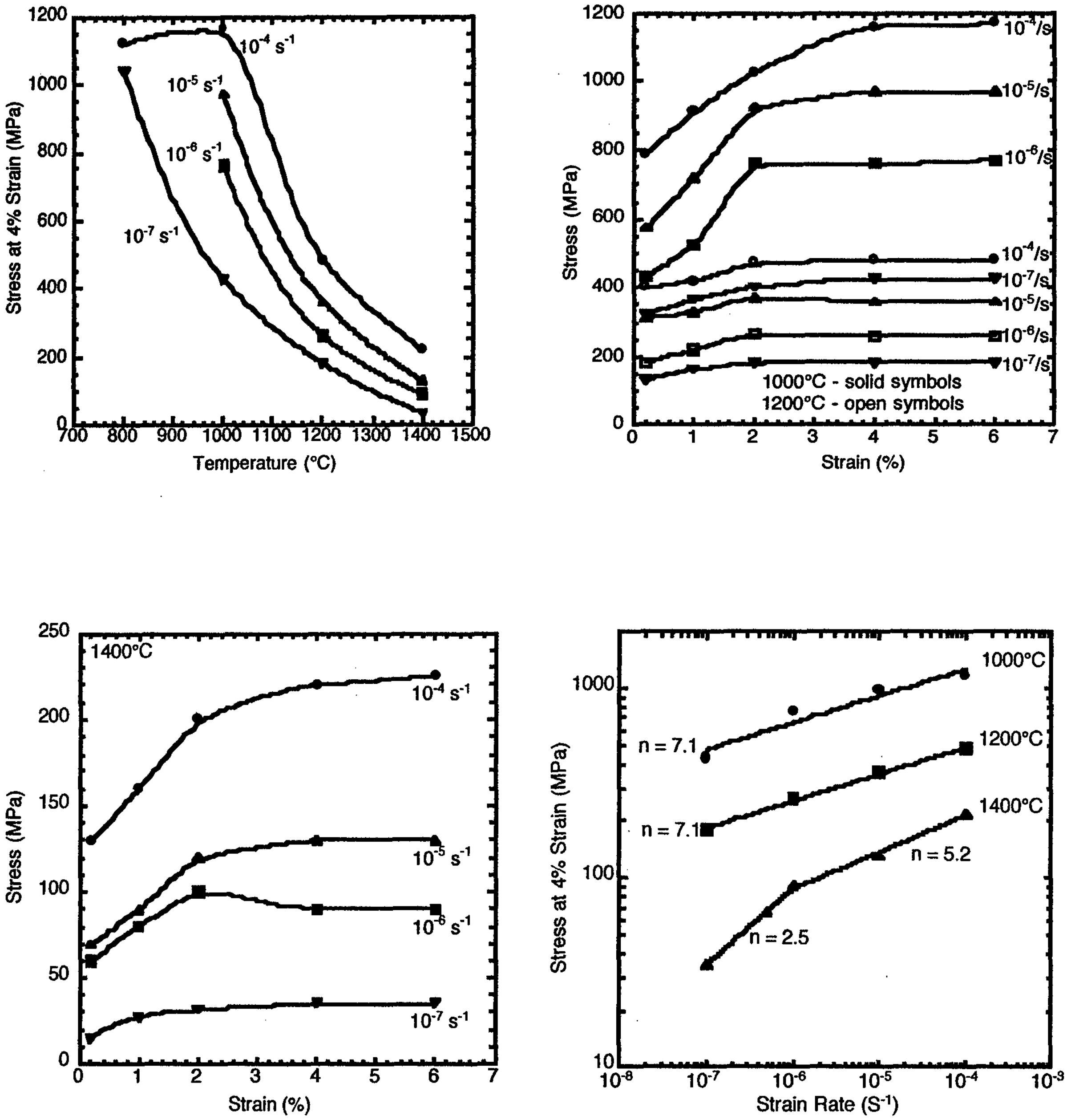

Figure 9: Compression response of the two-phase Mo-6.1Si-7.9B alloy in the 800°C-1400°C range in the strain rate regime 10^{-4} s^{-1} to 10^{-7} s^{-1}. In a), the variation in the compressive flow stress at 4% strain with test temperature at each strain rate is shown. In b) and c), the compression stress-strain curves at 1000°C, 1200°C and 1400°C are shown, and in d), the variation in compressive flow stress at 4% strain as a function of strain rate at each of these three temperatures is presented.

response observed at 800°C, the response in the 1000°C to 1400°C regime is strongly strain-rate dependent; thus, for example, at 1000°C, the flow stress drops from about 1100 MPa at the fastest strain rate to about 400 MPa at the slowest rate. An examination of compressive stress-strain data at 1000°C in Figure 9b confirms that this large decrease in flow stress is due to both, a lowering of the yield stress of the material at the slowest rate as well as a significant decrease in the hardening response during plastic deformation. The compressive stress-strain response as a function of strain rate in the regime 10^{-4} s^{-1} to 10^{-7} s^{-1} at 1200°C is also presented in Figure 9b and data obtained at 1400°C are provided in Figure 9c. A comparison of data in Figures 9b,c also illustrates that for a fixed strain rate, the 0.2% flow stress decreases with increasing temperature, as does the hardening rate in the plastic deformation regime (Note that the stress axis scale in Figure 9c is substantially different from that in Figure 9b). As before, the variation of the flow stress at 4% strain with strain rate at each of the three test temperatures could be fitted to a power-law and the results are shown in Figure 9d. At 1000°C and 1200°C, the fit yielded a stress exponent of ~7 for all four strain rates examined. At 1400°C, in the regime spanning strain rates of 10^{-4} s^{-1} to 10^{-6} s^{-1}, the exponent obtained was 5.2 whereas, between 10^{-6} s^{-1} and 10^{-7} s^{-1}, the strain rate dependence was significantly higher, yielding an exponent of 2.5, indicating a possible transition in the underlying deformation mechanism(s).

Compression tests were conducted at 1200°C and 1400°C on an isothermally forged, three-phase Mo-Si-B alloy (Mo solid solution phase + T2 + Mo_3Si) with a composition of Mo-8.6Si-8.7B (at.%). The microstructure of this alloy in the isothermally forged condition is shown in Figure 6a and the high areal fraction of intermetallic phases is evident. Back-scattered imaging in the SEM confirms the presence of two phases in addition to the still more-or-less continuous Mo solid solution matrix phase, exhibiting different atomic number contrast (Figure 10a). Based on X-ray diffraction analysis, these two phases were identified as Mo_3Si and T2 (Mo_5SiB_2). The variation of flow stress at 4% strain for the three-phase alloy at 1200°C and 1400°C as a function of strain rate is compared to that for the two-phase Mo-Si-B alloy and TZM in Figure 10b. In addition, the data at 1000°C comparing TZM with the two-phase MoSiB alloy are also included. It is evident that the flow stress of the three-phase alloy is virtually identical to that of the two-phase alloy at 1200°C and 1400°C for strain rates between 10^{-4} s^{-1} and 10^{-7} s^{-1}. This observation is suggestive of matrix-controlled deformation.

From the compression test data for the two-phase Mo-Si-B alloy at different temperatures and strain rates, and recalling that the flow stress at 4% strain corresponds to a steady-state stress, strain rates were plotted as a function of inverse temperature (Figure 11) for two narrow stress ranges (e.g. 130 MPa to 170 MPa and 425-460 MPa). The slope of the straight line fit to the data yields the activation energy (Q) for the deformation process and in the two instances, values obtained for Q were 415 and 445 kJ/mol which compare reasonably well with the activation energy for self-diffusion of Mo (400 kJ/mol – from ref. [43]). This finding is in agreement with the previous observation that deformation is matrix-controlled.

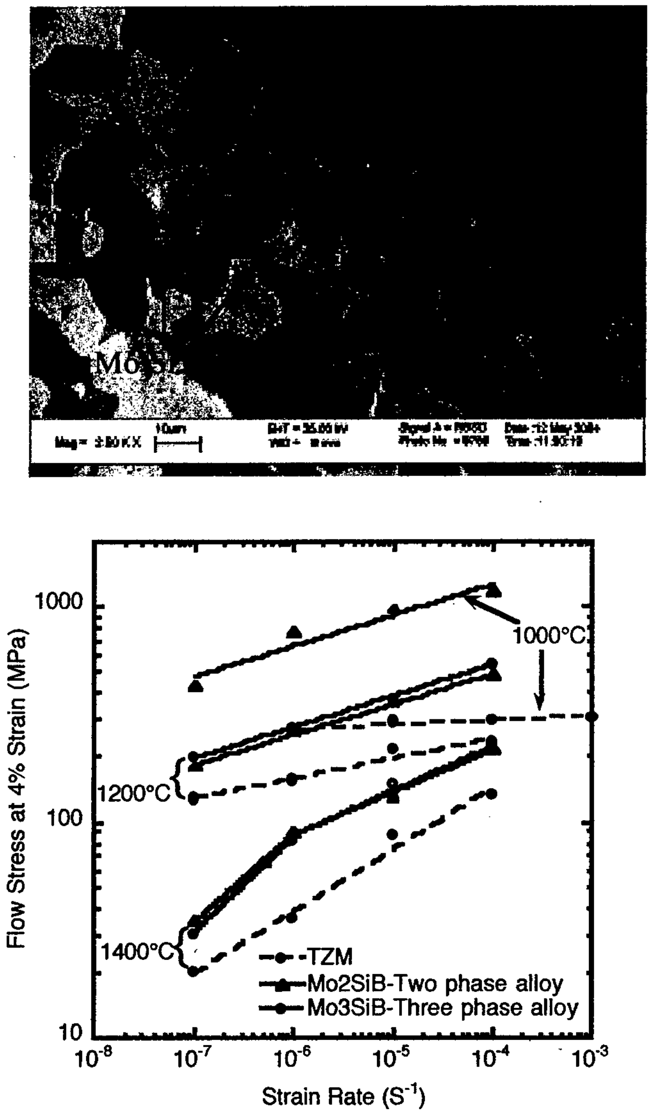

Figure 10: a) Back-scattered electron image of the three-phase Mo-8.6Si-8.7B alloy confirming the presence of the matrix solid solution phase and two types of precipitate phases that were verified by x-ray diffraction and compositional analyses to be the T2 phase and the Mo_3Si phase as labeled. In b) a comprehensive comparison is made of the variation of compressive flow stress at 4% strain for TZM, Mo-6.1Si-7.9B and Mo-8.6Si-8.7B with nominal strain rate in the strain rate regime 10^{-4} s^{-1} to 10^{-7} s^{-1} at test temperatures of 1000°C, 1200°C and 1400°C.

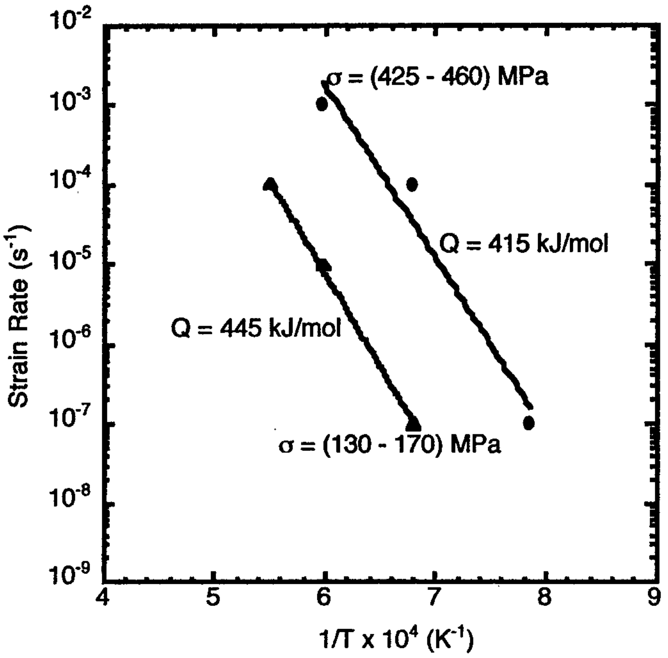

Figure 11: The variation in strain rate with reciprocal test temperature for stress levels of 130-170 MPa and 425-460 MPa. The activation energy for the deformation process can be obtained from the slopes of these curves.

4.3 Post-Deformation Microstructure

Examination of the deformed TZM specimens using an optical microscope revealed extensive recrystallization and grain growth in all cases, the degree being dependent on the test temperature and strain rate. Representative optical micrographs of specimens deformed at 1000°C at a strain rate of 10^{-6} s^{-1} and at 1400°C at a strain rate of 10^{-4} s^{-1} are shown in Figures 12a and 12b respectively. Examination of the deformed microstructure in the TEM confirms the conclusions drawn from metallography, and the recrystallized microstructure and the low dislocation density within the grains and subgrains are evident in micrographs obtained from the specimen deformed at 1000°C at a strain rate of 10^{-6} s^{-1} (Figures 12c,d).

Optical micrographs of the two-phase Mo-Si-B specimens deformed at 1000°C and 1400°C at nominal strain rates of 10^{-4} s^{-1} and 10^{-7} s^{-1} are shown in Figures 13a-d. These specimens were deformed to strains of 7%, 6.2%, 6.8% and 6% respectively. The T2 phase exhibits significant cracking at the fast strain rate at 1000°C (Figure 13a) whereas at the slowest rate, the extent of

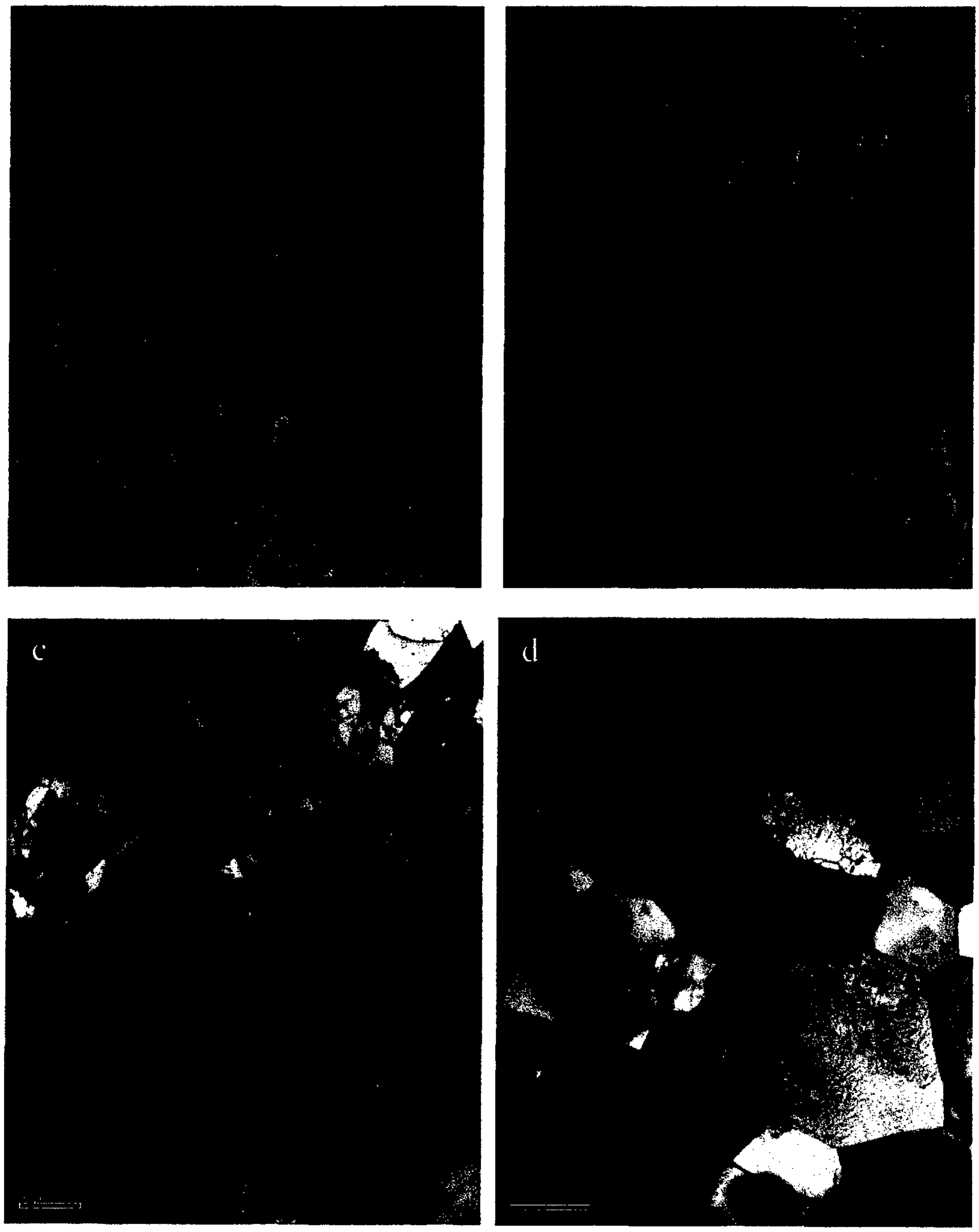

Figure 12: Optical micrographs of TZM specimens deformed at a) 1000°C at a strain rate of 10^{-6} s^{-1} and b) 1400°C and a strain rate of 10^{-4} s^{-1}, showing recrystallized microstructures with the grain size being larger in (b). In c) and d), TEM examination confirms the optical metallography findings in a) and b) of a recrystallized microstructure, and in additions reveals the low dislocation density within the grains and the presence of subgrains in the specimen confirming recrystallization is partial.

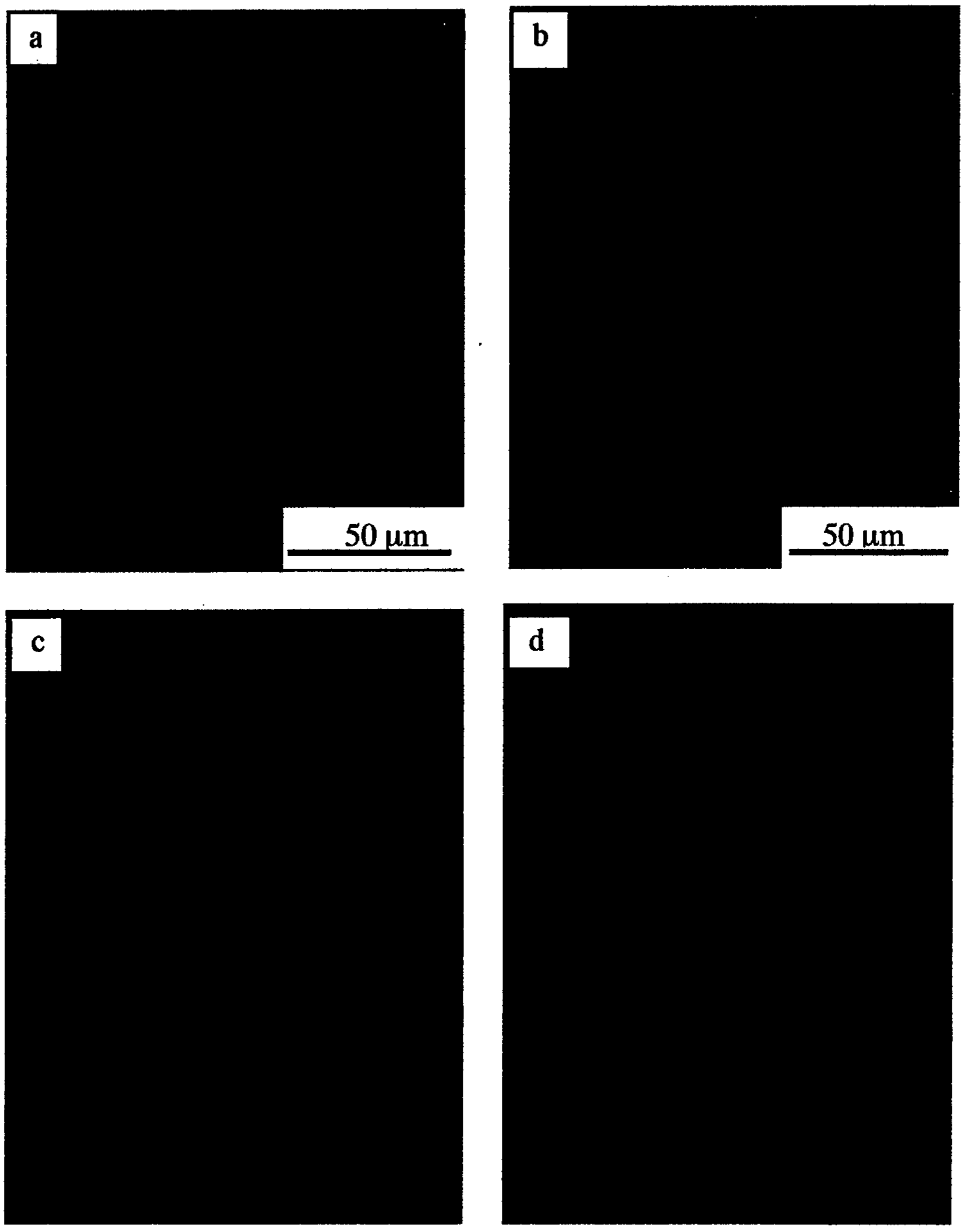

Figure 13: Optical micrographs of deformed two-phase Mo-6.1Si-7.9B specimens that show a) extensive cracking of the T2 particles in the specimen deformed at 1000°C at a strain rate of 10^{-4} s^{-1}, b) and c) minimal cracking of T2 particles in the specimens deformed at 1000°C at a strain rate of 10^{-7} s^{-1} and at 1400°C at a strain rate of 10^{-4} s^{-1}, and d) almost no cracking of T2 particles in the specimen deformed at 1400°C at a strain rate of 10^{-7} s^{-1}.

cracking is considerably less (Figure 13b). At 1400°C, almost no cracking is noted at the strain rate of 10^{-4} s^{-1} (Figure 13c) and none at all in the specimen deformed at 10^{-7} s^{-1} (Figure 13d).

Examination in the TEM of the specimen deformed at 1000°C at a strain rate of 10^{-4} s^{-1} confirms a high density of closely spaced dislocations in the Mo solid solution matrix (Figure 14a), whereas in the specimen deformed at 1000°C at the slowest rate (10^{-7} s^{-1}), the dislocations are arranged in networks, and sub-grains and sub-grain boundaries are evident (Figure 14b). (It is relevant to note that these observations of dislocation structures are not distinguishable from the dislocation structure in the forged condition; nevertheless, these compression specimens were plastically deformed to ~6% strain and the deformation must be accommodated by dislocation generation as well as rearrangement of the previously-existing and newly-generated dislocations). Furthermore, an examination of the T2 particles in the latter specimen shows the presence of dislocation debris (Figure 104) and slip (Figure 14d). Dislocations appear to be emitted at the particle/matrix interface (Figure14c). This was not observed in the as-forged material and leads to the conclusion that at 10^{-7} s^{-1} at 1000°C, the stress levels are adequate to initiate plastic deformation of the T2 phase but not high enough to cause premature fracture.

The microstructure after compressive deformation at 1400°C at strain rates of 10^{-4} s^{-1} and 10^{-7} s^{-1} was also examined in the TEM. Following deformation at the faster of the two strain rates, the microstructural features observed were similar to those seen in the specimen deformed at 1000°C at the slow rate of 10^{-7} s^{-1} (that is, the matrix exhibits recovery and the T2 phase shows evidence of plastic deformation). In the specimen deformed at the slow strain rate of 10^{-7} s^{-1}, the T2 particles do not appear dislocated, but the matrix clearly shows evidence of recovery.

4.4 Discussion of Microstructure and Strengthening Mechanisms

The as-received microstructure in the two-phase Mo-6Si-8B (in at.%) alloy consists of a dispersion of relatively coarse T2 particles in a more-or-less continuous Mo solid solution matrix. The individual T2 particles are blocky in shape with sizes ranging from 10-20 μm and the volume fraction of the T2 phase in the alloy is ~35-38 percent. Often, groups of T2 particles appear to be linked (Figure 3a) to form ligaments that lead to the creation of individual "islands" of matrix solid solution when observed in plane section. The T2 phase is known to exhibit plastic deformation only around 1550°C (at a strain rate of 10^{-3} s^{-1}). The Mo matrix dissolves small quantities of B and Si, and the two-phase microstructure is known to be resistant to coarsening or decomposition to very high temperatures (>1600°C). The distribution of B and Si within the Mo has not been characterized to date nor is their potency in contributing to solid solution hardening of the matrix

Figure 14: Deformed microstructures revealing dislocation arrangements: (a) high dislocation density with no clear indication of recovery or recrystallization in a specimen deformed at 1000°C using a strain rate of 10^{-4} s^{-1}; b) a recovered structure showing well-developed subgrain boundaries in a specimen deformed at 1000°C using a strain rate of 10^{-7} s^{-1}, with noticeable dislocation activity in the T2 phase (c,d). In (c), the dislocations in T2 appear to be emanating from the T2/matrix interface and in (d), several dislocations gliding along slip planes are seen within the T2 phase.

well understood. In addition to these features, the two-phase alloy examined in this study also contains silica as a second phase and the morphology observed (Figure 7b) suggests that it could be a eutectic/eutectoid decomposition product (alternately, it may be that the T2 particles crack during forging and the silica which is viscous at the forging temperature simply flowed in and filled the cracks). Its role in affecting the high temperature flow behavior is thought not to be substantial as it is co-mingled with the T2 phase and does not appear to provide a preferential crack path where present.

In the as-forged condition, it is seen (Figure 3e) that the matrix contains a moderately high dislocation density and this is likely to influence the early stage flow behavior of the material, perhaps more at 1000°C than at 1400°C. While B in Mo is quite likely an interstitial solid solution strengthener, Si is thought to be a substitutional element; the atomic radii of Mo and Si however differ substantially (0.14 nm for Mo and 0.117 nm for Si) and this is at least in part responsible for the low solubility of Si in Mo (2 at.% Si in Mo at 1600°C [44]). The large difference in atomic radius however will contribute in an appreciable way to substitutional solid solution hardening. Additionally, we also cannot discount the possibility that both B and Si are inhomogeneously distributed in the matrix (preferentially segregated at dislocation cores and grain boundaries) and may therefore be particularly effective in pinning mobile dislocations. It is pertinent to recall that the flow stress values reported in Figures 4-6 are all for 4% compressive strain, the intent there being to examine the steady–state stress levels. In discussing deformation mechanism(s) relating to early-stage flow behavior, it is therefore instructive to compare the yield stress of the materials under the various test conditions and these are provided in Table I.

An examination of Table I confirms that the 0.2% offset strength levels for the two Mo-Si-B alloys are similar for specific combinations of temperature and strain rate, and in all but one case, significantly superior to TZM. At the slowest strain rate (10^{-7} s^{-1}) at 1400°C, the strength values of the three alloys converge. To understand the origin of this high yield strength of the Mo-Si-B alloys relative to TZM, and more specifically the contribution from the Mo matrix solid solution, we conducted microhardness measurements on the Mo solid solution "islands" in these alloys and compared them to microhardness values for TZM as well as pure Mo (microhardness measurements were made using 500g load and reported values are Vickers Hardness Numbers, VHN). In TZM, the microstructural scale is adequately refined that microhardness measurements reflect the overall response of the alloy. Whereas the pure Mo exhibited a hardness of VHN 212 and the corresponding value for TZM was VHN of 256, the Mo solid solution matrix of the Mo-6Si-8B alloy (two-phase alloy) exhibited a substantially higher VHN of 474 in the as-forged condition that is likely a combined consequence of solid solution hardening and work-hardening arising from the high dislocation content in the as-forged condition.

Table I: Yield stress of TZM, Mo-6.1Si-7.9B (two-phase) and Mo-8.6Si-8.7B (three-phase) alloys.

Strain Rate	**Material**	**Temperature (°C)**		
	TZM	1000°C	1200°C	1400°C
$10^{-4}\ s^{-1}$		51.7 MPa	36.5 MPa	36.3 MPa
$10^{-5}\ s^{-1}$		50.0 MPa	32.3 MPa	16.5 MPa
$10^{-6}\ s^{-1}$		47.0 MPa	32.0 MPa	13.0 MPa
$10^{-7}\ s^{-1}$		----	32.0 MPa	9.0 MPa
	Mo-6.1Si-7.9B	1000°C	1200°C	1400°C
$10^{-4}\ s^{-1}$		790 MPa	400 MPa	130 MPa
$10^{-5}\ s^{-1}$		575 MPa	310 MPa	70 MPa
$10^{-6}\ s^{-1}$		430 MPa	180 MPa	60 MPa
$10^{-7}\ s^{-1}$		320 MPa	130 MPa	15 MPa
	Mo-8.6Si-8.7B	1000°C	1200°C	1400°C
$10^{-4}\ s^{-1}$			460 MPa	185 MPa
$10^{-5}\ s^{-1}$			295 MPa	117 MPa
$10^{-6}\ s^{-1}$			230 MPa	68 MPa
$10^{-7}\ s^{-1}$			109 MPa	15 MPa

An additional mechanism that can contribute to the strength and subsequent deformation response of the Mo-Si-B alloys is more macroscopic/geometric in nature and is often invoked in discontinuously reinforced composites [45, 46]. Christman et al [45] have shown the dependence of tensile properties (such as yield strength and work hardening behavior) of discontinuously reinforced metal-matrix composites on size, shape and spatial disposition of reinforcements; they concluded that significant triaxial stresses develop in the matrix due to constraints imposed by the reinforcements and these stresses provide an important contribution to strengthening. Whereas Christman et al [45] used a continuum plasticity approach, more recently, Cleveringa et al [46] have used the discrete dislocation approach to study the deformation behavior of a simple, two-dimensional, two-phase aggregate, where the matrix contains only a single slip system. Such a system was subjected to shear loading and the findings were compared against the results obtained using continuum plasticity. It was shown that when the reinforcement blocked all matrix slip planes, the composite exhibited high strain hardening whereas when a vein of unreinforced matrix material was present, a yield point was noted, followed by a decrease in flow stress until a steady state stress was reached. Both studies emphasize the importance of constraint imposed on the matrix by the particles on strengthening.

4.5 Analysis of the Deformation Behavior of the Two-Phase Aggregate

To explain the range of microstructural response observed following compression at high temperatures at different strain rates, it is necessary to understand how the stress and strain partition between the two phases. Thus, the compression response of the two-phase Mo-2Si-1B alloy was investigated via finite element modeling (FEM) with microstructure information being incorporated. Representative optical micrographs of the as-forged Mo-2Si-1B alloy were scanned to capture the size, shape, distribution and spacing characteristics of the T2 particles in the Mo solid solution matrix. Each scanned micrograph was then digitized and meshed into an FEM model. Both phases were assigned constitutive relations obtained from experimental observations at various temperatures and loading rates. As the mechanical properties of the Mo solid solution (containing Si and B) matrix is currently unknown, the properties of pure Mo was approximated in the simulation and these were obtained from the literature [47] for 300K and 1000K at a strain rate of 10^{-3} s^{-1}. The Mo solid solution phase was treated as elastic-plastic; at 300K, the yield strength was taken as 700 MPa with a linear work-hardening rate (expressed as $d\sigma_t/d\varepsilon_t$) of ~700 MPa, whereas at 1000K, the values for yield strength and work-hardening rate were 400 MPa and ~200 MPa respectively. The T2 phase was considered as being both elastic as well as elastic-plastic. Data for the plastic response of T2 were obtained from the work of Ito et al [25] where single crystals of the T2 phase were shown to deform plastically at 1550°C when deformed in compression in the [042] orientation. Thus, three distinctly different cases were evaluated that could be thought of as corresponding to temperature (and/or strain rate) effects: i) matrix strength and work hardening rate are high and particles are elastic, representing a relatively low-temperature situation, ii) matrix strength and work-hardening rate are lower, particle is still elastic – a situation that could correspond to an intermediate-temperature regime, and iii) matrix strength and work-hardening rate are low and particle exhibits plasticity, a siutation representing the high-temperature extreme. Since the matrix properties (for pure Mo) were not available at 1550°C, the data for 1000K were used for the case where T2 was assumed to show plasticity.

Commercially available FEM package (ABAQUS 6.3.1) was used to achieve uniaxial compression of 10% engineering strain with subsequent complete unloading. The friction between the material face and the compression block was assumed to be negligible, and thus sliding of the material block was allowed. At maximum compression, various contour plots of plastic equivalent strain and Mises stress were extracted to show the distribution and interaction between the two phases. In this paper, the FEM model is 2D with the bottom face vertically constrained and the top face uniaxially compressed. Three different mesh sizes were examined (120 x 120, 240 x 240, and 480 x 480) and it was determined that the 240 x 240 mesh adequately captured the situation.

The reference two-phase microstructure is shown in Figure 15a and equivalent plastic strain contours for three cases are shown in Figures 15b-d. In Figure 15b, which corresponds to deformation at low temperatures, it is seen that the applied displacement/strain is accommodated by strain in the matrix whereas the T2 particles remain mostly unstrained. This is a consequence of the assumption of elastic T2 particles and elastic-plastic matrix. The contours shown in Figure 15c correspond to an intermediate temperature deformation response where the matrix has a lower flow stress and a lower work-hardening rate and the particle still remain elastic. It is interesting to note that strain localization in the matrix is more intense than at room temperature and this is attributed to the decreased work-hardening response rather than the lower matrix flow stress. If however the T2 phase is allowed to deform plastically as would be representative of high temperatures and/or low strain rates, then deformation is much more homogeneous as evidence by the plastic equivalent strain contours in Figure 15d.

It is instructive to look at the companion Mises stress contours for these three cases and they are shown in Figures 16a-c. When the matrix is assumed to have the characteristics of Mo at 300 K (i.e. yield stress and work hardening rate at 300K) and the T2 phase is treated as elastic (Figure 16a), after 10 percent global plastic strain, the matrix is seen to support average stress levels of 1.0-1.4 GPa, although in local regions that are coincident with the high equivalent strain regions in Figure 16b, the matrix supports higher stresses of the order of ~2GPa. In contrast, the T2 phase supports extremely high stresses, with values reaching as high as 35 GPa. Clearly, these high values are observed because plastic deformation is not permitted and no fracture criterion or

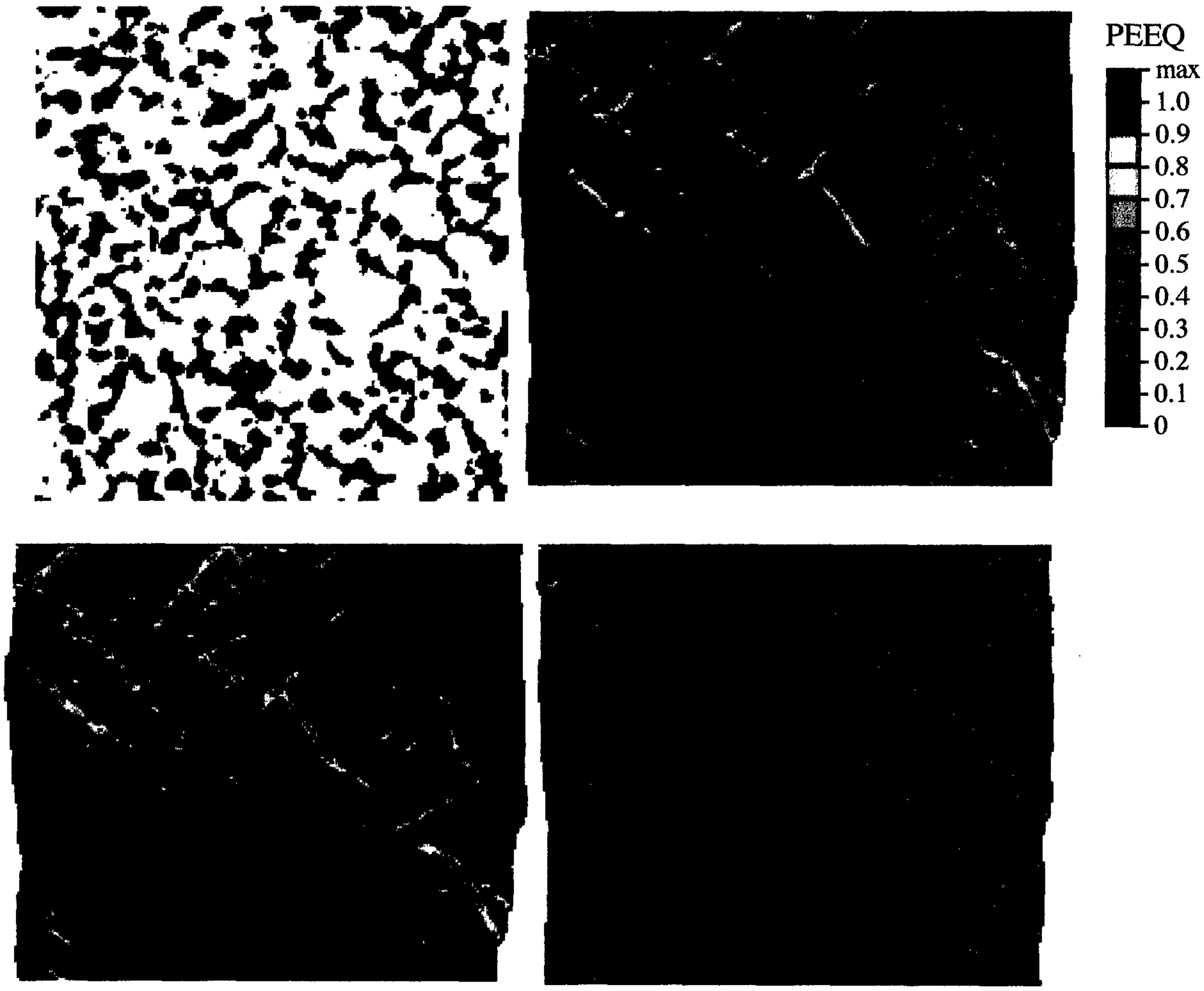

Figure 15: A scanned black-and-white reference microstructure in (a) is used for performing finite element analysis. In (b-d) equivalent strain contours are presented for a global strain of ten percent. In all three cases, the matrix is treated as pure Mo and in (b,c), the T2 phase is assumed to be elastic whereas in (d) it is treated as elastic-plastic. In (b), the properties (yield stress and work hardening behavior) of Mo are those at 300K whereas in (c) they are representative of 1000K, both sets of values taken from the literature [47].

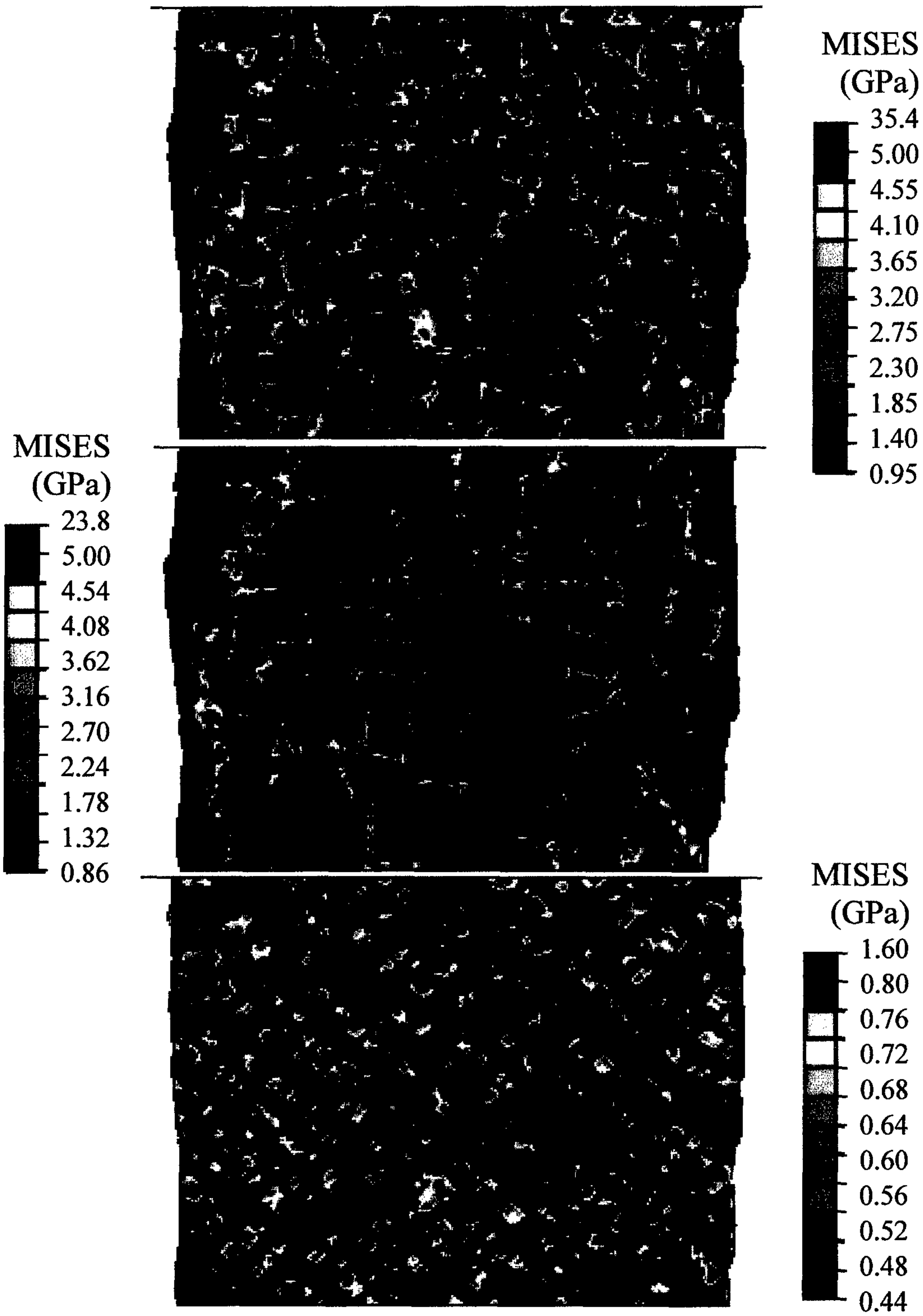

Figure 16: (a-c) The Mises stress corresponding to the three cases for which equivalent strains were presented in Figures 11b-d. Note that each figure (that is (a), (b) and (c)) has its own scale for stress levels so that the scale in (a) runs from 0.5 to 35.4 GPa, in (b) from 0.4 to 23.8 GPa and in (c) from 0.4 to 1.6 GPa.

cohesive surface is incorporated in the computation. When the matrix yield stress and work hardening rates are lowered (to values representing pure Mo at 1000 K) and T2 is maintained as being elastic, the stresses supported by the matrix phase and the T2 phase are lowered although T2 still supports large stresses in some locations. As previously stated, this condition may be viewed as being representative of an intermediate temperature or a lower strain rate, or both. A situation representing high temperature behavior and/or slow strain rate is depicted in Figure 16c where in addition to using the matrix properties at 1000 K, the T2 phase is treated as being elastic-plastic. This causes a significant decrease in the stress supported by the matrix but a more dramatic decrease is also observed in the stresses carried by the T2 phase.

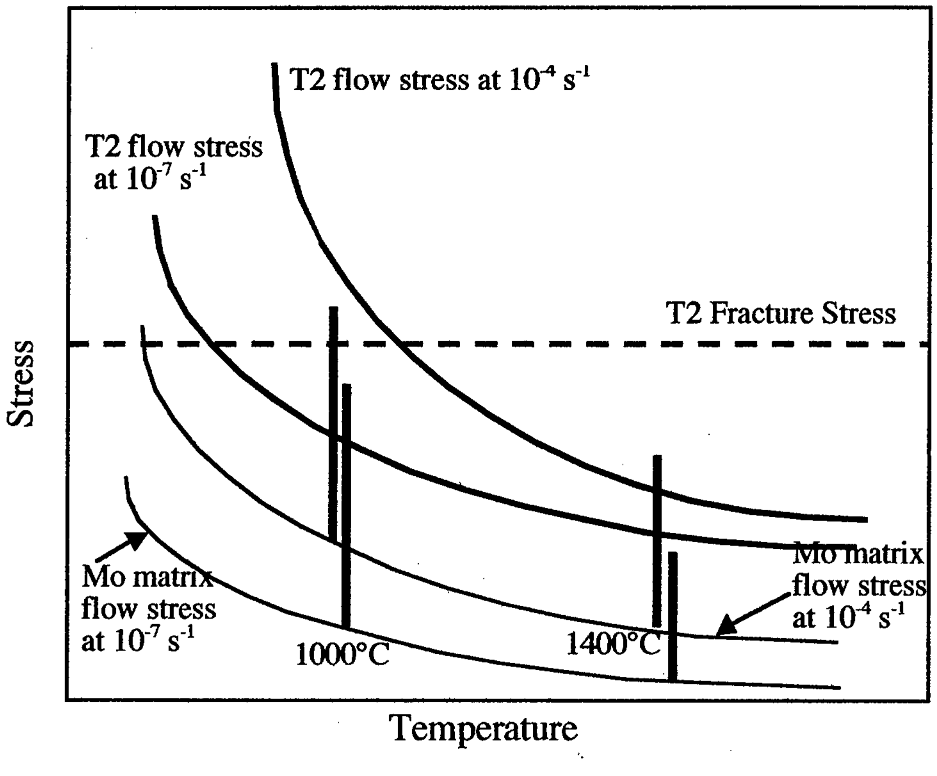

Figure 17: A schematic plot showing the variation of flow stress of the matrix solid solution phase and the T2 phase with temperature and strain rate, as well as the fracture stress of the T2 phase and how they can be used to explain the spectrum of deformed microstructures observed in Figures 13 and 14.

We explain the range of microstructures observed in the deformed specimens (T2 cracking, T2 plastic deformation and absence of dislocations or cracking in T2 particles depending on test temperature and strain rate) using the schematic illustration provided in Figure 17. The results from the computations support the rationale for this schematic illustration. The essence of the illustration is that the matrix phase and the T2 phase exhibit a temperature-dependent flow stress response that is sensitive to strain rate. The T2 phase is brittle at low temperatures and has a fracture stress that intersects the flow stress curves. When a compression test is performed at lower temperatures and faster rates (e.g. 1000°C and 10^{-4} s^{-1}) where the matrix flow stress is relatively high, stress multiplication occurs in the T2 phase and fracture precedes plastic flow of T2. In contrast, at the slower rate of 10^{-7} s^{-1} plastic flow of T2 is enabled. A similar argument is used to rationalize the response observed at 1400°C and 10^{-4} s^{-1} since the T2 flow stress is now lower than the fracture stress in a confined environment. At the slower rate of 10^{-7} s^{-1} at this temperature, the matrix flow stress is argued to be low enough that in spite of stress multiplication in the T2 phase, it is still below the flow stress (and fracture stress) at this temperature and so the T2 only deforms elastically and thus does not exhibit cracks or dislocation debris.

5.0 FRACTURE TOUGHNESS AND FATIGUE BEHAVIOR

5.1 Isothermal Oxidation Response

The weight changes resulting from isothermal oxidation for 24 hours at different temperatures are shown in Figure 18. The weight gain exhibited by MT104 and Mo-6Si-8B at 300°C is of the order of 0.001% of the initial weight of the samples and at 600°C, Mo-6Si-8B and MT104 show a weight gain of 0.9% and 27% respectively. Based on these results it was concluded that for temperatures of 600°C and higher, monotonic and cyclic crack growth tests had to be conducted in vacuum. Mo-6Si-8B showed increasing weight loss following the prescribed thermal exposure in the range of 900°C –1200°C, the weight loss percentage being 22% at 1200°C. The mass gain in the lower temperature regime (300-600°C) is attributed to MoO_3 and borosilicate formation while the weight loss at higher temperatures is thought to be a consequence of MoO_3 volatilization [48].

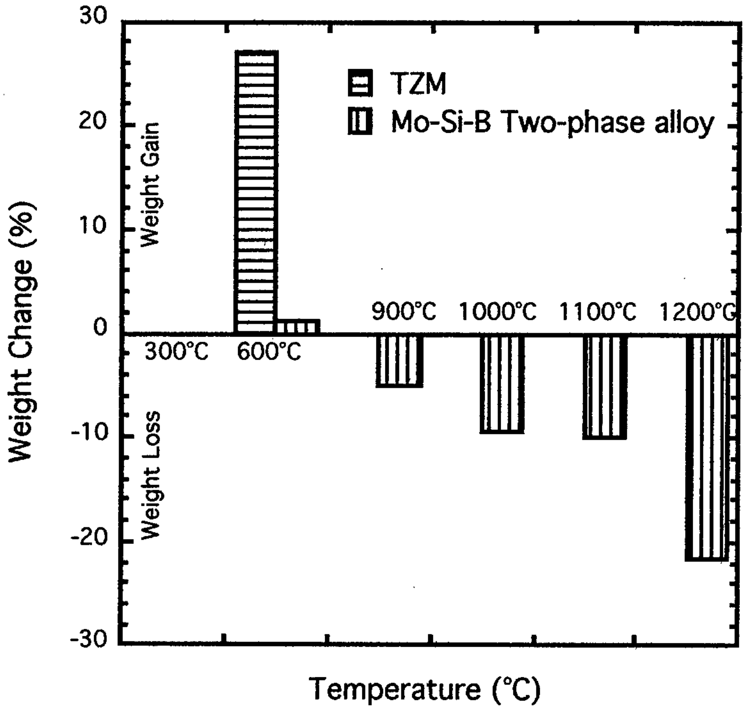

Figure 18: Isothermal oxidation response of TZM and the two-phase Mo-Si-B alloy as a function of temperature in the temperature interval 300°C-1200°C. In all instances, the samples were held at temperature for 24 hours.

5.2 Fracture Toughness and Monotonic Crack Growth Response

The variation in fracture toughness with temperature is shown in Figure 19. The room temperature toughness of the as-forged, two-phase Mo-Si-B alloy is about 8 MPa√m and increases marginally to ~ 9 MPa√m following extended annealing of the as-forged material (1600°C/48h). With increasing temperature, the toughness increases gradually to 13 MPa√m at 600°C for tests conducted in air and in vacuum. Tests at higher temperatures were conducted only in vacuum as preliminary isothermal oxidation studies at higher temperatures (600°C, 900°C and 1200°C for 24 hours) revealed that significant material loss occurs. In this context, it is worth noting that the monotonically loaded bend tests take only take fifteen to twenty minutes at the test temperature to go to completion as opposed to fatigue crack growth tests discussed in the later sections of this paper. The steepest rise in toughness is noted in the 1200°C-1400°C regime, where it increases from ~18 MPa√m to about 25 MPa√m.

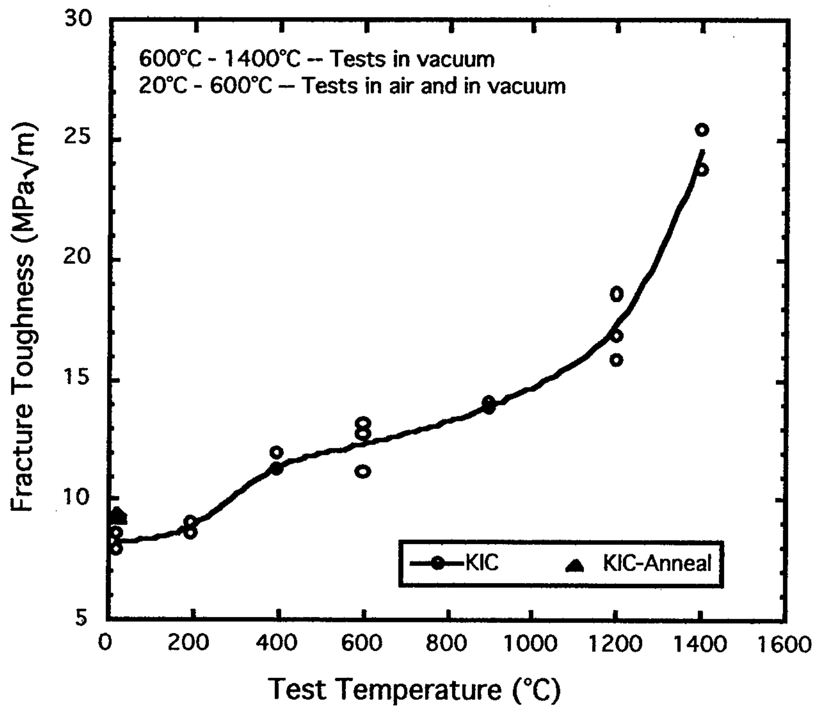

Figure 19: The variation in fracture toughness with test temperature measured in air (20°C-600°C) and in vacuum (20°C-1400°C) for the two-phase Mo-Si-B alloy. Except for one set of tests at room temperature that was conducted on annealed material, all other tests were conducted on as-forged material.

Examination of the interaction of a growing crack with the microstructure on the surface of the bend specimen by periodically interrupting the crack growth experiment enables an understanding of preferred crack path in the two-phase alloy. A representative image is shown in Figure 20a for a test conducted at room temperature. In addition to the main crack in the matrix solid solution, hairline secondary cracks are also observed; further, the main crack appears to show some preference for propagating along the T2/matrix interface versus going through the T2 particles, although in several instances, the latter was also seen. Fracture surface examination after the completion of the test (Figure 20b) supports the notion of substantially intergranular failure, although there was occasional evidence for transgranular rupture within the Mo solid solution.

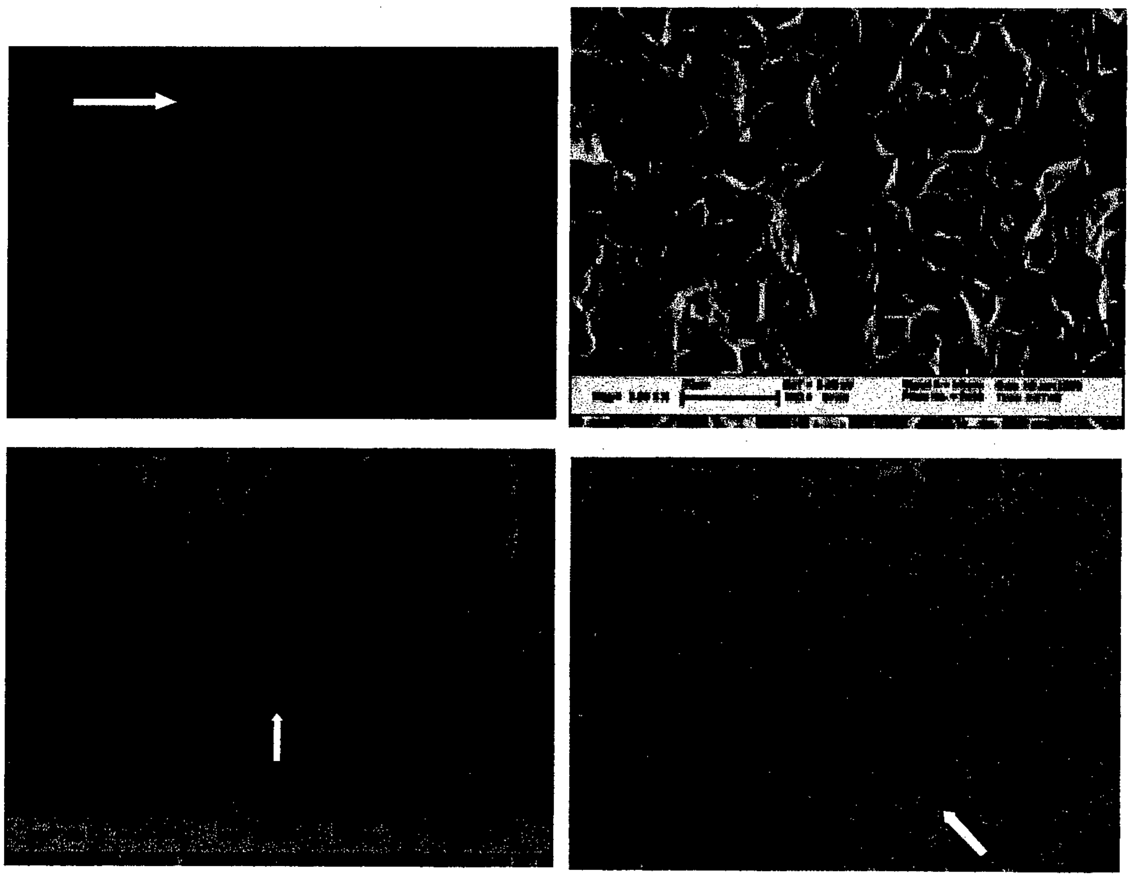

Figure 20: (a) Optical micrograph shows crack interaction with the surface microstructure obtained by interrupting monotonic loading of a notched and fatigue precracked bend specimen; The resulting fracture surface (b) after completing the test reveals a predominatly intergranular failure mode. Following a similar test at 1400°C in vacuum, the fracture surface (c) reveals a mix of transgranular cleavage and intergranular failure modes. An examination of the interaction of the advancing crack with the microstructure using an interrupted test at 1400°C (d) reveals extensive crack branching and multiple micorcracks ahead of the main crack. White arrows in (a) and (d) illustrate the direction of crack growth.

Chemical analysis of some of the flat featureless facets on the fracture surface using Energy Dispersive X-ray (EDX) methods confirmed Si levels significantly higher than those permitted in the solid solution, leading to the conclusion that these were fractured T2 particles. With an increase in test temperature, the incidences of transgranular cleavage appeared to increase at the expense of intergranular failure, although even at 1400°C, intergranular failure was still noted (Figure 20c). A careful examination of Figure 20c shows the rather interesting feature of cleavage of a large grain with intergranular failure of a smaller one located in the center of the cleaved grain (indicated by an arrow). This suggests that the small grain is likely a consequence of recrystallization, and that recrystallized grain boundaries are preferred crack paths (further note the secondary cracks around the cleavage facets that are believe to be intergranular cracks around the cleaved grains). The scale of the structure in the intergranular fracture regions in Figure 20c is similar to the corresponding features in the room temperature test specimen (Figure 20b) suggesting marginal grain growth (if any) at 1400°C for the duration of the test. It is not possible however to preclude the fact that some recrystallization of the forged material did occur during the elevated temperature test. An examination of the crack interaction with the surface microstructure at 1200°C and 1400°C revealed an extensive zone of microcracks ahead of the main crack (Figure 20d). This is in contrast to a single crack that propagates in the matrix at room temperature (Figure 20a). The main crack at 1400°C is significantly more tortuous than the one at room temperature, while the microcracks are often jagged on a scale comparable to the grain size.

It is worth noting that in the 20°C-600°C regime, where tests were conducted in air and in vacuum, the fracture surfaces did not exhibit significant differences (Figures 21a,b) except for the fact that those specimens tested in air exhibited oxidized fracture surfaces (a feature that was inevitable as these fresh surfaces were exposed to air during the cooling cycle); interestingly, fracture surface oxidation was readily noted on the Mo solid solution facets but not on the T2 cleavage facets, making it more easy to visually discriminate the T2 particles on the fracture surface (Figure 21b-400°C – air) and implying the enhanced warm-temperature oxidation resistance of this intermetallic phase relative to the matrix solid solution.

5.3 Cyclic Loading Response--Stress-Cycles (S-N) to Failure

The S-N response of the TZM plate material and the Mo-Si-B alloy was assessed at room temperature and that for the Mo-Si-B at 1200°C. These results are shown in Figure 22a. At 20°C, TZM shows a shallow fatigue response, characteristic of brittle materials, with a failure stress of ~370 MPa following 30,000 cycles that decreases to ~320 MPa following 10^6 cycles. This stress level appears to be just above a threshold stress, as a specimen cycled at a maximum stress of 310 MPa ($R = 0.1$), did not fail after 10^7 cycles. It is worth noting that the S-N response that we report

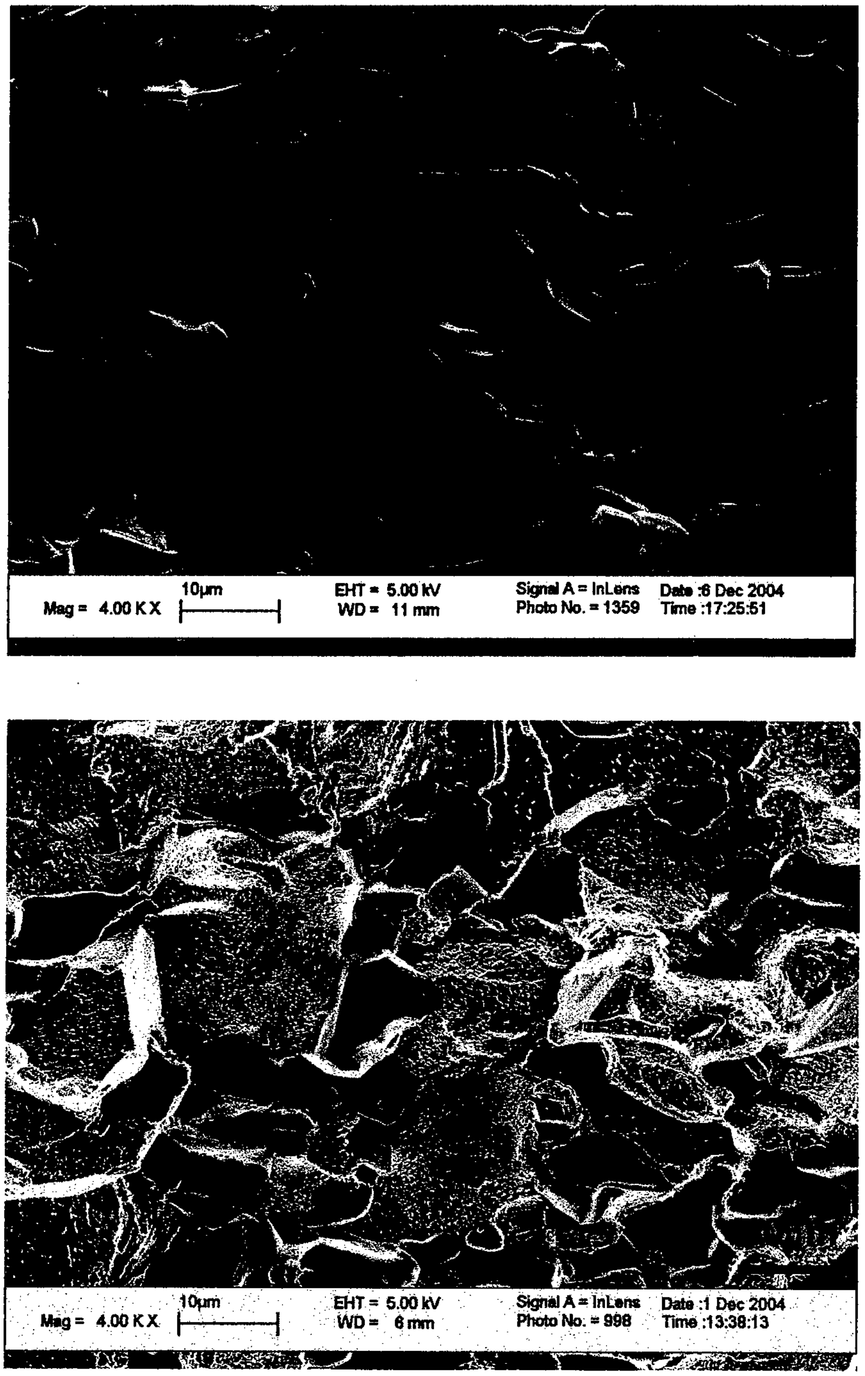
10μm
Mag = 4.00 K X
EHT = 5.00 kV
WD = 11 mm
Signal A = InLens
Photo No. = 1359
Date :6 Dec 2004
Time :17:25:51
10μm
Mag = 4.00 K X
EHT = 5.00 kV
WD = 6 mm
Signal A = InLens
Photo No. = 998
Date :1 Dec 2004
Time :13:38:13

Figure 21: Fracture surfaces resuting from the fracture toughness tests at 400°C conducted (a) in vacuum, and (b) in air.

here for powder-metallurgy processed TZM is inferior to an earlier report by Calderon et al [16] where the endurance limit was shown to be around 500 MPa. This difference is thought to be a consequence of the non-optimal microstructure of the off-the-shelf TZM that was utilized in the present study. Specifically, examination of fracture surfaces from these specimens revealed that the coarse zirconia particles present in this material acted as the fatigue crack initiation site (rather than surface machining marks etc; often a single site was observed from where the crack radiated out, but occasionally two or more similar sites were also observed on the fracture surface) and subsequent fracture occurred through a mix of transgranular cleavage and intergranular failure; the size and shape of the intergranular facets strongly suggested that this mechanism dominated in regions where recrystallization had occurred. The S-N response of the Mo-Si-B alloy is similar to the TZM, and in fact the slope is shallower, but the absolute stress levels are considerably higher (565-500 MPa). A single initiation site was not evident and fracture appears to have propagated through a mix of intergranular and transgranular cleavage modes (Figure 22b). In regions where intergranular fracture is observed, the grain boundary facets are of the order of 10 μm or less and equiaxed, suggestive of partial recrystallization. These observations are consistent with those made for the monotonically loaded bend specimens.

At 1200°C, the S-N response of the Mo-Si-B alloys is superior to that at room temperature, with a threshold stress (defined by survival of the specimen after 10^7 cycles) of ~550 MPa. The material is more prone to fatigue failure at this temperature as evidenced by the steeper slope of the S-N curve relative to room temperature. This would be expected since the material is capable of plastic deformation at this temperature. S-N tests were not conducted on the TZM alloy at 1200°C in this study. Although S-N data for TZM are not available at 1200°C in the published literature, a value of about 250 MPa for failure stress following 10^7 cycles was reported for TZM at 850°C [47]. Fracture surface examination of the Mo-Si-B specimens tested at 1200°C (Figures 22c,d) revealed a mix of intergranular failure and transgranular cleavage for the specimens that failed after 10^4 and 10^6 cycles; the grains delineated by the grain boundary facets however do not appear as equiaxed as they do following the room-temperature test (Compare Figures 22c and 22d with Figure 22b), suggestive of some plastic deformation prior to grain boundary separation at the higher test temperature of 1200°C relative to room temperature.

5.4 Cyclic Loading Response -- Crack Growth Studies

In the temperature interval from 20°C-600°C, cyclic crack growth tests (da/dN versus ΔK) were conducted in air and in vacuum; higher temperature tests were only conducted in vacuum. We first present the results of the tests at room temperature, followed by the results of the 300°C and

600°C tests in air and in vacuum, and then finally the results for the 600°C-1400°C tests conducted in vacuum. These tests were performed on TZM and the Mo-Si-B alloy.

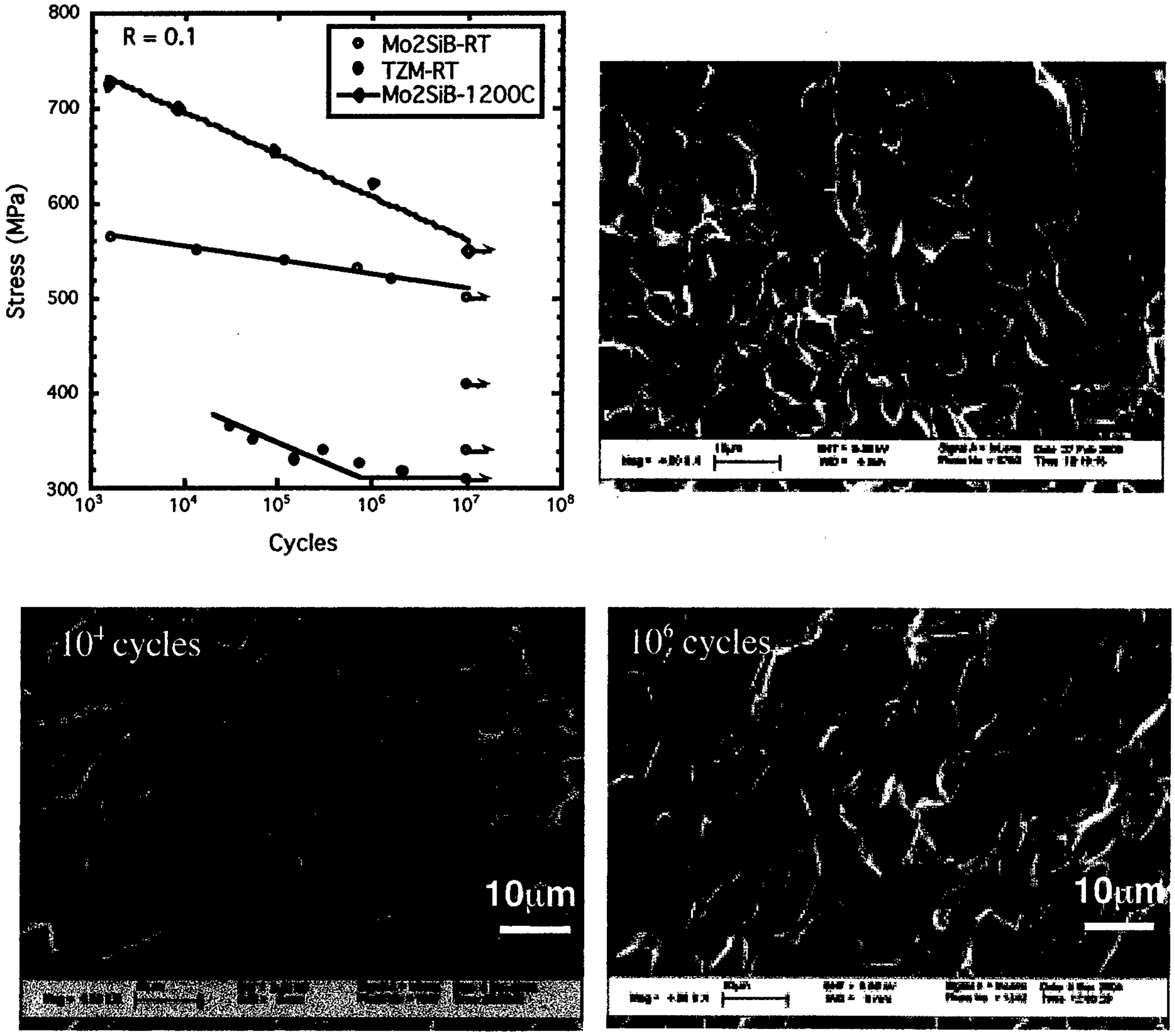

Figure 22: (a) The S-N response of the two-phase Mo-Si-B alloy at 20°C in air and at 1200°C in vacuum using R= 0.1. For purposes of comparison, S-N response of TZM was obtained at room temperature in air. In (b), the fracture surface following 2 million cycles at room temperature for the Mo-Si-B alloy is shown. In (c) and (d), the fracture surfaces following 10,000 cycles and a million cycles at 1200°C respectively are shown.

The da/dN - ΔK response for TZM at R=0.1 and R=0.2 is presented in Figure 23a. The tests were conducted in two orientations – crack propagation in the rolling direction and crack propagation transverse to it. It appeared that the response of the specimens with crack running in the transverse direction was marginally better than when the crack was oriented in the rolling direction and therefore all subsequent tests on TZM were performed with the notch aligned in the transverse orientation. Furthermore, the response for R=0.1 and R=0.2 was not appreciably different and therefore subsequent tests were limited to R=0.1. The threshold ΔK for the specimen notch oriented in the rolling direction is ~3 MPa√m whereas for the specimen with the notch oriented in the transverse orientation, it is between 4.5-5.0 MPa√m. In all instances however, the Paris slope is steep (n = 21) and is characteristic of a brittle material. The results for the Mo-Si-B alloy at R=0.1 and R=0.2 in air at room temperature are provided in Figure 23b. Once again there appears to be no visible difference in behavior and all subsequent tests were conducted at R=0.1. Since specimens were extracted from an isothermally forged pancake, geometric constraints precluded samples from being machined in orientations that would align the notch in the forging direction (pancake thickness direction). A cursory examination of Figure 23b reveals a threshold ΔK of a little over 5MPa√m and a steep Paris slope (n=17); the behavior is remarkably similar to TZM.

The interaction of a growing fatigue crack with the surface microstructure was examined by loading a pre-cracked specimen for a fixed number of cycles at a specific ΔK (50,000 cycles; 5 MPa√m), marginally above the threshold value and then unloading it. The results are compared in Figures 23c and 23d that show the fatigue pre-crack and the subsequent crack growth due to the cyclic loading. The rolling direction in these images is the vertical direction as evidenced by the orientation of the elongated grains. It is clear that the fatigue crack advances preferentially along the transverse grain boundaries. A similar analysis is presented for the Mo-Si-B alloy in the pair of images in Figures 23e and 23f. In Figure 23e, a region of the specimen is shown ahead of the main crack. The specimen at this stage had been subjected to 25,000 cycles at ΔK = 5.4 MPa√m and unloaded for examination. Two locations in the micrograph, 'X' and 'Y' provide reference markers. The specimen was then subjected to another 25,000 cycles at a slightly higher ΔK = 5.7 MPa√m and the region shown in Figure 23e is reproduced in Figure 23f with the two markers 'X' and 'Y'. In addition, at the extreme right of the figure, a vertical white arrow denotes the location of the main crack. It appears that the main crack bifurcates with one branch moving just above 'Y' and the other just above 'X' through a T2 particle. Multiple cracking and crack branching occurs within the matrix as the material is cycled, and damage in the form of hairline cracks is evidenced in the matrix as far as ~100 μm ahead of the location marked 'X'. The crack path shows no preference for any specific microstructural feature(s).

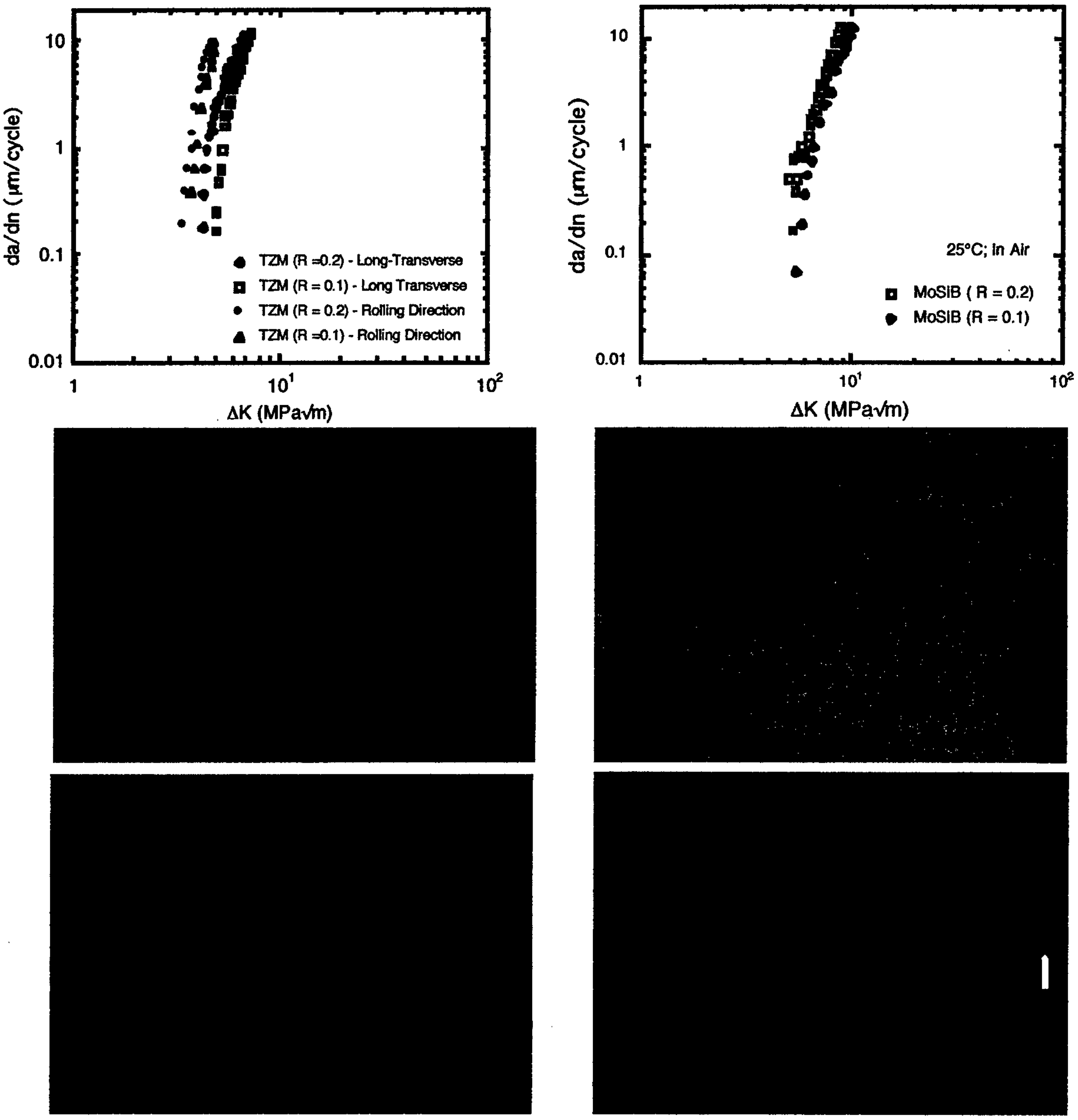

Figure 23: Cyclic crack growth behavior at room temperature for (a) TZM with crack growth in the longitudinal and long transverse directions for R=0.1 and R=0.2, and (b) for the two-phase Mo-Si-B alloy for R = 0.1 and 0.2. In (c), a micrograph of a TZM specimen shows the notch and the fatigue precrack; in (d) the same region following 25,000 cycles at a ΔK = 5 MPa√m confirms cyclic crack growth along transverse grain boundaries. In (e), the region ahead of a growing crack in the Mo-Si-B alloy following 25000 cycles at a ΔK of 5.4 MPa√m is shown and again in (f) after an additional 25,000 cycles at an increased ΔK of 5.7 MPa√m. Matrix and particle cracks are noted in the vicinity of regions marked X and Y and the main crack is illustrated with the white arrow in the extreme right of figure (d).

The effects of temperature (up to 600°C) and environment (air versus vacuum) on cyclic crack growth behavior of TZM and the Mo-Si-B alloy are seen in Figures 24a and 24b respectively. For TZM (Figure 24a), testing in air at 300°C, lowers the threshold ΔK from ~5 MPa√m to ~3.2 MPa√m and increases the Paris slope (n) from 20 at room temperature to 30. The results of the test at 600°C in air were worse with only a few data points being obtained before the crack propagated catastrophically. The threshold ΔK dropped to <3 MPa√m; a Paris slope could not be obtained due to insufficient data. However, when the 600°C test was conducted in vacuum, the response in terms of the threshold stress and the Paris slope (4.7 MPa√m and n = 18) was similar to that of the room-temperature-tested specimen. Taken together, the results in Figure 24a confirm a significant adverse influence of environment on the cyclic crack growth response of TZM in the 20°C-600°C regime.

The results for the Mo-Si-B alloy (Figure 24b) in this temperature regime also show a dependence of cyclic crack growth response on environment although not as dramatic as TZM. Thus, the Paris slope increases from 17 at room temperature to 19 at 300°C in air, to 23 at 600°C in air. When the test is conducted at 600°C in vacuum, the Paris slope returns to the value at room temperature of 17. Furthermore, it is evident from Figure 24b, that the threshold ΔK does not change appreciably (~4.6 MPa√m to ~5.4 MPa√m) with either the environment or the test temperature within the 20°C-600°C range.

Tests at higher temperatures were conducted in vacuum only for both materials. Whereas the Mo-Si-B alloy was tested at 900°C, 1200°C and 1400°C, TZM was only tested at 900°C and 1200°C. The results of these high-temperature tests together with the results for the room-temperature test and the 600°C test in vacuum are presented in Figures 25a,b. In presenting the room temperature test in air along with the vacuum test results at elevated temperatures, it is assumed that environmental effect, if any is present, is negligible at room temperature. In the case of TZM, up to and inclusive of 900°C, the cyclic crack growth curves virtually overlap (Figure 25a), with the Paris slope at 900°C being marginally lower than at 600°C (n = 14 versus n = 18). At 1200°C however, there is a measurable improvement in the crack growth behavior with the threshold ΔK of ~5 MPa√m and a Paris slope n ~ 8. In the case of the Mo-Si-B alloy (Figure 25b), a similar response is noted in that the behavior from room temperature to 900°C may be grouped where a marginal increase in Paris slope occurs (from n = 17 at room temperature to n = 11 at 900°C), with the threshold ΔK remaining around 5 MPa√m. At 1200°C, the Paris slope drops to ~6 and then to 3.5 at 1400°C; the threshold ΔK continues to remain between 5 and 6 MPa√m. Thus, at or above 900°C, for a given temperature, the cyclic crack growth response of the two-phase Mo-Si-B alloy appears to better than that of the TZM alloy evaluated in this study; this may also be seen from the

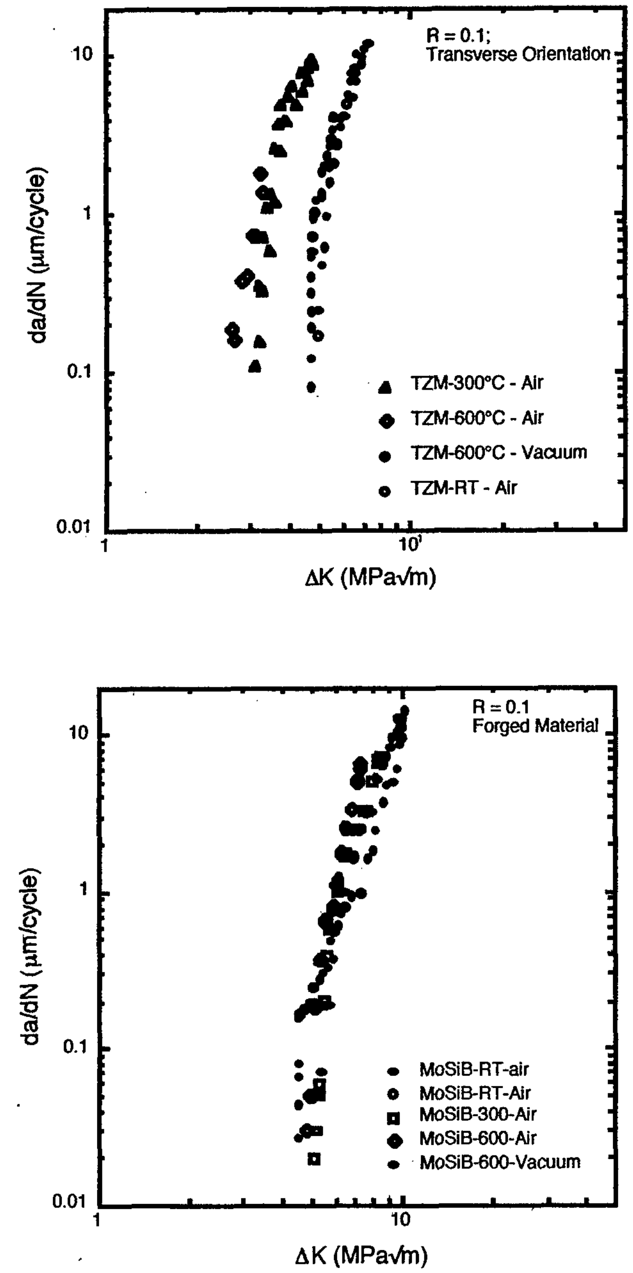

Figure 24: Cyclic crack growth behavior (R = 0.1; 5Hz) in air from room temperature to 600°C, and in vacuum at 600°C for (a) TZM, and (b) the two-phase Mo-Si-B alloy.

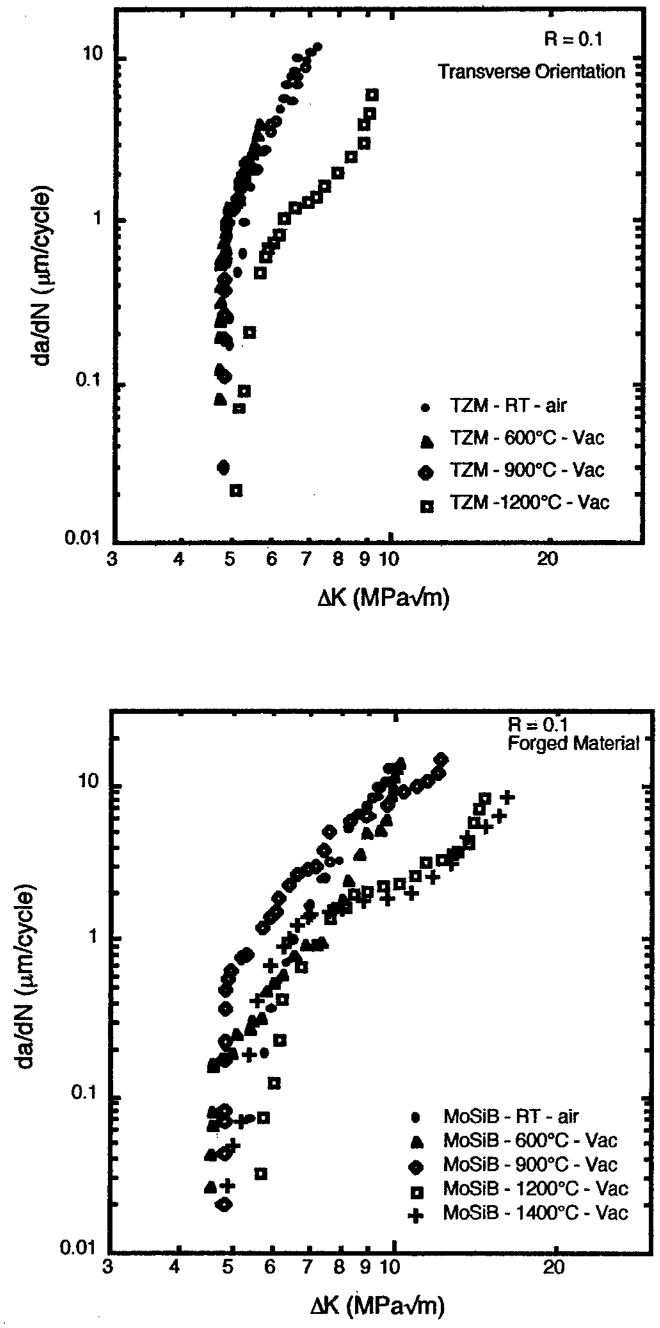

Figure 25: Cyclic crack growth behavior (R = 0.1; 5Hz) in air at room temperature, and in vacuum (a) from 600°C to 1200°C for TZM, and (b) from 600°C to 1400°C for the two-phase Mo-Si-B alloy.

variation of the Paris slope with temperature for the two materials in Figure 26. Note that in this figure, data for Mo-Si-B obtained at 1100°C and 1300°C are included. Cyclic crack growth tests at these two temperatures were only performed for ΔK values lying in the Paris regime.

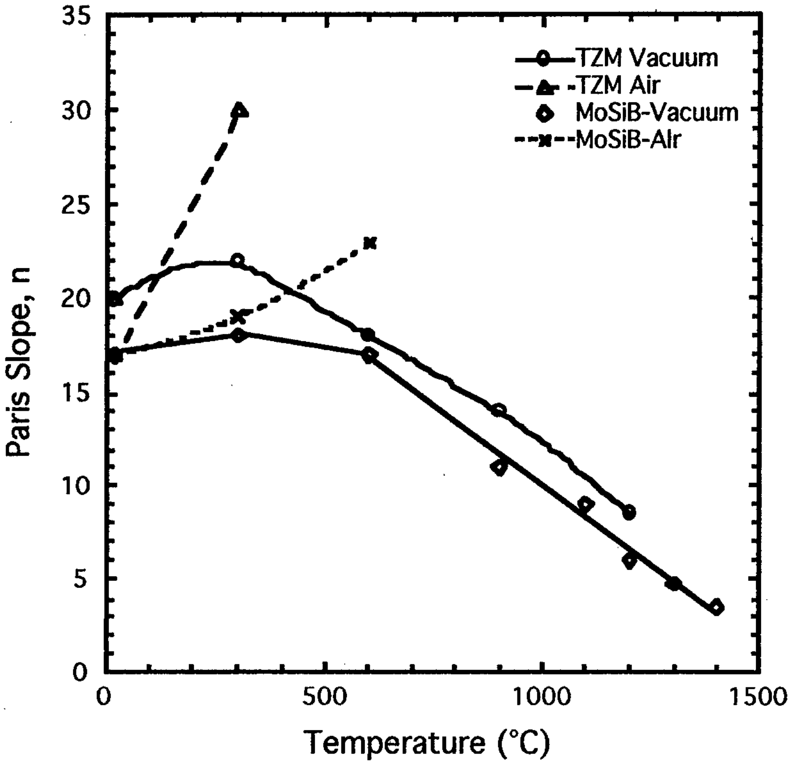

Figure 26: Variation in Paris slope with temperature and environment for TZM and the two-phase Mo-Si-B alloy.

An examination of the fracture surface of the 1200°C compact tension specimen of TZM that was failed in fatigue reveals that although fracture mode is predominantly transgranular cleavage (Figure 27a), the cleavage facets illustrate a lot of surface roughness and micro-ridges (one is shown by an arrow in Figure 27b) indicative of local plasticity. This can be contrasted with crack propagation predominantly along the transverse grain boundaries at room temperature. In the case of the Mo-Si-B alloy, transgranular cleavage is noted (Figure 27c) and a careful examination of the cleavage facets at high magnifications reveals fatigue striations (Figure 27d) that indicate local plasticity and fatigue failure susceptibility. These observations suggesting enhanced local plasticity are consistent with the increased fracture toughness of the Mo-Si-B alloy from ~8MPa√m at room temperature to ~18 MPa√m at 1200°C.

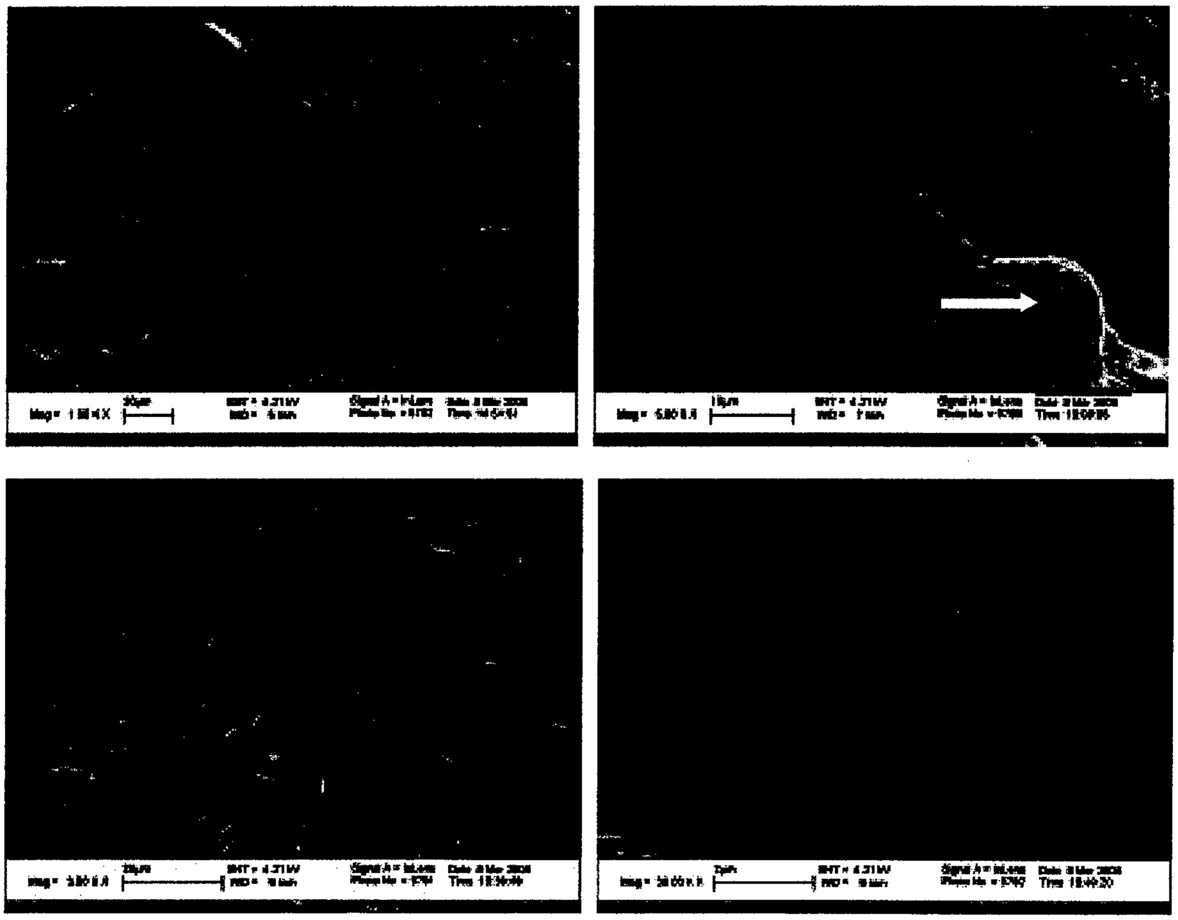

Figure 27: Fracture surfaces following the 1200°C cyclic crack growth tests in vacuum: (a, b) are for TZM and (c,d) are for the two-phase Mo-Si-B alloy. Note the fatigue striations on the cleavage facet in (d) which is a higher magnification image of the region circled in (c).

5.5 Discussion of Results

The crack growth behavior of a two-phase Mo-Si-B alloy (Mo solid solution + 38 volume percent T2 phase), in monotonic and cyclic loading (R=0.1) over a range of temperatures, was compared to that for an off-the-shelf TZM alloy in the previous section. The influence of environment (air versus vacuum) in accelerating this response in the 20°C-600°C temperature range was highlighted. Crack interaction with microstructure on the sample surface obtained from interrupted tests, together with the fracture surfaces of the failed specimens provided an appreciation for preferred crack paths.

Prior to discussing the results in detail, it is pertinent to note that in relation to the high-temperature tests, the monotonically-loaded specimens are exposed to significantly less time at temperature (usually in the order of ten to twenty minutes) than are the cyclically-loaded specimens (several hours). Also, the matrix solid solution in the as-forged condition, though low in Si and B content, is still substantially solid solution strengthened by Si which, as we know is a potent solid solution strengthener in Mo [49], and has a fairly high dislocation content that contributes to a work -hardening component (microhardness of pure Mo was VHN 212, of the matrix of the as-forged Mo-Si-B alloy was VHN 474, and of the matrix of the forged + annealed at 1600°C/48h Mo-Si-B alloy was VHN 375). During the tests at the highest temperatures (1200°C-1400°C), particularly in the cyclic loading mode, matrix softening may be anticipated due to (i) recovery and recrystallization processes, (ii) loss in any Si supersaturation that may have been present in the as-forged alloy, and (iii) intrinsic decrease in matrix strength due to temperature. It is further worth noting that specific to Mo (and W) and its alloys is the fact that recrystallized microstructures are inferior to worked structures in terms of monotonic and cyclic crack growth resistance, and that recrystallized grain boundaries provide preferred crack paths [13, 14, 50].

The room-temperature toughness of the as-forged two-phase Mo-Si-B alloy is around 8 MPa√m (Figure 19) and this only improves marginally when the as-forged material was tested after a substantial high-temperature anneal (1600°C/48h). The annealing process is expected to substantially reduce the residual dislocation content and any Si supersaturation that may have been present in the as-forged condition. The grain size does not change significantly due to this anneal as the volume fraction of the T2 second phase is of the order of 0.38 and is effective in suppressing growth. Thus, the limited room-temperature toughness and its insensitivity to the anneal is attributed to the hardening of the Mo matrix by Si in solid solution (and to a lesser extent by B), to the presence of fairly coarse, anglualr T2 particles and to the presence of a recrystallized (at least, partially) matrix microstructure. Although ultra-pure Mo is known to have a ductile-to-brittle transition temperature below room temperature, small levels of interstitials (particularly, N and O) adversely affect ductility (and toughness) and promote intergranular failure and being powder-processed products, these levels though not measured are anticipated to be relatively high and may also contribute to intergraular embrittlement.

Toughness improvement is gradual up to 1000°C but begins to increase more rapidly thereafter. Minimal changes are anticipated in matrix composition, microstructure or strength up to 1000°C and thus the lack of dramatic improvements in toughness is to be expected. We have shown that at 1200°C and a strain rate of 10^{-4}/s however, the compressive flow stress at 4% strain drops precipitously from 1150 MPa at 1000°C to ~450 MPa, this being due to a decrease in yield stress as well as a decrease in the early stage work-hardening response. The decrease in yield strength is thought to be primarily due to a loss in solid solution strengthening, although some dynamic recovery is also likely to contribute to it. The loss in work hardening capacity is attributed to dynamic recovery. These changes can account for the modest increase observed in toughness (from ~15 MPa√m to ~18 MPa√m), where the high stresses in the region ahead of the advancing crack could promote dynamic recovery.

In the 1200°C-1400°C regime, the toughness increases more rapidly and examination of the crack interaction with microstructure confirms significant crack branching and primary crack tortuosity (Figure 20c). Observations of fracture surfaces confirm a mix of transgranular failure and intergranular fracture, the size of the latter facets not being significantly different from those at room temperature (compare grain sizes in Figures 20b and 20c). An instance of the presence of a recrystallized grain on a transgranular facet (white arrow in Figure 20c) confirms both, the occurrence of some recrystallization (possibly during the test), and the preference for intergranular fracture along recrystallized grain boundaries. The 1400°C compressive flow stress at 4% strain at a strain rate of 10^{-4}/s is ~220 MPa and about half that at 1200°C, and a specimen deformed in compression at 1400°C to about 6-7% plastic strain revealed an almost fully recovered structure in the matrix with well-developed subgrains. Further, there was also some evidence of plasticity in the T2 phase. Thus, the sharp increase in toughness at 1400°C, may be attributed primarily to a decrease in intrinsic matrix strength (and enhanced intrinsic plasticity) coupled with crack branching; the latter is likely encouraged by microstructural changes in the region ahead of the crack tip as discussed above.

Cyclic loading at room temperature of the TZM and the two-phase Mo-Si-B alloy confirm minimal fatigue susceptibility (as seen in the S-N response in Figure 22a) as would be the case with brittle materials. This is also verified by the high threshold stress and a steep Paris slope in the cyclic crack growth results in Figures 23a,b. Crack nucleation was almost always at a ZrO_2 particle whereas in the Mo-Si-B alloy, a specific nucleation site was not easily discernable. Fracture path during cyclic crack growth in the TZM appears to be along grain boundaries (Figures 23c,d), whereas in the Mo-Si-B, a mix of transgranular and intergranular failure was observed (Figures 8e,f combined with fracture surface examination). Crack trapping and crack bridging in the α-Mo phase were cited by Kruzic et al [42] as important mechanisms to bestow toughness and cyclic crack growth resistance in two-phase Mo-Si-B alloys but it is important to recognize that in their experiments, an unusual processing approach was adopted to produce the material that likely rendered regions of the intervening continuous α-Mo phase virtually silicon-free. Si is recognized as an extremely potent solid solution addition to Mo and so, in more-conventionally processed Mo-Si-B alloys, the Mo matrix will contain Si in solid solution and will have significantly higher yield strength and work hardening response and less plasticity. Thus, for example, in this study, ductile bridging ligaments of Mo matrix were not often observed either in monotonic loading or cyclic loading at room temperature. Results from these two studies together however confirm the need to neutralize the negative effects of Si in solid solution on plasticity of the matrix phase at low temperatures.

We will next examine the cyclic crack growth results for TZM and the Mo-Si-B alloy in vacuum and in air in the temperature interval 20°C-600°C. In this temperature regime, microstructural changes are not anticipated due to thermal effects either during heating or during the course of the test, except for oxidation of the crack-tip region for tests conducted in air. An examination of Figures 18, 24a,b, and 26 together confirms that TZM exhibits severe degradation in crack growth response due to environmental effects compared to the Mo-Si-B alloy in this temperature regime.

The effects of temperature and environment on crack growth response during cyclic loading has been studied for a variety of materials, particularly steels and superalloys [51-57] and the underlying mechanisms have been discussed in detail. Cotterill and Knott [52] have examined the effect of environment (air) on the crack growth behavior in the Paris regime for a 9%Cr-1%Mo steel; the study was conducted over a temperature range where the crack growth rate did not change to any significant extent with temperature when tested in vacuum but did when tested in air. They attributed crack growth in air to two components: mechanical growth and environmental growth, the latter being absent in vacuum. They approximated the mechanical component to be the same in air and in vacuum and also assumed no interactive effects between the mechanical and environmental component, the latter clearly being a simplification. Thus, the environmental component was taken to be the difference of crack growth rate in air (da/dN_{air}) and crack growth rate in vacuum (da/dN_{vac}).

This approach has been adopted in this study and Arhennius-type plots were generated for TZM and the two-phase Mo-Si-B alloy by plotting ln(da/dN) versus reciprocal temperature in the interval 20°C-600°C for three different values of ΔK in the Paris regime from tests done in vacuum and in air (Figures 28a,b). The slope of such a curve provides apparent activation energy for the process and these values are documented in Table II. The slopes of the plots for TZM and the Mo-Si-B alloy in Figure 28a (vacuum) are shallow and indicative of the fact that for both materials, within this temperature interval, crack growth rate is almost temperature-independent. The associated apparent activation energy for TZM varies from 1.2-1.4 kJ/mol and that for the Mo-Si-B alloy varies from 1.4-1.7 kJ/mol, for the ΔK values utilized. An examination of Figure 28b, which corresponds to the air tests and where the ordinate is $da/dN_{env} = da/dN_{air} - da/dN_{vac}$, confirms that the Mo-Si-B shows some temperature dependence of crack growth rate relative to that in vacuum, and the associated apparent activation energy is in the range 4.1-5.4 kJ/mol. In contrast, the TZM

(a)

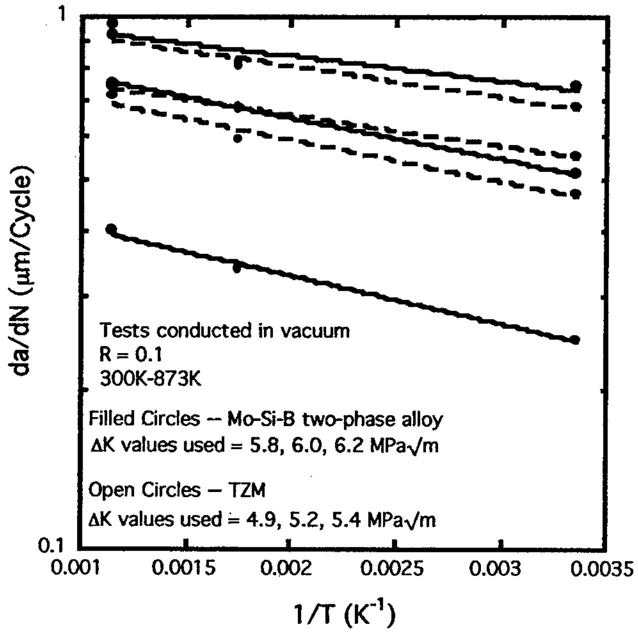

da/dN (μm/Cycle)
1
0.1
0.001
0.0015
0.002
0.0025
0.003
0.0035
1/T (K^{-1})
Tests conducted in vacuum
R = 0.1
300K-873K
Filled Circles -- Mo-Si-B two-phase alloy
ΔK values used = 5.8, 6.0, 6.2 MPa√m
Open Circles -- TZM
ΔK values used = 4.9, 5.2, 5.4 MPa√m

(b)

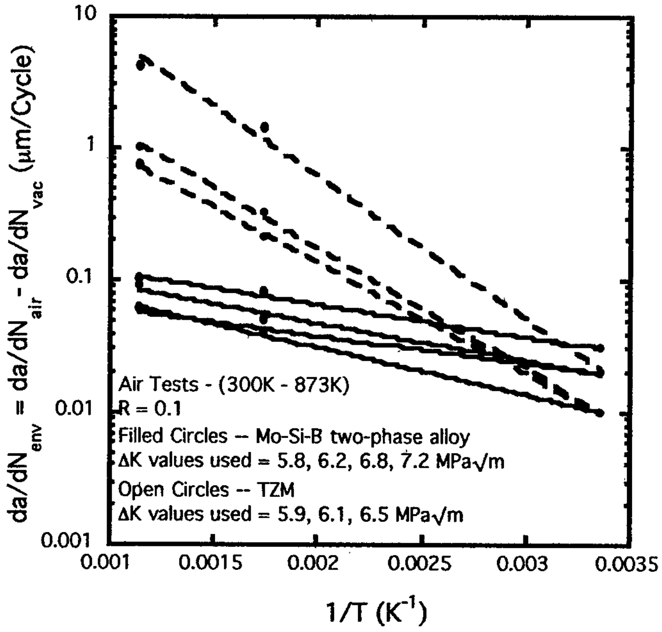

da/dN$_{env}$ = da/dN$_{air}$ - da/dN$_{vac}$ (μm/Cycle)
10
1
0.1
0.01
0.001
0.001
0.0015
0.002
0.0025
0.003
0.0035
1/T (K^{-1})
Air Tests - (300K - 873K)
R = 0.1
Filled Circles -- Mo-Si-B two-phase alloy
ΔK values used = 5.8, 6.2, 6.8, 7.2 MPa√m
Open Circles -- TZM
ΔK values used = 5.9, 6.1, 6.5 MPa√m

(c)

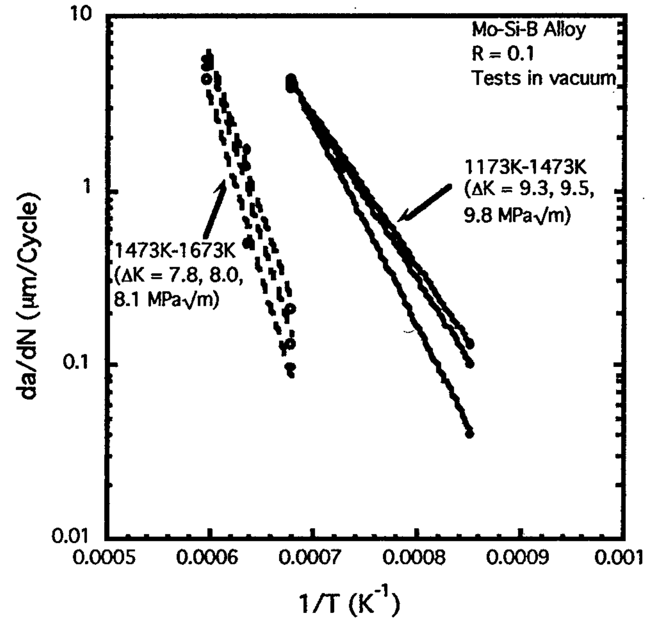

Figure 28: The effect of temperature on crack growth rate for fixed values of ΔK for TZM and the Mo-Si-B alloy a) in vacuum and b) in air, both in the temperature interval 20°C-600°C, and (c) in vacuum in the temperature interval 900°C-1400°C.

alloy tested in air shows a pronounced difference relative to the vacuum test results in Figure 28a. A strong temperature dependence of crack growth rate on test temperature is evident and the associated activation energies are in the range of 16.0-20.4 kJ/mol. This difference in apparent activation energy relative to those in vacuum is interpreted as being due to crack-tip oxidation. Tang and Plumtree [55] report that when a metal is cycled in air at temperatures below half the homologous melting temperature, the dominant mechanism enhancing crack growth is oxidation but the apparent activation energy for crack growth is usually anywhere from 0.2-0.9 of that for oxygen diffusion in the metal matrix.

A mechanism-based explanation that has been provided by Cotterill and Knott [52] for this large difference in measured activation energy in fatigue relative to that for conventional oxidation is based on the ideas that the metal at the crack tip is heavily strained and that virgin metal surface is created each cycle unlike in a simple oxidation test. In fact, apparent activation energy results in their study were more in line with values for erosion-corrosion, which provides support for the

Table II: Apparent activation energy for the two-phase Mo-Si-B alloy and TZM as a function of temperature and environment.

Material	Test Temperature (K)	ΔK Values Used (MPa√m)	Test Environment	Calculated Apparent activation energy, Q (kJ/mol)
Mo-Si-B	300, 573, 873	5.8	Vacuum	1.7
	300, 573, 873	6.0	Vacuum	1.5
	300, 573, 873	6.2	Vacuum	1.4
TZM	300, 573, 873	4.9	Vacuum	1.4
	300, 573, 873	5.2	Vacuum	1.2
	300, 573, 873	5.4	Vacuum	1.2
Mo-Si-B	300, 573, 873	5.8	Air	6.8
	300, 573, 873	6.2	Air	5.4
	300, 573, 873	6.8	Air	4.6
	300, 573, 873	7.2	Air	4.1
TZM	300, 573, 873	5.9	Air	20.4
	300, 573, 873	6.1	Air	17.3
	300, 573, 873	6.5	Air	16.0
Mo-Si-B	1173, 1373, 1473	9.3	Vacuum	221*
	1173, 1373, 1473	9.5	Vacuum	180*
	1173, 1373, 1473	9.8	Vacuum	170*
Mo-Si-B	1473, 1573, 1673	7.8	Vacuum	386**
	1473, 1573, 1673	8.0	Vacuum	375**
	1473, 1573, 1673	8.1	Vacuum	336**

* Q for grain boundary diffusion in Mo = 263 kJ/mol – [60]
** Q for volume diffusion in Mo = 400 kJ/mol – [60]

notion of metal removal during crack growth. Cotterill and Knott [52] also observed two distinctly different behavior for their steel in the 125°C-525°C temperature range they examined; from 125°C-325°C, they obtained an apparent activation energy of around 6 kJ/mol whereas for the 325°C-525°C range they obtained a value of ~30 kJ/mol. They interpreted this difference in activation energies as being due to two distinctly different mechanisms –metal removal through oxidation above 325°C, and oxide-induced enhanced slip irreversibility (formation of oxide films with high modulus leads to image forces that repel dislocations from crack surface and promote tangling and blocking of active slip planes) between 125°C and 325°C.

In the present investigation, the TZM response in air (TZM matrix is assumed to be virtually pure Mo) is associated with the formation of MoO_3 which only begins to sublime at temperatures ≥ 500°C, while that for the Mo-Si-B alloy is associated with the formation of a protective borosilicate scale over a MoO_3 scale [58]. Parabolic kinetics was reported for pure Mo oxidation in the 500°C-

600°C regime and described by a rate equation of the form $k_p = 7.93 \times 10^{10} \exp(-160.6/RT)$ mg/cm$^2\sqrt{h}$, whereas for a Mo-12Si-12B (at.%) alloy, the reported rate equation was $k_p = 3.41 \times 10^5 \exp(-94.5/RT)$ mg/cm$^2\sqrt{h}$ [58]. Thus, in the 500°C-600°C range, the weight gain kinetics for the Mo-Si-B alloy is considerably slower than for pure Mo [58], with the Si and B serving to form the borosilicate layer that provides complete coverage. The MoO_3 layer is thought to be porous [59] so that oxygen diffusion through the layer forming at the crack tip may not be the rate-limiting step but the oxygen-metal reaction kinetics would. The accelerated crack growth in the TZM during cyclic loading at a given temperature within the regime under discussion is thought to be associated with crack growth rate lagging the oxidation rate and crack growth occurring incrementally through the oxide scale rather than the metal. Further, spallation of the oxide during cyclic loading can also lead to continuous exposure of the fresh metal at the crack tip. The strong temperature dependence of crack growth is attributed to the exponential dependence of the reaction kinetics on temperature as described above [58]. In contrast, the Mo-Si-B alloy has a significantly lesser dependence of crack growth on temperature but nevertheless finite. This weaker temperature dependence could be associated with oxygen diffusion through the borosilicate layer and the slower reaction rates [58]. Further, it is argued that the enhanced crack growth rate in air at a given temperature relative to vacuum may perhaps be related to slip irreversibility resulting as a consequence of the borosilicate layer, and the temperature dependence of the phenomenon is a then a consequence of the formation of thicker layers at higher temperatures.

Next, we turn our attention to cyclic crack growth at higher temperatures (900°C-1400°C). Such tests were conducted in vacuum (1.33×10^{-10} MPa) and it is presumed that if there is any environmental effect on crack growth behavior, it would be minor. The variation of da/dN with temperature for different values of ΔK in the Paris regime for the Mo-Si-B alloy is plotted in Figure 28c for this temperature range. In all cases, crack growth per cycle increases with increasing temperature. The data however group into two regimes: the first set belonging to the 900°C-1200°C range providing an apparent activation energy of 170-220 kJ/mol (Table II) and a second set belonging to the 1200°C-1400°C regime with an apparent activation energy of 336-386 kJ/mol. The apparent activation energy for grain boundary diffusion in Mo is reported as 263 kJ/mol [60] whereas that for bulk diffusion is ~400 kJ/mol [60]. Good agreement of apparent activation energy with literature data is recognized in both instances.

Evidently, there are two competing effects; increasing plasticity with increasing temperature (Figure 19 -- where the test duration is in the order of minutes and therefore creep effects are thought to be insignificant) which should decrease crack advance per cycle, and creep effects during the fatigue tests which often leads to an enhancement in crack growth per cycle. In addition, the high stresses at the crack tip can also trigger dynamic recrystallization ahead of the advancing crack tip, provided recrystallization kinetics are comparable to crack growth rates. This certainly appears to be the case at 1400°C (Figure 29), when a cyclic crack growth test was interrupted and the microstructure ahead of the crack tip was examined. Two lobes of recrystallized regions can be seen ahead of the crack tip, and crack then advances intergranularly along the newly-formed grain boundaries. Enhancement in crack growth rates (per cycle) is therefore also affected by this microstructural instability. Dynamic recrystallization of the structure ahead of an advancing crack could pose a problem to the high temperature fatigue response of such materials. It is however pertinent to note that recrystallization was only observed in the 1400°C test not at lower temperatures, and that too only in the cyclic loading test where the cycling frequency used in this study of 5 Hz is lower than that used in most studies (more like 20 Hz) and only after a ΔK of ~8.8 MPa√m was reached. In this sense, this observation defines an upper bound for using such an alloy in applications where fatigue failure is of primary concern.

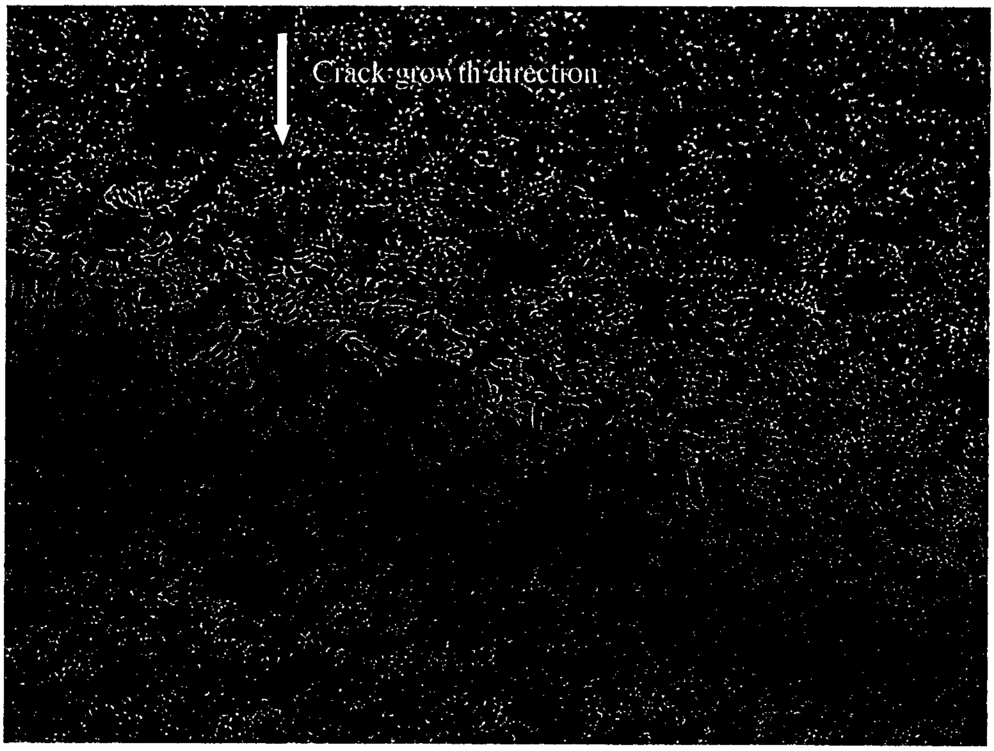

Figure 29: A recrystallized zone ahead of the advancing crack tip in a fatigue crack growth specimen tested at 1400°C in vacuum (R = 0.1; 5Hz). The ΔK value at which recrystallization was first observed was ~8.8 MPa√m (within the Paris regime).

6.0 CONCLUSIONS

6.1 High Temperature Compression Response

A detailed study of the compression behavior of powder-processed off-the-shelf TZM, an experimental two-phase Mo-Si-B alloy and to a lesser extent, a three-phase Mo-Si-B alloy was undertaken. Results from these studies show that

(1) The flow stress of the two Mo-Si-B alloys are similar to each other and superior to the TZM alloy examined in this study for all combinations of temperature and strain rates investigated.

(2) High-temperature deformation of the Mo-Si-B alloys is believed to be matrix Mo solid solution controlled; the presence of blocky T2 particles is instrumental in providing physical obstruction to slip, thereby substantially increasing the flow stress of the "composite".

(3) Post deformation examination confirms dynamic recovery and recrystallization in the matrix in these alloys at the slower strain rates.

(4) The T2 phase in the two-phase alloy shows a range of behavior from brittle fracture through plastic deformation to simply elastic deformation. The specific response observed is dependent on temperature and strain rate.

5) Finite element analysis confirms strain localization in the matrix, the extent being greater with decreased work-hardening capability of the matrix, as would be the case when temperature is increased or strain rate is decreased or both. In contrast, when the T2 phase is provided the ability to deform plastically, strain localization in the matrix is reduced and deformation is relatively more homogeneous.

(6) Computations also confirm stress multiplication in the T2 particles, particularly when they are treated as being elastic. This feature coupled with the interplay between fracture stress and plastic flow is used to rationalize the observed range of post-deformation microstructure.

6.2 Fracture Toughness and Fatigue Response

Results from a detailed study of the monotonic and cyclic crack growth response in the 300K-1673K regime of two Mo-based alloys, TZM and Mo-Si-B are reported. Crack interaction with microstructure, preferred fracture paths and microstructural changes during testing at elevated temperatures have all been characterized and correlated with measured properties. The effects of environment at lower temperatures and of creep at higher temperatures on cyclic crack growth behavior have been delineated through apparent activation energy calculations. The following statements summarize the findings.

1. The fracture toughness of the Mo-Si-B alloy at room temperature is 8 MPa$\sqrt{m}$ and this low toughness is believed to arise due to intrinsically low matrix toughness and stress concentration from the angular, fairly large brittle T2 particles located at the grain boundaries. The low matrix toughness is thought to be primarily a consequence of Si in solid solution but also due to a partially (if not fully) recrystallized microstructure.

2. Toughness increases gradually with temperature to ~17-18 MPa$\sqrt{m}$ at 1200°C, but then sharply to 25 MPa$\sqrt{m}$ at 1400°C. Associated with this increase is a transition in fracture mode with multiple cracking and higher incidences of transgraular cleavage (which in bcc metals may be accompanied with extensive plastic deformation) being observed at 1200°C and 1400°C.

3. The S-N response obtained at room temperature for the Mo-Si-B alloy is superior to the TZM used in this study. However, room temperature S-N response reported in the literature for TZM [16] is similar to what was measured for the Mo-Si-B alloy in this study. The poor response for TZM in this study is thought to arise from improper processing of the "off-the-shelf" TZM which had a partially recrystallized microstructure with large ZrO_2 particles dispersed in them that acted as fracture nucleation sites. The response observed for the Mo-Si-B alloy is typical of a material with a toughness of 8 MPa$\sqrt{m}$.

4. The S-N response of the Mo-Si-B alloy at 1200°C was indicative of the fact that the material was prone to fatigue failure, showing a larger cycle dependency of failure stress; this is in line with a material capable of plastic deformation. The Mo-Si-B alloy is capable of enduring 550 MPa for 10^7 cycles compared to 250 MPa at 850°C for TZM [16].

5. Cyclic crack growth studies at room temperature illustrated a high threshold ΔK and a steep Paris slope for the Mo-Si-B alloy. The response for TZM was not appreciably different. In the 20°C-600°C regime, the TZM however showed significant deterioration when tested in air whereas the Mo-Si-B alloy did not (i.e. results from air and vacuum tests for the Mo-Si-B alloy yielded similar results). This difference in sensitivity to test environment in the two cases is attributed to the nature of the oxide formed. When these two alloys are tested in vacuum however, neither one shows a significant change in behavior with temperature within this temperature range.

6. In the temperature interval 600°C-1400°C, where all tests were conducted in vacuum, the TZM and the Mo-Si-B alloy show a continuous decrease in the Paris slope with increasing temperature, reaching ~8 and ~6 respectively at 1200°C, and 3.5 at 1400°C (for the Mo-Si-B alloy. TZM was not tested at 1400°C). Fatigue striations were clearly observed on the cleavage facets of the Mo-Si-B alloy tested at 1200°C.

7. In the case of the Mo-Si-B alloy, crack growth per cycle, da/dN, increased with increasing temperature in the temperature range 900°C-1400°C for a fixed value of ΔK. This is indicative of creep-assisted fatigue crack growth and apparent activation energies extracted from the results suggest grain boundary diffusion dominance in the 900°C-1200°C range and volume diffusion dominance in the 1200°C-1400°C range.

8. Recrystallization ahead of the advancing crack tip was noted in the Mo-Si-B specimen that was subjected to cyclic loading at 1400°C when the ΔK level was sufficiently high (~8.8 MPa√m) and for the cycling frequency used in this study (5 Hz). As a recrystallized microstructure in Mo and its alloys is thought to promote intergranular embrittlement, conditions that promote recrystallization may set the upper bound for the alloy, and alloy design considerations to discourage/suppress recrystallization are recommended.

7.0 REFERENCES

1. D. Berczik, Pratt & Whitney, East Hartford, CT, private communications.
2. S. Suresh, in Fatigue of Materials, Cambridge Solid State Science Series, editors: E.A. Davis and I.M. Ward, Cambridge University Press, 1991.
3. L.F. Coffin, *Trans. ASME*, **76**, 931 (1954).
4. S.S. Manson, in *National Advisory Commission on Aeronautics: Report 1170*; Cleveland, Lewis Flight Propulsion Laboratory, 1954.
5. Mechanical Behavior of Materials by T.H. Courtney, McGraw-Hill series in Materials Science and Engineering, McGraw-Hill Inc., New York, 1990 (ISBN 0-07-013265-8).
6. D.M.R. Taplin and A.L. Collins, *Ann. Rev. Mater. Sci.*, 8, 235 (1978).
7. A. Ferro, P. Mazzetti, and G. Montalenti, *Philos. Mag.*, 12, 867 (1965).
8. H. Boehling and R. Burman, in Progress in Powder Metallurgy 1983, Volume 39. Editors: H.S. Nayar, S.M. Kaufman, and K.E. Meiners, MPIF, Princeton, NJ. p.491.
9. S.M. Tuominen and V. Biss, in Modern Developments in Powder Metallurgy, Volume 14-Special Materials, 1980. Editors: H.H. Hausner, H.W. Antes, and G.D. Smith, MPIF, Princeton, NJ, p. 215.
10. T.J. Patrician, V.P. Sylvester and R.L. Daga, *International Journal of Refractory and Hard Metals*, 4, 133 (1985).
11. J.Z. Briggs and R.Q. Barr, *High Temperatures-High Pressures*, 3, 363 (1971).
12. W. Jakobeit, *International Journal of Refractory and Hard Metals*, 2, 133 (1983).
13. V.F. Terent'yev, I.S. Kogan, and L.G. Orlov, *Fiz. Metal. Metalloved.*, 42, 1273 (1976).
14. V.F. Terent'yev, E.E. Savitskaya, I.S. Kogan, and L.G. Orlov, *Izv. Akad. Nauk SSSR, Met.*, 6, 129 (1976).
15. R.L. Stephenson, *Trans TMS-AIME*, 245, 997 (1969).
16. H.A. Calderon, G. Kostorz and G. Ullrich, Mater. Sci. Eng., A160, 189 (1993).
17. J. Warren, *International Journal of Refractory and Hard Materials*, 16, 149 (1998).
18. Ya. M. Vitorskiy, R.K. Ivashchenko, S.N. Kaverina, D.V. Lotsko, Yu. V. Mil'man, and V.I. Trefilov, *Fiz. Metal. Metalloved.*, 31, 1076 (1971).
19. C.A. Nunes, R. Sakidja and J.H. Perepezko, in Structural Intermetallics 1997, Editors; M.V. Nathal et al., TMS, Warrendale, PA. 1997, p. 831.
20. R. Sakidja, G. Wilde, H. Sieber and J.H. Perepezko, MRS Proceedings, Vol. 552, 1999, p. KK6.3.1.

21. J.H. Perepezko, R. Sakidja and S. Kim, "Phase Stability in Processing and Microstructure Control in High Temperature Mo-Si-B Alloys", MRS Proceedings, 2000 (Vol. 646) – preprint.
22. R. Sakidja, H. Sieber and J.H. Perepezko, *Phil. Mag. Lett.*, **79**, 351 (1999).
23. J.H. Perepezko, R. Sakidja, S. Kim, Z. Dong and J.S. Park, in ISSI-3, Jackson Hole Wyoming, 2001.
24. D.M. Dimiduk and J.H. Perepezko, *MRS Bulletin*, **28**, 639 (2003).
25. K. Ito, K. Ihara, K. Tanaka, M. Fujikura and M. Yamaguchi, *Intermetallics*, **9**, 591 (2001).
26. M.K. Meyers, M.J. Kramer and M. Akinc, *Intermetallics*, **4**, 273 (1996).
27. D.P. Mason and D.C. Van Aken, *Acta Metall. Mater*., **43**, 1201 (1995).
28. K. Yoshimi, M.H. Yoo, A.A. Wereszczak, S.M. Borowicz, E.P. George and R.H. Zee, *Scripta Mater*., **45**, 1321 (2001).
29. I. Rosales and J.H. Schneibel, *Intermetallics*, **8**, 885 (2000).
30. J.G. Swadener, I. Rosales and J.H. Schneibel, MRS proceedings, Vol. 646, 2001, Materials Research Society, N4.2.
31. K. Ito, M. Kumagai, T. Hayashi and M. Yamaguchi, *Scripta Mater*., **49**, 285 (2003).
32. K. Ihara, K. Ito, K. Tananka and M. Yamaguchi, Mater. Sci. Eng. A, 329-331, 222 (2002).
33. K. Yoshimi, S. Nakatani, N. Nomura and S. Hanada, *Intermetallics*, **11**, 787 (2003).
34. J.H. Schneibel, M.J. Kramer, O. Unal and R.N. Wright, *Intermetallics*, **9**, 25 (2001).
35. J.H. Schneibel, D.S. Easton, E. Choe and R.O. Ritchie, ISSI-3, Jackson Hole, Wyoming, 2001.
36. J.H. Schneibel, C.T. Liu, L. Heatherly and M.J. Kramer, *Scripta Mater*., **7**, 1169 (1998).
37. J.H. Schneibel, M.J. Kramer and D.S. Easton, *Scripta Mater*., **46**, 217 (2002).
38. J.H. Schneibel, *Intermetallics*, **11**, 625 (2003).
39. T.G. Nieh, J.G. Wang and C.T. Liu, *Intermetallics*, **9**, 73 (2001).
40. H. Choe, D. Chen, J.H. Schneibel and R.O. Ritchie, *Intermetallics*, **9**, 319 (2001).
41. H. Choe, J.H. Schneibel and R.O. Ritchie, *Metall. Mater. Trans*., **34A**, 225 (2003).
42. J.J. Kruzic, J.H. Schneibel and R.O. Ritchie, *Scripta Mater*., **50**, 459 (2004).
43. Smithells' Metals Reference Book, edited by E.A. Brandes, G.B. Brook, 7th edition (1992).
44. R. Sakidja and J.H. Perepezko, private communication.
45. T. Christman, A. Needleman and S. Suresh, *Acta Metall*., **37**, 3029 (1989).
46. H.H.M. Cleveringa, E. Van Der Giessen and A. Needleman, Acta Mater., 3163 (1997).
47. Jingyi Cheng, Sia Nemat-Nasser and Weiguo Guo, *Mech. of Mat*., **33**, 603 (2001).
48. M.K. Meyer, A.J. Thom and M. Akinc, *Intermetallics*, **7**, 153 (1999).
49. L. Northcott, Metallurgy of the Rarer Metals -5, Butterworth Scientific Publications, London, 1956.

50. A. Kumar and B.L. Eyre, *Proc. Royal Soc. London, Series A, Math. Phys. Sci.*, **370**, 431 (1980).
51. W. Hoffelner, C. Wuthrich, G. Schroeder and G.H. Gessinger, *High Temperatures-High Pressures*, **14**, 33 (1982).
52. P.J. Cotterill and J.F. Knott, *Acta Metall. Mater.*, **40**, 2753 (1992).
53. S-F. Chen and R.P. Wei, *Mater. Sci.Eng.*, **A256**, 197 (1998).
54. R.P. Wei and Z. Huang, *Mater. Sci. Eng.*, **A336**, 209 (2002).
55. N.-Y. Tang and A. Plumtree, *Mater. Sci Eng.*, **A141**, 55 (1991).
56. J. Byrne, R. Hall and L. Grabowski, Int. J. Fatigue, **19**, 359 (1997).
57. M.B. Cortie and G.G. Garrett, in "Creep and Fracture of Engineering Materials and Structures: Proceedings of the Third International Conference held at University College, Swansea", pp. 635-648, 1987.
58. T.A. Parthasarathy, M.G. Mendiratta and D.M. Dimiduk, *Acta Mater.*, **50**, 1857 (2002).
59. N. Floquet, O. Bertrand and J.J. Heizmann, *Oxid. Met.*, **37**, 253 (1992).
60. H.J. Frost and M.F. Ashby, *Deformation Mechanism Maps: The Plasticity and Creep of Metals and Ceramics,* Pergamon Press, United Kingdom, 1982.